INTERNATIONAL JOURNAL OF
IJCOE
COASTAL, OFFSHORE & ENVIRONMENTAL ENGINEERING

Volume 3 | Issue 2 | Jul 2018

www.ijcoe.org info@ijcoe.org 10

International Journal of Coastal, Offshore and Environmental Engineering (IJCOE) Vol. 3 / Issue. 2 / Jul 2018

International Journal of Coastal, Offshore & Environmental Engineering
Since 2015
ISSN: 2980-8731 (online)

Volume 3 | Issue 2| Jul 2018
IJCOE
Editor-in-Chief: Prof. Hamid S.Bahai

International Journal of Coastal, Offshore & Environmental Engineering
Since 2015
ISSN: 2980-8721 (online)

In The Name of God

Message from the Editor-in-Chief

The IJCOE journal office was established in 2015,and its first issue was published in 2016. TheIJCOE covers a wide range of research in thefields of oceanography & ocean technology, aswell as marine industries & marine engineering.The editorial board of IJCOE consists of nearly130 of the greatest scientists and researchersfrom over 30 countries worldwide, and thejournal's review board comprises 1,000 membersfrom all five continents. The membership andapplication process for joining the editorial andreview boards of this journal is ongoing. IJCOE isa research-academic quarterly journal that haspublication and distribution permissions fromthe Press Organization and permission topublish scientific-research articles from theMinistry of Science, Research, and Technology(MSRT) with an "A" rating. It also holds a "Q1"rating from the ISC institute with an impactfactor (IF) of approximately 0.43 and isconsidered a "core journal" (prestigious andoutstanding journal). IJCOE is an open-accessjournal and allows the download and receipt ofaccepted articles in full text for free. It respectsand adheres to copyright and COPE regulations.The journal's office operates 24/7, providingservices to researchers. In addition to publishinga regular quarterly journal, IJCOE has 16 specialissues on specific topics in preparation. It alsoprovides conditions for publishing specializedbooks, references, and handbooks. Moreover, itis ready to cooperate with the secretariats ofreputable international conferences to publishtheir selected and outstanding articles. IJCOEevaluates, appraises, and publishes books,articles, and the scientific achievements andfindings of esteemed researchers and scientistsworldwide who are innovating and conductingin-depth research in the "important and strategicfield of the maritime technology & Oceanengineering." It welcomes any form of jointcooperation with universities, research institutes,and related research centers at the national,regional, and international levels, and extends ahand for collaboration.

Classification of Editorial Board in IJCOE

Editor-in-Chief

Director-in-Chief

Deputy Editor

Executive Managers

English Text Editor

Technical Editor

International Editorial Board

National Editorial Board

Editorial Board Associate

Editorial Board Assistant

Guest Editorial Board

Advisory Board

Administrative Coordinator

Honorary Board Member

Methodology Advisor

Author Benefits

- Open Access
- Rapid Publication
- Thorough Peer-Review
- No Copyright Constraints
- Coverage by Leading Indexing Services
- Discounts On Article Processing Charges (APC)
- No Space Constraints, No restriction on the maximum length of the papers, number of figures or colors

INTERNATIONAL JOURNAL OF IJCOE COASTAL, OFFSHORE & ENVIRONMENTAL ENGINEERING

Aims of IJCOE

Hydrodynamics

Marine equipment

Structural mechanics

Ocean environmental predictions

Stochastic calculations Experimental

Automatic Control of Marine Systems

Scope of IJCOE

Marine Hazards

Ocean Acoustics

Naval Architecture

Ocean Engineering

Coastal Engineering

Marine Meteorology

Marine Earth Sciences

Underwater Technology

Marine Renewable Energy

Polar & Arctic Engineering

Marine Renewable Energy

Marine Geography & Geodesy

Marine Environmental Engineering

Automatic Control of Marine Systems

Hydro Physics & Physical Oceanography

Type of papers

- Case Studies
- Book Reviews
- Review Article
- Letters to the Editor
- Methodology Papers
- Editorials and Commentaries
- Response or Rejoinder Papers
- Perspective or Opinion Papers
- Conceptual or Theoretical Papers
- Meta-Analysis and Systematic Reviews
- Short Communications or Brief Reports
- Research Articles (Original Research Papers)

Scientific Research Journal

Ministry of Science, Research And Technology (MSRT)

Jurnal Ranking 2023: A

Ministry Of Science, Research And Technology (ISC)

Citation Impact 2022: 0.429

Quartile 2022 : Q1

Core Collection

IJCOE is a Member of

Cantact Us

Office 1 | Research Institute of Meteorology and Atmospheric Science

Address | Tehran, Shahid Kharrazi Highway, Pajoohesh Blvd, Research Institute of Meteorology and Atmospheric Science, Sand and Dust Storm International Research Center (SDS-IRC), No. 13, 1st floor.

Phone | +982144787652

Postal code | 13611-14977

website | www.rimac.ac.ir

Office 2 | Iranian National Institute for Oceanography and Atmospheric Science

Address | Tehran, Dr. Fatemi Gharbi St., Shahid Etemadzade St., No. 3, third floor.

Phone | +982166944873

Postal code | 13389 – 14118

website | www.inio.ac.ir

Email | Info@ijcoe.org

Website | www.ijcoe.org

Follow Us

www.ijcoe.org

INTERNATIONAL JOURNAL OF IJCOE COASTAL, OFFSHORE & ENVIRONMENTAL ENGINEERING

Volume & Issue:

Volume 3, Issue 2, July 2018

Number of Articles: 6

Content

INTERNATIONAL JOURNAL OF
COASTAL & OFFSHORE ENGINEERING IJCOE Vol.3/No. 2/Summer 2018 (1-9)

Available online at: http://ijcoe.org/browse.php?a_code=A-10-117-2&sid=1&slc_lang=en

Effect of FRP Material Properties on Chord SCFs of an FRP-Strengthened Offshore Tubular T-Joint under Brace Axial Loading

Alireza Sadat Hosseini[1*], Mohammad Lesani[2], Mohammad Reza Bahaari

[1*] *PhD Student, University of Tehran, Tehran, Iran; a.sadat@ut.ac.ir*
[2] *Assistant Professor, Sadra University, Tehran, Iran; m.lesani@sadra.ac.ir*
[3] *Professor, University of Tehran, Tehran, Iran; mbahari@ut.ac.ir*

ARTICLE INFO

Article History:
Received: 30 Apr. 2018
Accepted : 1 Sep. 2018

Keywords:
Tubular T-joint
Offshore Platforms
FRP-strengthening
SCF
Finite Element Analysis

ABSTRACT

The relative stress concentration factors (SCF) on the chord member of a tubular T-joint strengthened with FRP which is subjected to brace axial loading are studied. ABAQUS Finite Element software package is used to perform the numerical analyses. Prior to the main studies, the unstiffened joint was validated against the API and Lloyd's Register equations together with the experimental data. Six different types of FRP materials such as Glass/Vinyl ester, Glass/Epoxy (Scotch ply 1002), S-Glass/Epoxy, Aramid/Epoxy (Kevlar 49/Epoxy), Carbon/Epoxy (T300-5208) and Carbon/Epoxy (AS/3501) are used as strengthening material in order to enhance the fatigue life of tubular T-joints through lowering the SCFs. Promising results derived from analyses which show that FRP strengthening method can be considered as an effective method for decreasing the SCF values at tubular T-joints. Results of the analyses for 6mm CFRP layup revealed that under the action of axial loading the FRP strengthening could decrease the SCFs up to 30% and 50% at crown and saddle points of the chord member.

1. Introduction

Offshore jacket platforms are often made of steel circular hollow sections (CHSs) due to high buoyancy and lower drag coefficients and also their adequate structural performance against buckling, bending and torsion. These members are widely used for load-bearing purposes [1]. The most common and basic CHS joint configuration is the T-shape joint which is made by connecting one tube (Brace) perpendicular to the undisturbed exterior surface of the other tube (Chord) using butt welding technique.

Wave loading on offshore structures apply cyclic forces which make them susceptible to fatigue damage Thus, fatigue life prediction in offshore structural joints is necessary to ensure structural safety. Normally, stress-life (S-N) curves are used to assess the fatigue life of offshore structures. In this way, the number of loading cycles that the structure can sustain before fatigue failure could be estimated by hot-spot stress range (HSSR). HSSR is calculated from the stress concentration factor (SCF). According to API [2] part 8.3.1, "for each tubular joint configuration and each type of Brace loading, SCF is defined as: SCF = the hot spot stress range (HSSR)/nominal Brace stress range". In this study, the focus is on the estimation of SCFs at Chord member. Thus, the HSSR is the hot spot stress range on the Chord which must be divided by the nominal direct stress in the Brace member to give the SCF. .

In order to determine the hot-spot stress (HSS) API (2014) presented a conventional method in which, extrapolated geometric stress at the weld toe is to sum the products of the nominal stresses due to each load type and the corresponding SCFs. Estimation of SCFs in tubular as well as non-tubular joints has been the subject of so many numbers of researches since the 1970s. The main objective of these studies was deriving parametric equations. Here, some studies in this field are reviewed.

SCFs could be considered in uni-planar as well as multi-planar joints. Kuang et al. [3] presented parametric equations for estimation of SCF in T, Y, K and KT-joints, using shell elements in a finite element program. It is worth noting that Kuang equations are still widely used in the fatigue design of offshore tubular joints. Equations for SCF estimation in T, Y and X-joints under axial force, in-plane and out-of-plane bending moments were given by Wordsworth and Smedley [4]. Efthymiou and Durkin [5] presented a complete set of SCF equations for T, Y and K-joints.

A wide range of joint geometries under axial loading, in-plane bending and out-of plane bending moments were covered by Hellier et al. [6] finite-element analyses. They presented semi-empirical equations for SCF calculation in tubular T- and Y-joints. Parametric equations were presented by Lloyd's register (LR) [7] which were derived from fitting curves on the existing SCF database. SCFs in Saddle and Crown points of T, Y, X, K and KT-joints are covered in these equations. This is now considered as one of the most liable references for SCF estimation. Chang and Dover [8,9] presented parametric equations for estimation of stress distribution along the Chord-Brace intersection for T, Y, X and KT-joints. SCF equations in multi-planar welded tubular DT-joints were presented by Karamanos et al. [10]. Lotfollahi-yaghin and Ahmadi [11] and Ahmadi et al. [12] proposed equations to predict the SCF along the weld toe of uni-planar KT and multi-plannar DKT-joints under axial loading. SCF distribution parametric equations along the weld toe of outer-inclined and central-vertical Braces of two-planar DKT-joints are presented recently [13, 14]. There are many external strengthening methods for enhancing the mechanical properties of steel members. As a method of strengthening, there are metallic-based methods to decrease the SCFs in CHS joints. Some of these strengthening techniques are reviewed by Lesani et al. [15]. Ramachandra et al. [16] presented formulae for the effect of geometric parameters on SCFs in ring stiffened T and Y-joints.. Nwosu et al. [17] studied the stress distribution along the ring stiffened T-joints through analyzing the effect of geometry, location and number of stiffeners. SCF distributions along the intersections of a T-joint reinforced with doubler plate subjected to the action of combined loadings was investigated by Hoon et al. [18]. Myers et al. [19] studied the effect of three kinds of longitudinal stiffeners in the Chord member on SCF values in jack-up platforms. Fatigue design equations for internal ring-stiffened KT-joints under axial loading were proposed recently [20, 21].

Along with the metallic methods, there are non-metallic external reinforcement methods such as FRP strengthening technique. FRP wrapping method in comparison to the metallic methods is more convenient for handling and application. It resists longer in corrosive areas. Moreover, its potentially high overall durability, light weight, superior strength-to-weight ratio, tailorability and high specific performance attributes make it to be easier for application in areas which conventional materials may encounter deficiencies.

As some examples researches done by Hollaway and Cadei [22], Zhao and Zhang [23] and Zhao [24] on FRP strengthened steel structures are remarkable. Jiao and Zhao [25] studied the - CHSs strengthened with four layers of CFRP under the action of tension loading. Steel short columns strengthened with CFRP were investigated by Shaat and Fam [26] through experiments. Zhao et al. [27] studied the load-bearing capacity of RHSs strengthened with CFRP sheets. Thin walled steel sections which were strengthened with cross-ply FRPs were investigated by Bambach et al. [28]. Wang et al. [29] studied the restraining effect of using external GFRP composites for steel tubes subjected to significant axial displacement. Nishino and Furukawa [30] studied the buckling behavior of CFRP strengthened steel tubes. According to this study, the amount of CFRP used as a strengthening component, has an important impact on delaying buckling and subsequently increasing the section ultimate capacity. The influence of wrapping techniques on deformation capacity of steel tubes under the action of static axial loading was studied by Teng and Hu [31]. Alemdar et al. [32] experimentally and analytically investigated fatigue performance of cover-plate specimens with CFRP reinforced welded connections. A numerical investigation on the failure pattern, ultimate static strength and detailed behavior of GFRP strengthened steel tubular T-joints under axial Brace compressive loading was performed by Lesani et al. [15]. They observed a remarkable increase in joint ultimate capacity due to the combined action of steel and composite against the compressive load. In addition, critical deformations and ovalization of Chord member showed a descending trend up to 50% of the un-strengthened joint. Lesani et al. [33] investigated the ultimate capacity of GFRP strengthened T-joints under the action of static compressive loading through the experiments. Increase up to 50% in the ultimate load-bearing capacity of the tubular joint strengthened by Glass/vinyl ester was observed. Lesani et al. [34] investigated the GFRP strengthened tubular T and Y-joints through a numerical and experimental research program. In this research, the state of the strengthened joint strength, deformation, ovalization, stresses and failure of T and Y-joints under compressive loading were investigated. It was observed that the static strength of tubular T and Y-joints could be improved significantly by the FRP wrapping technique. Chen et al. [35] conducted experiments as well as and numerical analysis to investigate the stress concentration factors in concrete-filled circular chord and square braces in K-joints under balanced axial loading. It is seen that SCFs in concrete-filled circular chord and square braces K-joints were lower than those of corresponding hollow circular chord and square brace K-joints. Yang et al. [36] experimentally studied the SCFs in concrete-filled tubular Y-joints subject to in-plane bending moment. They observed that this strengthening method could effectively reduce the SCF values. Moreover, SCF is evenly distributed when the value of the axial compression ratio in the chord is increased. Jiang et al. [37] experimentally investigated the mechanical behavior

of tubular T-joints reinforced with the grouted sleeve. The failure mode, ultimate load, initial stiffness and deformability of these joint specimens were studied in detail. It was found that the grouted sleeve enhances the strength up to 154.3%~172.7% of the corresponding un-reinforced joint.

According to the literature, during the past years, considerable effort has been devoted to studying SCFs in various unstiffened joints but much fewer on stiffened joints. Metallic-based schemes were mostly used as the strengthening technique. Due to the numerous advantages of non-metallic schemes such as the FRP-wrapping technique on enhancing the static load-bearing capacity of CHSs and prospect of the increasing interest in using such reinforcing schemes, studying the SCFs in FRP-strengthened tubular joints seems to be necessary in order to confirm the efficacy of this method. Sadat Hosseini et al. [38] comprehensively investigated the SCF distribution in FRP-strengthened tubular T-joints under brace axial loading. In this study three types of FRP materials are studied. Moreover, Sadat Hosseini et al. [39] investigated the SCFs in FRP strengthened tubular T-joints subjected to brace axial loading, in-plane and out-of-plane bending moments using finite element analyses. Three FRP materials where used and remarkable results were observed for 1 mm thick strengthening. The present research is aimed at such investigations, in which the results of numerical analyses on 48 steel tubular T-joints strengthened with six various 6mm thick FRP materials were used to deeply investigate the effects of FRP material on the SCF values at the weld toe under Brace axial load. The finite element model was verified against the experimental results extracted from HSE OTH 354 report [7] and the predictions of Lloyd's register (LR) and API equations.

2. Unstiffened Joint FE Model Verification

Here, finite element model of the unstiffened joint was developed and analyses were carried out using ABAQUS [40] software package. The unstiffened T-joint is the joint 1.3 from JISSP project experimental results [7]. Table 1 gives the geometric parameters of the joint.

Table 1. Values of the chord diameter and the other geometric parameters of the T-joint

Reference	D (mm)	α $=2L/D$	β $=d/D$	γ $=D/2T$	τ $=t/T$
JISSP joint 1.3	508	10	0.8	20.3	0.99

The finite element geometries of the unstiffened joints are exactly as same as the geometry of the experimental models. In this study, ABAQUS 3D brick elements (C3D20) are incorporated to model the unstiffened joint geometry. This type of element is defined by 20 nodes having three degrees of freedom per node.

Fig. 1(a) illustrates the isometric view of the T-joint numerical model. The mesh enlargement view of the T-joints is presented in Fig. 1(b). Moreover, the weld profile at the Brace-Chord intersection is modeled in order to achieve accurate stresses along the Chord-Brace intersection. It is important to model the weld geometry with accurate dimensions. Here, the weld profile along the Brace-Chord intersection satisfies the specifications addressed in AWS [41]. Along with the AWS (2010) specifications some simplifications according to the techniques utilized by Lee [42] and Chiew et al. [43] are used to make it possible to create a smooth and adequately accurate weld profile. For further discussion, the reader is referred to Lie et al. [44]. In Fig. 1(c) the weld profile section in finite element model can be seen. Weld profile is modeled as a sharp notch by using 3D brick 20 nodes elements. The weld material properties are assumed the same as the Chord and Brace.

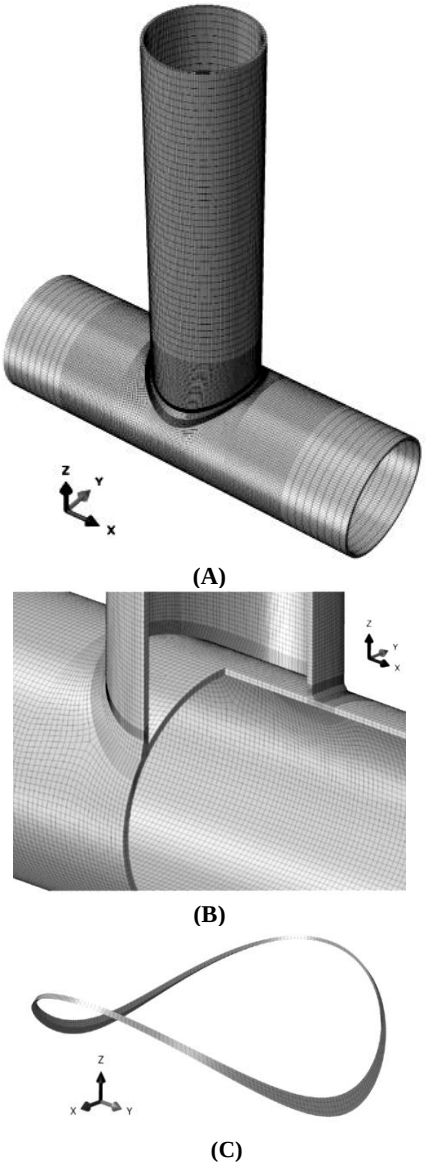

(A)

(B)

(C)

Figure 1. The mesh generated for the t-joint (JISSP joint 1.3) using the sub-zone method; (a): Isometric view, (b): Mesh enlargement, (c): 3d view of the weld profile

Different sub-zone mesh generation methods were used for the weld profile, hot spot stress region, FRP wrapping area and other regions of the joint. The mesh in the hot-spot stress region is much finer than the other zones since more computational precision is required in this area. FRP wrapping areas have coarser meshes but still fine enough to ensure computational accuracy.

The boundary conditions are chosen in such a way to represent the actual boundary conditions of the experiment. Here in the analyses, Chord ends were assumed to be fixed.

In order to determine the stress concentration factors in a tubular joint, a linear elastic numerical analysis needs to be performed [45]. The Young's modulus and Poisson's ratio of steel are taken as 207 GPa and 0.3, respectively exactly as same as the experimental model. In order to estimate the SCFs, the method introduced by IIW-XV-E [46] is implemented. In this method, the peak stress at the weld toe is calculated by linear extrapolation of the von-Mises stresses at distances of 0.4T and 1.4T from the weld toe; where T is the thickness of the Chord member. SCF is calculated by dividing the von Mises stresses at weld toe by the nominal stress on the Brace member. Fig, 2 shows the extrapolation zone on the crown point of the chord member.

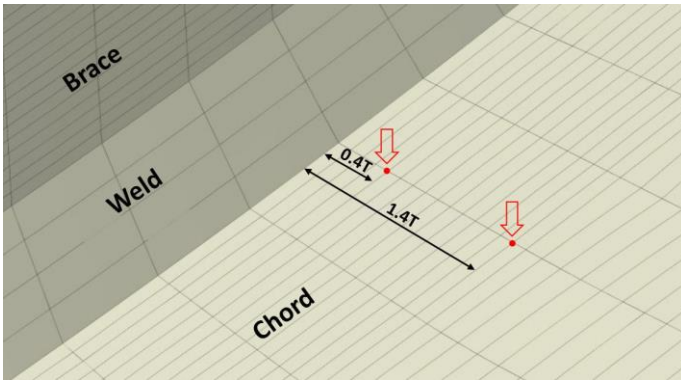

Figure 2. The extrapolation zone on the chord member

In order to validate the finite element model, Lloyd's Register equations and API equations for SCF computation together with the test results published in HSE OTH 354 report for JISSP joint 1.3 [7] is used. Table 2 summarizes the verification results at the Saddle and Crown points. In this table, e1 and e2 show the percentage of relative difference of Lloyd's Register and API equations with test results respectively, and e3 denotes the percentage of the relative difference between the results of finite element model and the experiment results. According to Table 2, it is obvious that the finite element model predicts the SCFs at Crown and Saddle points accurately which is in good agreement with the test results and therefore, the FE model is validated.

Table 2. Comparison of finite element results with experimental data and predictions of LR and API equations

Position	Test	LR Eq.	API Eq.	FEM	e_1	e_2	e_3
Crown	5.4	3.94	3.85	5.3	27	28.7	1.9
Saddle	11.4	10.54	12.13	11.1	7.5	6.4	2.6

3. Stiffened Joint FE Modeling

In the previous section, it is explained how the unstiffened model has been generated and verified against the experimental model. This section gives an account of the specifications of the FRP strengthened numerical model.

FRPs are composed of two distinguishable parts namely fibers and matrix. Thus, various compositions could be made. In this study six types of common FRP materials, Glass/Vinyl ester, Glass/Epoxy (Scotch ply 1002), S-Glass/Epoxy, Aramid/Epoxy (Kevlar 49/Epoxy), Carbon/Epoxy (T300-5208) and Carbon/Epoxy (AS/3501), are used as strengthening material on the T-joint in order to find out how different FRP materials affect the SCF values. Table 3 demonstrates the properties of the FRPs used in the analyses. In this table, subscripts ''1'' and ''2'' stand for the fiber longitudinal and transverse directions respectively.

Table 3. FRP properties [15, 47, 48]

Mechanical properties	E_1 [Gpa]	E_2 [Gpa]	ν_{12}	G_{12} [Gpa]	G_{13} [Gpa]	G_{23} [Gpa]
Glass/ Vinyl ester	28	7	0.29	4.5	4.5	2.54
Glass/Epoxy (Scotch ply 1002)	38.6	8.27	0.26	4.14	4.14	3.1
S-Glass/Epoxy	43	8.9	0.27	4.5	3.18	3.18
Aramid/Epoxy (Kevlar 49/Epoxy)	76	5.5	0.34	2.3	2.3	2.01
Carbon/Epoxy (T300-5208)	132	10.8	0.24	5.7	5.7	3.4
Carbon/Epoxy (AS/3501)	138	8.96	0.3	7.1	7.1	2.82

FRP material is modeled using shell elements defined as a skin layer on the 3D unstiffened joint model. The specifications of the unstiffened joint model are given in the previous section. The FRP shell elements are ABAQUS element type S4R, which is a 4-node doubly curved thin or thick shell with reduced integration. The interior surface of the FRP elements are tied to the external surface of the solid elements of the un-stiffened joint geometry and these two surfaces share the same nodes and mesh topology. This is similar to the actual application of FRP layup on the surfaces. Here a perfect bond state was considered and no cohesive/adhesive element was modeled at the FRP and the steel substrate interface. This is not an irrational assumption since the bond between FRP layer and steel stays undisturbed in the elastic range of

loading according to the experimental and numerical analysis [33]. Fig. 3 shows an enlarged section of the strengthened T-joint.

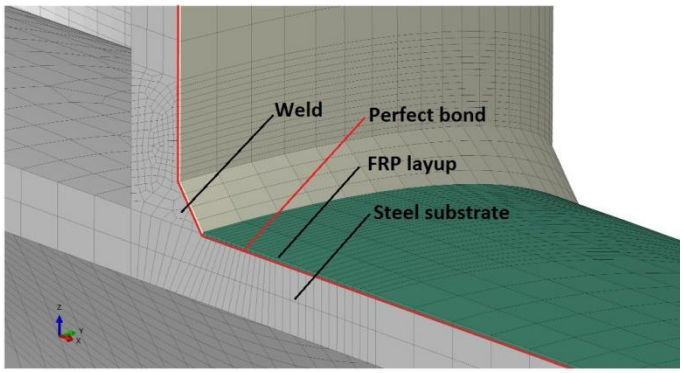

Figure 3. Mesh enlargement around crown point of the numerical model of the frp wrapped t-joint

FRP fibers are considered in two major directions. The 0o (Chord hoop direction and along the Brace longitudinal axis) and 90o orientations. Fig. 4 clarifies how these fiber orientations are being considered in FRP modeling.

For all of the analyses, the strengthening materials are applied on the T-joint having a thickness of 6mm and a wrapping length equal to one diameter of the relative strengthened member (1D on the Chord and 1d on the Brace member).

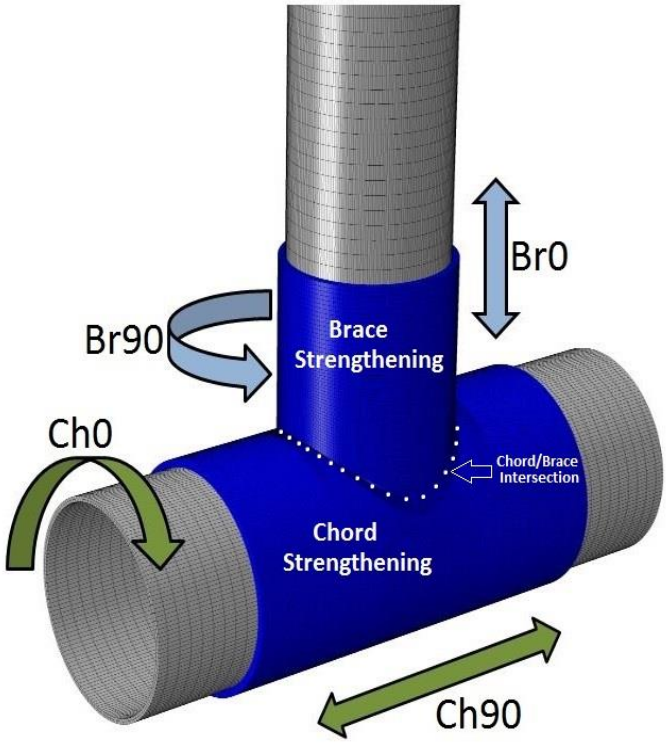

Figure 4. The FRP wrapped T-joint with definition of 0º and 90º fiber orientations in the FRP layup on chord and brace

4. Analysis and Results

Here the results of the analyses on the strengthened T-joints are presented. In order to investigate the stress concentration in FRP strengthened tubular T-joints under Brace axial loading, models were generated and analyzed using ABAQUS finite element software package. The six FRP materials (Glass/Vinyl ester, Glass/Epoxy (Scotch ply 1002), S-Glass/Epoxy, Aramid/Epoxy (Kevlar 49/Epoxy), Carbon/Epoxy (T300-5208) and Carbon/Epoxy (AS/3501)) are applied on the basic joint geometry and the stiffened joints were analyzed. Table 4 gives the abbreviations used for FRP materials in this study. Stresses at Saddle and Crown points at the weld toe on the Chord surface are extracted (HSSR) using IIW-XV-E method and divided by the nominal Brace stress range to find the SCFs at the strengthened joint.

Table 4. The abbreviations of the strengthening schemesand FRP orientations

Abbreviation	Description
Ch0	Chord strengthening with 0º fibers orientation
Ch90	Chord strengthening with 90º fibers orientation
Br0	Brace strengthening with 0º fibers orientation
Br90	Brace strengthening with 90º fibers orientation
Ch0&Br0	Chord and Brace strengthening with 0º fibers orientation on both Chord and Brace
Ch0&Br90	Chord and Brace strengthening with 0º fibers orientation on Chord and 90º fibers orientation on Brace
Ch90&Br0	Chord and Brace strengthening with 90º fibers orientation on Chord and 0º fibers orientation on Brace
Ch90&Br90	Chord and Brace strengthening with 90º fibers orientation on both Chord and Brace

The analyses were carried out in three phases. At first, the Chord alone was strengthened in order to investigate the effects of strengthening the Chord member on SCFs. In the second phase, FRP was applied only to the Brace member to study the Brace strengthening effects, and finally, in the third phase, both of the Chord and Brace members were strengthened. SCF values of the strengthened joints are extracted and divided by the SCFs of the unstiffened joint at Crown and Saddle points to find the SCF ratios. Two major orientations (0o and 90o) are selected for the fibers in FRP layups. Table 5 presents the abbreviations for the strengthening schemes.

Table 5. The abbreviations of the FRP materials

Abbreviation	Description
GV	Glass/vinyl ester
GE	Glass/Epoxy (Scotchply 1002)
SGE	S-glass/Epoxy
AE	Aramid/Epoxy (Kevlar 49/Epoxy)
T300	Carbon/Epoxy (T300-5208)
AS	Carbon/Epoxy (AS/3501)

The results of the analyses of investigation of the effect of using six different FRP compositions as the

strengthening material on the T-joint (JISSP joint 1.3) on SCF values at Crown and Saddle points, when the joint is under Brace axial loading were investigated. The joint is under 10 tones load which is monotonously distributed on the top of the Brace member. Fig. 5 shows the von Mises stress distribution around the Chord/Brace intersection area for the unstrengthened joint as long as the strengthened joint with Carbon/Epoxy (AS/3501) in order to make sense how FRP strengthening could affect the von misses stresses. Stresses at the weld toe in Chord Crown and Saddle points are calculated according to the IIW-XV-E method which is explained previously. These stresses are divided by the nominal stress at the Brace member and thus, SCF values are extracted.

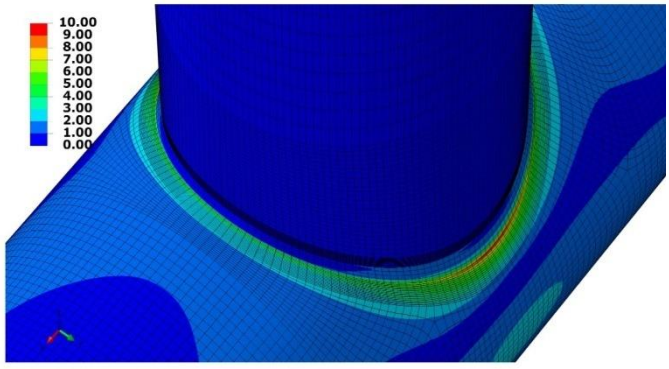

(A)

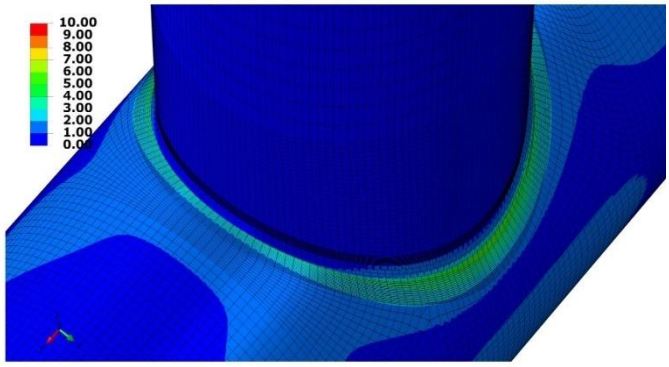

(B)

Figure 5. Von misses stresses on the joint surface for 10 tones axial load at the top of the brace: a) Unstrengthened joint; b) Strengthened joint

Analyses are performed for all fix types of FRPs and results are given for different strengthening schemes. Fig. 6 and Fig. 7 show the relative SCFs (SCF_s: SCF at the strengthened joint divided by SCF_u: SCF at the unstiffened joint) at Crown and Saddle points respectively.

As it can be seen in Fig. 6, the more the stiffer FRP used as strengthening material, the more the SCF values decreases. According to this Figure, fibers orientation on the Chord member has a chronic effect on SCFs. It is seen that the decreasing effect of FRP wrapping on the Chord member when the fibers are in 90°, is three times the FRP wrapping with 0o orientation on average.

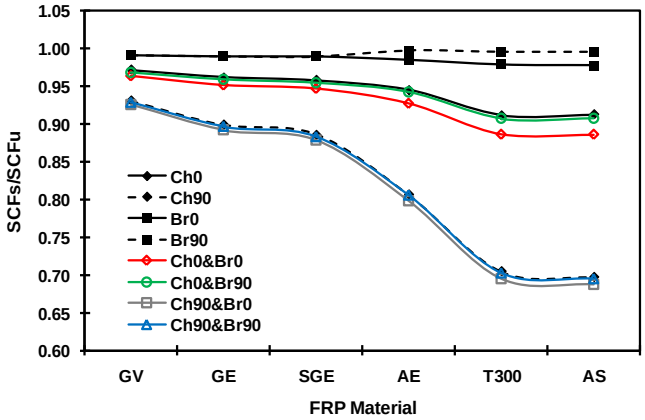

Figure 6. Ratio of SCF at the crown point of the FRP strengthened tubular t-joint with different FRP materials to SCF distribution in un-strengthened joint under brace axial load

According to Fig. 6, in order to further reduce the SCFs at the Crown Point, fibers should be aligned in 90° orientation. Applying FRP only on the Brace member has a negligible unpleasant increasing effect on SCFs (square and dash square lines in Fig. 6). Although Brace strengthening has an undesired effect on SCF, in order to keep the integrity of joint strengthening, in practical applications, both Chord and Brace members will be wrapped.

As an interesting result, applying FRP on both Chord and Brace members simultaneously has more effect on SCF reduction comparing to the other schemes (hollow square and hollow rectangular lines). Given that, using FRP on Brace member, with fibers in 0o orientation has the weakest increasing effect on SCFs, and on the other hand, using FRP with fibers in 90o orientation on the Chord member has the strongest decreasing effect on SCFs, the best layup would be Ch90&Br0. Focus on the effect of FRP material reveals that using Carbon/Epoxy (AS/3501) with 6mm thickness on both Chord and Brace members decreases the SCFs by 30 percent at the Crown point. Generally, the decreasing effect of using stiffer FRPs such as CFRP is about 5 times the GFRP material.

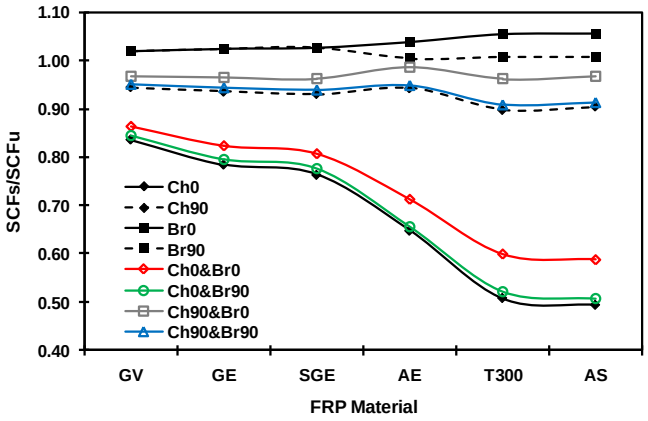

Figure 7. Ratio of SCF at the saddle point of the FRP strengthened tubular T-joint with different FRP materials to SCF distribution in un-strengthened joint under brace axial load

Considering the T-joint when the Chord member is strengthened (Fig. 7), it is seen that, stiffer FRP material (higher mechanical properties) shows more effectiveness in decreasing the SCF values at the Saddle point (Fig. 7). As clearly envisaged from this Figure, using 6mm Carbon/Epoxy material has effectiveness of about three times the GFRP material on SCF reduction, which is about 50% at the Saddle point. As like as the Crown Point, strengthening the Brace member has also an increasing effect on SCFs at the Saddle point. These effects are amplified by increasing the mechanical properties of FRP materials. Between 0º and 90º orientations, using 90o orientation has a weaker additive effect on SCFs. The adverse effect of using higher modulus FRP materials on the Brace member is about maximum 5% at the Saddle point. The effect of different strengthening FRP materials on SCF values when the Chord and Brace members of the T-joint are simultaneously strengthened is also illustrated in this Figure. Based on this figure, applying 6mm Carbon-epoxy on the Chord member with 0º fibers orientation and 90º fibers orientation on the brace is the most effective layup which can lower the SCFs up to 50% at the Saddle point. This confirms the effectiveness of FRP strengthening on SCF reduction in tubular T-joints.
Having Fig. 6 and Fig. 7 along with the mechanical properties given in Table 1, one can find how the change in the value of each mechanical property in two main extreme fiber orientations (0o and 90o) will affect the SCFs under axial loadings.

5. Summary and Conclusions

In this research, changes in SCF values at Crown and Saddle points on the Chord member of the tubular T-joint due to change in FRP material used for wrapping the joint was investigated. The FRP layup thickness is 6mm in all models. The following conclusions were derived from this study:

- Change of fiber and/or matrix material properties corresponds to change in FRP mechanical properties. Use of FRP material with higher values of mechanical properties as the strengthening material shows more effect on SCF values reduction. In general, CFRP strengthening can reduce the SCFs up to 30% and 50% at Crown and Saddle points respectively.
- Among the six common composite material, CFRP materials have the effectiveness of about 3 and 2.5 times the GFRP materials in SCF reduction at Crown and Saddle points respectively.
- According to the results, the most effective schemes under axial loading at Crown and Saddle points are Ch90Br0 and Ch0Br90 (see Table 5) respectively. Besides, in as much as for common practical applications, the joint will completely wrapped with FRP (Chord and Brace are strengthened) the Brace and Chord should be strengthened with FRPs in which the fibers are aligned in both longitudinal and hoop directions.
- Due to the better fatigue performance of CFRP materials in comparison to other composite materials such as GFRP, and based on the findings of this study, it is recommended to use CFRP composites as wrapping and strengthening material for fatigue life extension of tubular joints. Anyway, economical issues must be addressed.

6. References

1- Jia, J., (2008), *An efficient nonlinear dynamic approach for calculating wave induced fatigue damage of offshore structures and its industrial applications for lifetime extension*, Applied Ocean Research, Vol.30, p.189-198.
2- API (American Petroleum Institute), (2014), *Recommended practice for planning, designing and constructing fixed offshore platforms - working stress design*, API RP 2A WSD, 22nd edition.
3- Kuang, J. G., Potvin, A. B., and Leick, R. D., (1975), *Stress concentration in tubular joints*, Proceedings of the offshore technology conference (OTC 2205), Houston, Texas, US.
4- Wordsworth, A. C., and Smedley, G. P., (1978), *Stress concentrations at unstiffened tubular joints*, Proceedings of the European offshore steels research seminar, Paper 31, Cambridge, UK.
5- Efthymiou, M., and Durkin, S., (1985), *Stress concentrations in T/Y and gap/overlap K-joints*, Proceedings of the conference on behavior of offshore structures, Delft, Netherlands.
6- Hellier, A. K., Connolly, M., and Dover, W. D., (1990), *Stress concentration factors for tubular Y and T-joints*, International Journal of Fatigue, Vol.12, p.13-23.

7- Health and Safety Executive (UK), (1997), OTH 354: Stress concentration factors for simple tubular joints - assessment of existing and development of new parametric formulae. Prepared by Lloyd's Register of Shipping.

8- Chang, E., and Dover, W. D., (1999), *Parametric equations to predict stress distributions along the intersection of tubular X and DT-joints*, International Journal of Fatigue, Vol.21, p.619-635.

9- Chang, E., and Dover, W. D., (1999), *Prediction of stress distributions along the intersection of tubular Y and T-joints*, International Journal of Fatigue, Vol.21, p.361-381.

10- Karamanos, S. A., Romeijn, A., and Wardenier, J., (2002), *SCF equations in multi-planar welded tubular DT-joints including bending effects*, Marine Structures, Vol.15, p.157-173.

11- Lotfollahi-Yaghin, M. A., and Ahmadi, H., (2010), *Effect of geometrical parameters on SCF distribution along the weld toe of tubular KT-joints under balanced axial loads*, International Journal of Fatigue, Vol.32, p.703-719.

12- Ahmadi, H., Lotfollahi-Yaghin, M. A., and Aminfar, M. H., (2011), *Geometrical effect on SCF distribution in uniplanar tubular DKT- joints under axial loads*, Journal of Constructional Steel Research, 67, p.1282-1291.

13- Lotfollahi-Yaghin, M. A., and Ahmadi, H., (2011), *Geometric stress distribution along the weld toe of the outer Brace in two planar tubular DKT-joints: parametric study and deriving the SCF design equations*, Marine Structures, Vol.24, p.239-260.

14- Ahmadi, H., Lotfollahi-Yaghin, M. A., and Aminfar, M. H., (2011), *Distribution of weld toe stress concentration factors on the central Brace in two-planar CHS DKT connections of steel offshore structures*, Thin-Walled Structures, Vol.49, p.1225-1236.

15- Lesani, M, Bahaari, M. R., and Shokrieh, M. M., (2013), *Numerical investigation of FRP-strengthened tubular T-joints under axial compressive loads*, Composite Structures, Vol.100, p.71-78.

16- Ramachandra Murthy, D. S., Madhava Rao, A. G., Ghandi, P., and Pant, P.K., (1992), *Structural efficiency of internally ring stiffened steel tubular joints*, Journal of Structural Engineering, Vol.118, p.3016-3035.

17- Nwosu, D. I., Swamidas, A. S. J., and Munaswamy, K., (1995), Numerical stress analysis of internal ring-stiffened tubular T joints, Journal of Offshore Mechanics and Arctic Engineering, Vol.117, p.113-125.

18- Hoon, K. H., Wong, L. K., and Soh, A. K., (2001), *Experimental investigation of a doubler-plate reinforced tubular T-joint subjected to combined loadings*, Journal of Constructional Steel Research, Vol.57(9), p.1015-1039.

19- Myers, P. T., Brennan, F. P., and Dover, W. D., (2001), *The effect of rack/rib plate on the stress concentration factors in jack up Chords*, Marine Structures, Vol.14, p.485-505.

20- Ahmadi, H., Lotfollahi-Yaghin, M. A., Shao, Y. B., and Aminfar, M. H., (2012), *Parametric study and formulation of outer Brace geometric stress concentration factors in internally ring stiffened tubular KT-joints of offshore structures*, Applied Ocean Research, Vol.38, p.74-91.

21- Ahmadi, H., Lotfollahi-Yaghin, M. A., and Shao, Y. B., (2013*), Chord-side SCF Distribution of central Brace in internally ring stiffened tubular KT-joints: A geometrically parametric study*, Thin-Walled Structures, Vol.70, p.93-105.

22- Hollaway, L. C., and Cadei, J., (2002), *Progress in the technique of upgrading metallic structures with advanced polymer composites*, Progress in Structural Engineering and Materials, Vol.4(2), p.131-148.

23- Zhao, X. L., and Zhang, L., (2007), *State of the art review on FRP strengthened steel structures*, Engineering Structures, Vol.29(8), p.1808-1823.

24- Zhao, X. L., (2009), *FRP strengthened metallic structures*, Thin Walled Structures, Special Issue, Vol.47(10), p.1019.

25- Jiao, H., Zhao, and X. L., (2004), *CFRP strengthened butt welded very high strength (VHS) circular steel tubes*, Thin- Walled Structures, Vol.42(7), p.963-978.

26- Shaat, A., and Fam, A., (2007), *Finite element analysis of slender HSS columns strengthened with high modulus composites*, Steel and Composite Structures, Vol.7(1), p.19-34.

27- Zhao, X. L., Fernando D., and Al-Mahaidi R., (2006), *CFRP strengthened RHS subjected to transverse end bearing force, Engineering Structures*, Vol.28(11), p.1555-1565.

28- Bambach, M. R., Jama, H. H., and Elchalakani, M., (2009), *Axial capacity and design of thin walled steel SHS strengthened with CFRP*, Thin-Walled Structures, Vol.7(10), p.1112-1121.

29- Wang, X. G., Bloch, J. A., and Cesari, D., (1991), *Axial crushing of tubes made of multi-materials*, Proceedings of the 4th international MECAMAT seminar on mechanics and mechanisms of damage in composites and multi-materials, St. Etienne, France, London, Mechanical Engineering Publications Ltd., p.351-360.

30- Nishino, T., and Furukawa, T., (2004), *Strength deformation capacities of circular hollow section steel member reinforced with carbon fiber*, Proceedings of the 7th pacific structural steel conference, Long Beach, California, USA, American Institute of Steel Construction.

31- Teng, J. G., and Hu, Y. M., (2007), *Behaviour of FRP jacketed circular steel tubes and cylindrical shells under axial compression*, Construction and Building Materials, Vol.21(4), p.827-838.

32- Alemdar, F., Matamoros, A., Bennett, C., Barrett-Gonzalez, R., and Rolfe, S. T., (2012), *Use of CFRP Overlays to strengthen welded connections under fatigue loading*, Journal of Bridge Engineering, Vol.17(3), p.420-431.

33- Lesani, M, Bahaari, M. R., and Shokrieh, M. M., (2014), *Experimental investigation of FRP-strengthened tubular T-joints under axial compressive loads*, Construction and Building Materials, Vol.53, p.243-252.

34- Lesani, M., Bahaari, M. R., and Shokrieh, M. M., (2015), *FRP wrapping for the rehabilitation of Circular Hollow Section (CHS) tubular steel connections*, Thin-Walled Structures, Vol.90, p.216-234.

35- Chen, Y., Hu, K., and Yang, J., (2016), *Investigation on SCFs of concrete-filled circular Chord and square Braces K-joints under balanced axial loading*, Steel and Composite Structures, Vol.21(6), p.1227-1250.

36- Yang, J., Yang, C., Su, M., and Lian, M., (2016), *Stress concentration factors test of reinforced concrete-filled tubular Y joints under in-plane bending*, *Steel and Composite Structures*, Vol.22(1), p.203-216.

37- Jiang, S., Guo, X., Xiong, Z., Cai, Y., and Zhu, S., (2017), *Experimental studies on behavior of tubular T-joints reinforced with grouted sleeve*, Steel and Composite Structures, Vol.23(5), p.585-596.

38- Sadat Hosseini, A., Bahaari, M. R., Lesani, M., (2018), *SCF distribution in FRP-strengthened tubular T-joints under brace axial loading*, Scientia Iranica, Articles in Press, Accepted Manuscript, Available Online from 06 May 2018.

39- Sadat Hosseini, A., Bahaari, M. R., Lesani, M., (2017), *SCF in FRP strengthened tubular T-joints under brace axial loading, in-plane bending and out-of-plane bending moments*, Proceedings of the 4th conference on smart monitoring, assessment and rehabilitation of civil structures, Zurich, Switzerland, Paper no. 151.

40- ABAQUS/CAE, (2014), Standard user's manual, Version 6.14-1.

41- AWS (American Welding Society), (2010), *Structural welding code, AWS D 1.1:2010* (22nd Edition). Miami, FL (USA), American Welding Society, Inc.

42- Lee, M. M. K., (1999), *Estimation of stress concentrations in single-sided welds in offshore tubular joints*, International Journal of Fatigue, Vol.21, p.895-908.

43- Chiew, S. P., Soh, C. K., Fung, T. C., and Soh, A. K., (1999), *Numerical study of multi-planar tubular DX-joints subject to axial loads*, Computers and Structures, Vol.72, p.746-761.

44- Lie, S. T., Lee, C. K., and Wong, S. M., (2001), *Modeling and mesh generation of weld profile in tubular Y-joint*, Journal of Constructional Steel Research, Vol.57, p.547-567.

45- N'Diaye, A., Hariri, S., Pluvinage, G., and Azari, Z., (2007), *Stress concentration factor analysis for notched welded tubular T joints*, International Journal of Fatigue, Vol.29, p.1554-1570.

46- IIW-XV-E., (1999), International institute of welding subcommission XV-E, *recommended fatigue design procedure for welded hollow section joints*, IIW Docs, XV-1035-99/XIII-1804 99, International Institute of Welding, France.

47- Ganesh, K, and Naik, N. K., (2005), *Some strength studies on FRP laminates*, Journal of Composite Structures, Vol.24, p.51-58.

48- Kollár, L. P., and Springer, G. S., (2003), *Mechanics of composite structures*, Cambridge university press.

INTERNATIONAL JOURNAL OF
COASTAL & OFFSHORE ENGINEERING
IJCOE Vol.3/No. 2/Summer 2018 (11-20)

Available online at: http://ijcoe.org/browse.php?a_code=A-10-230-1&sid=1&slc_lang=en

Automatic Coastline Extraction Using Radar and Optical Satellite Imagery and Wavelet-IHS Fusion Method

Hasan Mirsane[1*], Yaser Maghsoudi[2], Rohollah Emadi[3], Majid Mostafavi[1]

[1] *Hydrography M.Sc., North Tehran branch, Islamic Azad University, Tehran, Iran; hasanmirsane@yahoo.com*
[2] *Faculty of Geodesy and Geomatics Engineering, Khaje Nasir Toosi University of Technology (KNTU), Tehran, Iran*
[3] *Department of Geomatics Engineering, South Tehran branch, Islamic Azad University, Tehran, Iran*

ARTICLE INFO

Article History:
Received: 16 Jul. 2018
Accepted:1 Sep. 2018

Keywords:
Coastline Extraction
Radar
Landsat
Sentinel-1
ALOS
IRS
Fusion
Wavelet
IHS

ABSTRACT

The coastline is defined as an edge or land margin by the sea. Managing such ecological environments in terms of continuous changes requires monitoring at different intervals. To do this, it is necessary to use remote sensing techniques to detect and analyze coastline variations. Two study areas located on the coast of the Persian Gulf (South part of the Qeshm Island and the port of Tien to Asaluyeh) have been studied by two types of optical and radar images and wavelet edge detection algorithm for coastline extracting. In this study, the coastline is extracted in two ways, firstly the coastline extracts from both optical and radar images separately, then by images fusion using wavelet-IHS method. The accuracy obtained in Qeshm area in 2009 from optical, radar and fused images was 3.4, 5.5 and 3.2 respectively, and in Asaluyeh region in 2007, 2.1, 3.4 and 2.98 respectively.

1. Introduction

Coastlines are one the most important linear phenomena on the earth's surface, which have dynamic nature and usually a fragile ecosystem [2]. They have also tremendous value in economical and natural resources. Coastline changes are often the result of coastal erosion or sedimentation, as well as human activities (such as dredging, making breakwaters and ports, etc.). Monitoring and assessing coastal areas for the sustainable planning and predicting coastal behavior also safe navigation could be considered as an important factor in national development and natural resource management [4]. Coastline detection using manual and surveying methods are mainly hard and costly, the non-automatic coastal detection methods by the visual interpretation of high-resolution aerial photos are also time consuming and require tedious process skills and massive attention to details. Therefore, automated and remote sensing methods for monitoring coastal area seems to be necessary. In this study we firstly extract coastlines in study areas using Optical and Radar data separately then extract it from a fused image of these data and evaluate all results by high resolution IRS images. Finally, we estimate the coastline displacement in different times of study.

The extraction of shorelines are well known issue in satellite remote sensing and have been discussed in many publications [8][23][7][15] . Mason, D. C and Davenport, I. J., 1996 suggested the use of a contrast ratio filter together with an active contour model (snake algorithm) as edge detector. S. Mallat *et al.* (1992a and 1992b) suggested a method to detect all edges above a certain threshold. Niedermeier, A., *et al.* (2000) used a Wavelet based edge detection method coastline detection by SAR images. Liu, H and Jezek, K, C., (2004), used thresholding technique on Landsat and Radarsat data. Wang Y. and Allen, R. T., (2008) applied an edge-filtering model with Sobel filter. Ouyang, Y., *et al.* (2010) applied two enhanced Level Set Algorithm (LSA) on Radarsat imagery. Chen, K. S., *et al.* (2011) developed an algorithm for costal changes monitoring from ERS data. They also fallowed morphological filter to refine the boundaries. Acar, U., *et al.* (2012) improved an automatic algorithm to detect coastline using from ALOS/PALSAR data at the coastline of the Black Sea in the north-west part of Turkey.

Optical data makes coastline detection easier while differentiate between water and land and interpretation of coastline observations due to color differences is more distinguishable. Basic techniques, which use optical data, make detection and extraction of a continuous coastline with precision at pixel level

measurement possible. Main issue of optical systems is its dependence on cloud cover, sunlight and generally meteorological conditions, which significantly limits its effectiveness [4]. The similarity of shadows on surface with water bodies (especially in deep water) could also make mistakes in water pixels' classification. In addition, in coastal areas with less than one-meter depth, it is difficult to find threshold values in 5 or 7 bands due to sea-floor reflections to the sensor. The presence of particles in water and its pollution in coastal areas is another problem that makes coastal areas detection (using only one band) difficult. Hence, many researchers have suggested the use of the indexes (which calculated using more than one bands) [15]. The return of light from the sea floor near beaches (shallow waters) is also another weakness in optical images that could be eliminated by fusion. Since, in the event of precipitation or the presence of clouds during optical imaging, the use of a radar image (that does not depend on weather conditions) could be a good solution.

In this case, the most effective tool is the Synthetic Aperture Radar (SAR), which ensures good spatial resolution observation throughout the day and any weather conditions. Although coastline extraction based on SAR still remain challenging, because: 1) the presence of speckle noise in SAR images, which interferes the interpretation of these images. 2) Lack of difference between land and water properties to the sensor, which depend on the sea conditions and geological materials on surface [4]. One of the main source of errors in radar images is the speckle. Major changes in the gray levels of adjacent pixels in a SAR image is calling speckle. These changes create a granular texture in the image. This noise, have more effects in wavy coast conditions it cause reduction of distinction between water and land. Due to the presence of noise in the images some holes on edges and especially on the coastline area will appear, when using Mallat algorithm for edge detection. Filling these holes requires knowing the prior information about the edges' behavior in images. The Kanizsa triangle shows that eliminating such holes in the edges is done by the human visual system [11]. Consequently, for first time a Wavelet-IHS method was applied in this study for optical and radar images fusion to extract coastline at the study area. For coastline extraction we used Mallat algorithm for edge detection which is based on Wavelet transformation. The advantage of using this method is its high accuracy in edge detection from images.

In fusion techniques, the most significant problem is color distortion. In this study, a fusion method for high-resolution SAR image with medium-resolution multispectral (MS) images was applied to simplify SAR images interpretation. This method is based on IHS (Intensity, Hue, Saturation) fusion method and wavelet transformation, while each of these methods could not produce satisfactory results of SAR and MS images fusion standalone (due to the significant difference in gray value between SAR images and MS). The proposed wavelet-IHS method is to benefit from IHS ability in conserving the spatial resolution and from wavelet, the ability of intensity preserving. So a combination of Wavelet-IHS techniques was proposed to utilize the benefits of Wavelet and IHS techniques for SAR image and multivariate image fusion and to address the shortcomings of these two methods standalone. In this method, IHS was used to integrate multifunctional color information with low spatial resolution with high resolution SAR information and details to achieve a smooth injection of spatial and color features. Wavelet transform is used to produce a new image that has high image intensities and includes spatial details of the original SAR image [6].

A discrete wavelet transform is a fragmentation in spatial-frequency domain that present a flexible multivariate analysis of image [19]. This analysis can reveal the characteristics of a signal or image that other analytical techniques, such as drives, disclose points, discontinuities in higher and similar derivatives will lose out. Wavelet analysis could also filter and reduce noises in signal without any significant data loss. In IHS method, panchromatic (PAN) and MS images are combined, and the RGB space with red, green, and blue colors transforms from a MS image to the IHS space. The intensity (I) is replaced by a PAN image, then the invers transformation is used to obtain the RGB image. A commonly used IHS transformation is based on a triangular color model [18]. In this study we used Haar-Wavelet edge detection and Wavelet-IHS fusion method simultaneously which could lead to better results while this method could have more relative capabilities than any above mentioned reasons.

2. Study Areas and Dataset

2.1 Study area

Qeshm is the largest island in the Persian Gulf and is located in the southern part of Bandar Abbas. This island has three types of sandy, rocky, and muddy beaches that are affected by sea currents, including tides, so that the island's area is changing around 195 km² from the highest to the lowest tide level. Our first study area is the southern part of the island, which includes the Salach port, and has a sandy beach. The geographical coordinate of this studied area are between 22.65° (E) to 22.68° (E) longitude and 55.64° (N) to 55.70° (N) latitude, which cover about 12 km of island's coastline. Sea level changes is differing between 2 and 4 meters depend on tidal periods around Qeshm Island. The waves altitude is maximally up to 1 meter in the south coastal area of Qeshm and will reach up to 3 ~ 5 meters. There are

Table 1: Satellites' specifications comparison

Specification	ALOS	Sentinel-1	CartoSat-1	Landsat-7	Landsat-8
Altitude (km)	691.65	693	617	705	705
Inclination (°)	98.26	98.18	97.87	98.21	98.22
Period (min)	98	98.7	94.72	98.83	98.8
Repeat cycle (days)	46	12	116	60	16
Radar Sensor	PALSAR	C-band	N/A	N/A	N/A
Band	L-band (1.27 GHz)	C-band (5.405 GHz)	Pan	Red, NIR,SWIR1	Red, NIR,SWIR1
Wavelength	236 (mm)	555 (mm)	0.5-0.8 (μm)	0.6-1.7 (μm)	0.6-1.6 (μm)
Incidence Angle	8° to 60°	20° to 45°	N/A	N/A	N/A
Spatial Resolution (m)	10	5 (40)	2.5	15 (30)	15 (30)
Swath (km)	70	20 (400)	25(30)	185	185

sea streams affected by sea waves on the margin near the shores of Qeshm, as well as tidal flows, especially in the sea channel between the island and the motherland. In addition to waves effects, sea flows, have an effective impact on coastal erosion and displacement of sediments and land-bed changes, especially for sea canals between the island's Hara forests. The second study area is the westernmost part of the coast in Bandar Abbas province with a geographic coordinate of 27.21° (E) to 27.31° (E) longitude and 52.67° (N) to 52.82° (N) latitude. This area includes the port of Tien (eastern part of Asaluyeh) which has mostly rocky beaches.

2.2 Dataset

In order to detect and extract the coastline, radar and optical satellites data have been used in the regions. Radar images are extracted from the PALSAR sensor of ALOS satellite (in 2007 and 2009) also Sentinel-1 satellite (in 2016). For optical data Landsat-7 (in 2007 and 2009) and Landsat-8 (in 2016) were used. The images of these satellites are roughly in same dates as radar images, and have 3, 4, and 5 bands with a resolution of 30 meters, as well as a pan-chromatic band with 15-meter resolution. The high-resolution image of CartoSat-1 (IRS-P5) satellite is used for results evaluation and to determine the accuracy of coastline detection. For this purpose, a panchromatic band of IRS images with spatial resolution of 2.5 was considered. In the southern part of Qeshm Island, images of three different periods were used. For the years 2007 and 2009, the ALOS images and for the year 2016, Sentinel-1 images were used. The ALOS images are descending and have HH and HV dual polarimeter. The Sentinel-1 image is also in single-polar VV mode. Table 1 shows specifications of used satellites in this study. In second study, two different periods of images have been used. The ALOS and Sentinel-1 images, which has a VH and VV polarimetry. Table 2 indicates the data acquisition date and time in different study areas and for different sources of data.

The PALSAR sensor operates in the L band, which creates waves about 10 cm. It has a multi-polarimetric and a ScanSAR mode. Therefore, it is expected that the collected data by this system will contribute to a new research lines. While the Sentinel-1 mission includes C-band imaging and operates in four unique imaging modes with different resolutions (less than 5 meters) and different coverage (up to 400 kilometers)

3. Methodology

To distinguish the edges and body, the scale of the object must also be considered, this will lead to image wavelet analysis. The edges can be defined as the maximal absolute value of the image wavelet spectrum. In order to reveal edges, the Haar-Wavelet analysis was applied using the algorithm provided by the Mallat, S. G., (1989). Automated coastline extraction was used by MATLAB in three images (radar, optical and fussed image) in this study. A Wavelet-IHS model was applied for image fusion. Due to using two sensors for fusion, the images must be in a same coordinate system before processing. In addition, a sensor is rotated slightly away from its

Table 2: Acquisition date and time of satellite images

Region	Radar Image		Optic Image		IRS Image
Qeshm	ALOS	19/7/2007 18:50	Landsat-7	10/7/2007 06:35	N/A
	ALOS	24/7/2009 18:52	Landsat-7	15/7/2009 06:36	10/06/2009 6:56
	Sentinel-1	31/8/2016 06:39	Landsat-8	27/8/2016 06:45	N/A
Asaluyeh	ALOS	12/7/2007 19:01	Landsat-7	8/7/2007 06:48	18/02/2007 7:11
	Sentinel-1	13/11/2016 17:29	Landsat-8	13/11/2016 06:58	N/A

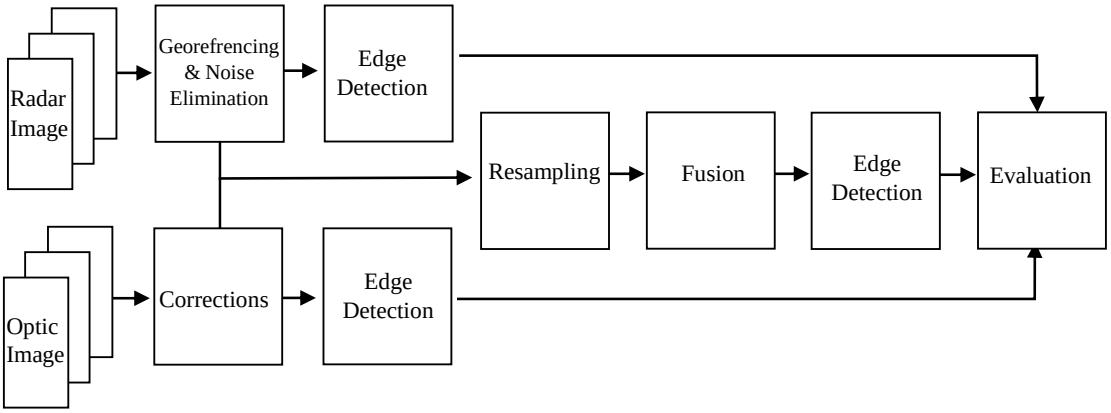

Figure 1: Schematic diagram of applied methodology

orbit every time, and therefore for comparison of images in different years we also need to co-register the images. In order to find the coastline displacement over the course of several years, we have to do the co-registration two times. Finally, the coastline displacements were identified using these images fusion. Below diagram (Figure 1) illustrated applied methodology of our study.

3.1 Pre-processing

Pre-processing for Radar images include speckle noise reduction and geo-referencing of the images. Landsat images should then be co-registered with radar images, the pre-processing steps are mentioned as below:

3.1.1 Speckle Noise Reduction

To reduce and eliminate speckle noise in radar images, the Refined-Lee filter was applied by NEST software for all ALOS and Sentinel-1 radar images in different years and in both HH and HV bands.

3.1.2 Geo-referencing

After the speckle noise reduction in radar images, we must do geo-referencing. Their coordinate system is the UTM WGS84 and should be referenced using ground control points which include in image's file. This process was also performed using the Nearest sampling method by NEST software.

3.1.3 Co-registration

In the next step, optical and radar images should be co-registered. So the Landsat images get co-registered based on radar images, but before that, they should be resampled. The spatial resolution of the panchromatic band of Landsat is 15 meters and the other bands are 30 meters. Considering the spatial resolution of the ALOS images is 12.5 meters, Landsat images get resampled to 12.5 meters then they get stacked together using Envi software. The spatial resolution of the Sentinel-1 image is also 10 meters and the final resolution of Landsat image considered the same (10 meters). In next step Landsat images get co-registered based on radar images using ArcGIS.

3.1.4 Tidal effect

The tidal effects could make changes in position of the coastline at different hours in a day. In this study, the tidal data of nearest tide gauge close to our study area were considered. Tidal effect at the moment of shooting two optical and radar images (7:00:00 – 19:00:00) have almost equal effect in the region according to the 12 hours' interval (Figure 3) which was considered the same.

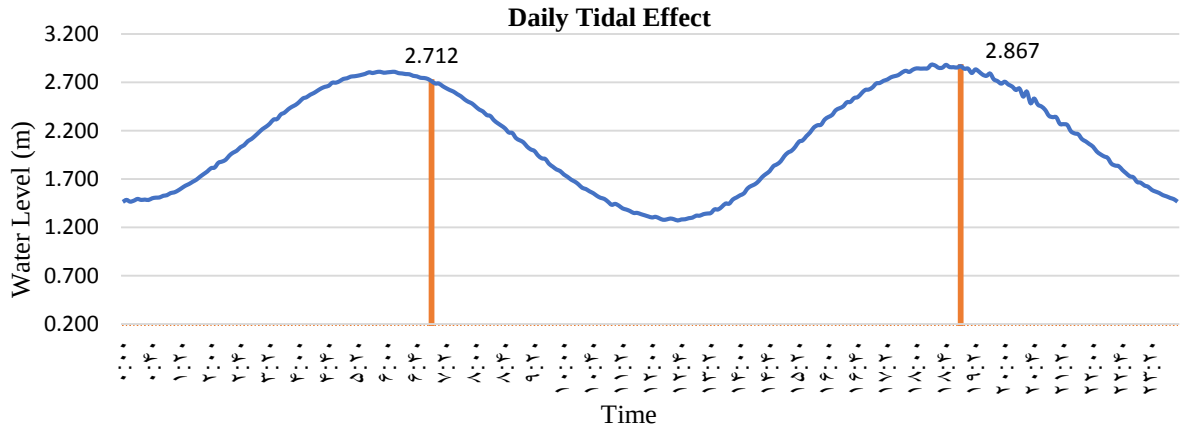

Figure 2: Daily tidal effect over study area

3.2 Coastline extraction

We applied two methods in order to detect the coastline. Firstly, we extracted the coastline from each Landsat image and the radar separately using the wavelet method. then we did the fusion of Landsat and Radar images using the Wavelet-IHS method and then extract the coastline from the fussed image with the wavelet method. Then we compare the lines obtained from the three images and interpret the results.

3.2.1 Coastline extraction using Landsat and Radar Image

After images pre-processing, we extracted the coastline from each Landsat and radar images separately. For optical image, Landsat Panchromatic Band was used for coastline extraction. In radar images, there are two HH and HV bands, multiply of this two bands were used to increase the distinction between water and land. The implementation algorithm process using MATLAB are described as below:

1. Wavelet algorithm was applied in order to extract the edges in both images
2. The Isodata method was used to binary images. The remaining noises is removed using morphology analysis.
3. The detected edges in output image contains all available edges in study area and our goal is to extract the coastline from them. The binary image was segmented by Watershed method. Using this method, the segments larger than 8 pixels are labeled as a single segment.
4. In the segmentation result, the water and land regions are the largest components of image. We used the maximum likelihood method to convert the image to an image that only contains two pieces of water and land regions.
5. At this point, the coastline was extracted from the image. From the existing edges, the coastline was assumed to be the edge that one side is water and other side is land.
6. Finally, in order to have a better shape, we have made the coastline smoother using morphology analysis.

To evaluate coastline extraction visually, the obtained automated coastline was compared with the original image. The Figure 3 through Figure 7 confirm that mostly the extracted coastline form Landsat image has better agreement with the original image, and obtained line from the ALOS image shows some errors mainly due to the speckle noise. The obtained edge (which assumed to be the coastline) has discontinuities and holes. A mathematical morphology technique has been applied to interpolate it, which would eliminate the existing dock (in ALOS 2007) and will make errors in some parts of the coastline. As shown in Figure 4 (b) the extracted coastline using radar image has dislocation in three parts compare to the actual coastline, which is caused by applying the morphology.

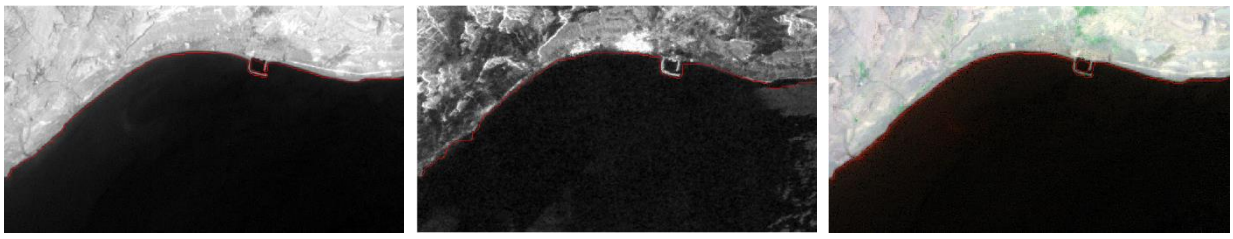

(a) (b) (c)

Figure 3: Extracted coastline in 2007 using a: Landsat-7 b: ALOS c: Fused images in Qeshm area

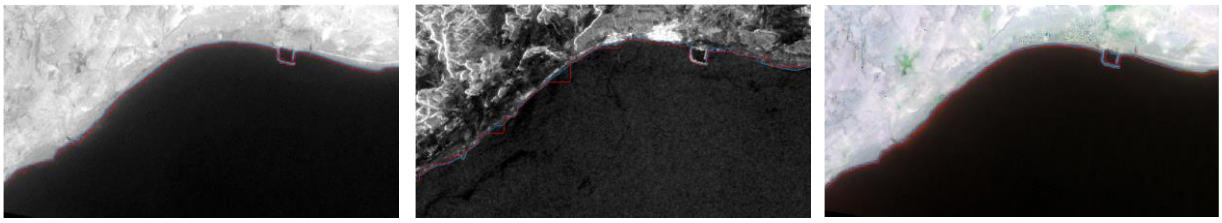

(a) (b) (c)

Figure 4: Extracted coastline in 2009 using a: Landsat-7 b: ALOS c: Fused (red line) images in Qeshm area compare to hand drawn line (blue line)

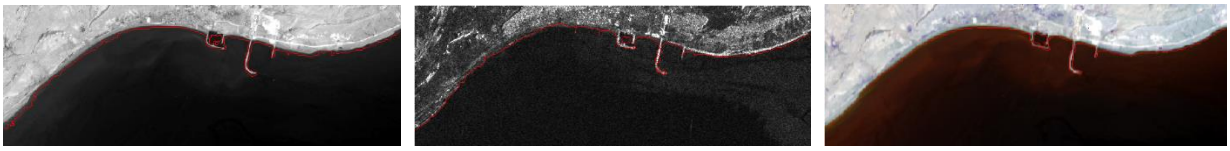

(a) (b) (c)

Figure 5: Extracted coastline in 2016 using a: Landsat-8 b: Sentinel-1 c: Fused images in Qeshm area

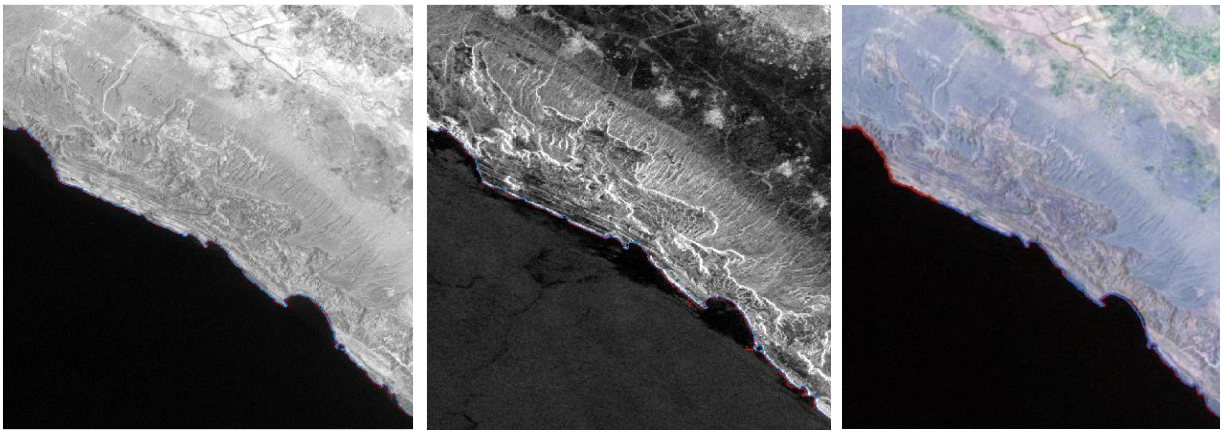

(a) (b) (c)

Figure 6: Extracted coastline in 2007 by a: Landsat-7 b: ALOS c: Fused images (red line) in Asaluyeh area compare to hand drawn coastline (blue line)

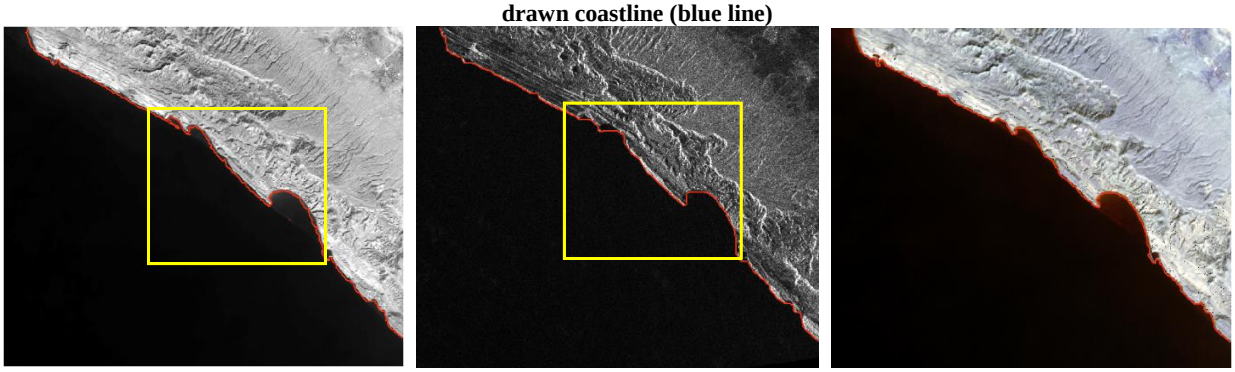

(a) (b) (c)

Figure 7: Extracted coastline in 2016 by a: Landsat-8 b: Sentinel-1 c: Fused image in Asaluyeh area

3.2.2 Coastline extraction using fused image

In this study, an intermittent image fusion method has been applied for SAR images and low-resolution optical images fusion to enhance the interpretation capability of SAR images, which was also described by Hong, G., *et al.* (2009). The goal is to keep the high resolution of SAR images while the spectral information of the optical image remains unchanged. To achieve this goal, The Wavelet-IHS methods has been developed for fusion while:

1. Wavelet transformation method can maintain the spectral information of optical image, but artifacts are visible in results [22].
2. IHS method could saves the spatial information of high-resolution images well, but the color quality strongly depends on sampling of high-resolution image and the image of intensity of low-resolution optical image [20].
3. The Wavelet-IHS fusion method is more desirable than each of the unique methods as it avoids the above mentioned issues.

After coastline detection by each of the Landsat and radar images, the coastline detection is also done by image fusion. To do this, HH and HV bands firstly fused by Wavelet algorithm in order to gain the advantage of polarimetry, and then the image is fused using Wavelet-IHS with bands 3, 4, and 5 of Landsat image.

The fusion results showed that the proposed integration method could display spatial data from SAR images and spectral information from optical image well in a single fused image. The colors in all compilation results are close to the original MS images and the details are similar to the SAR image. Compared to the original SAR data, it can be seen that the coatings are interpreted in a simpler and more accurate image than original data.

The IHS fusion method stand alone could save the spatial information of the SAR image, but there will be color distortion in comparison with the MS image [6]. The standalone Wavelet method can enhance spatial information, however, severe color distortion is also created in the result and the whole image looks gray as SAR image is evenly injected into each of multiple bands of MS image. In Wavelet-IHS fused image, the coastline is better interpreted due to color combination and spatial details. For example, in SAR data, we have difficulties in objects interpreting in parts of the image, but in output fused image, the objects could be easily interpreted cause of their color and clarity. The colors in the fused image is very close to Landsat main image, and are also clear as the original SAR data. This shows that MS and SAR images are well fused. The final extracted coastline in 2009 and 2016 for the Qeshm area as well as the years 2007 and 2016 for the Asaluyeh region was shown in Figure 3 through Figure 7. In

Figure 8 (sub-section of Asaluyeh 2007) and Figure 9 (sub-section of Qeshm 2009) the difference between the extracted coastline by optical and radar images is distinguishable.

4. Results and Discussions

Manually drawn coastlines on radar and optical images was used for evaluation and precision estimation of automated extracted coastline. Also for fused images evaluation we used manually drawn coastline on high resolution IRS images in Qeshm 2009 and Asaluyeh 2007. Thus, difference between the lines derived from the algorithm and the hand drawn line is calculated and considered as final precision (Table 3).

Table 3: Coastline extraction precisions in pixels

Region	Year	Optical Image	Radar Image	Fused Image
Qeshm	2007	2	5.5	-
	2009	3.4	5.5	3.2
	2016	4.6	3.3	-
Asaluyeh	2007	2.1	3.4	2.98
	2016	4.6	4.3	-

In Qeshm area, difference between the drawn coastline on IRS image and extracted line by algorithm in Landsat and radar images in 2009 stand alone are respectively 3.4 and 5.5 pixels (Figure 4). Given the precision of fused image, which is 3.2, it can be concluded that the image fusion improved accuracy. Considering the extracted coastline in 2009, radar image is comparable in some parts of the coast and also has a large difference in another area, we choose a part of the image that has good agreement (Figure 9), then calculate the extraction accuracy for all three Landsat, radar and fused images.

In Asaluyeh area (2007), the difference between the drawn coastline and extracted coastline in Landsat, radar and fused images are respectively 2.1, 3.4 and 2.98 pixels (Figure 6). In this area, we select two smaller parts of the original image and calculate the accuracy of extracted coastline for each of the three images (Figure 8). In sub-section (1-1) of this region, the precision of Radar, Landsat and Fused images are respectively 2.55, 2.30 and 2.52 pixels, which indicates improvement in precision of extraction after

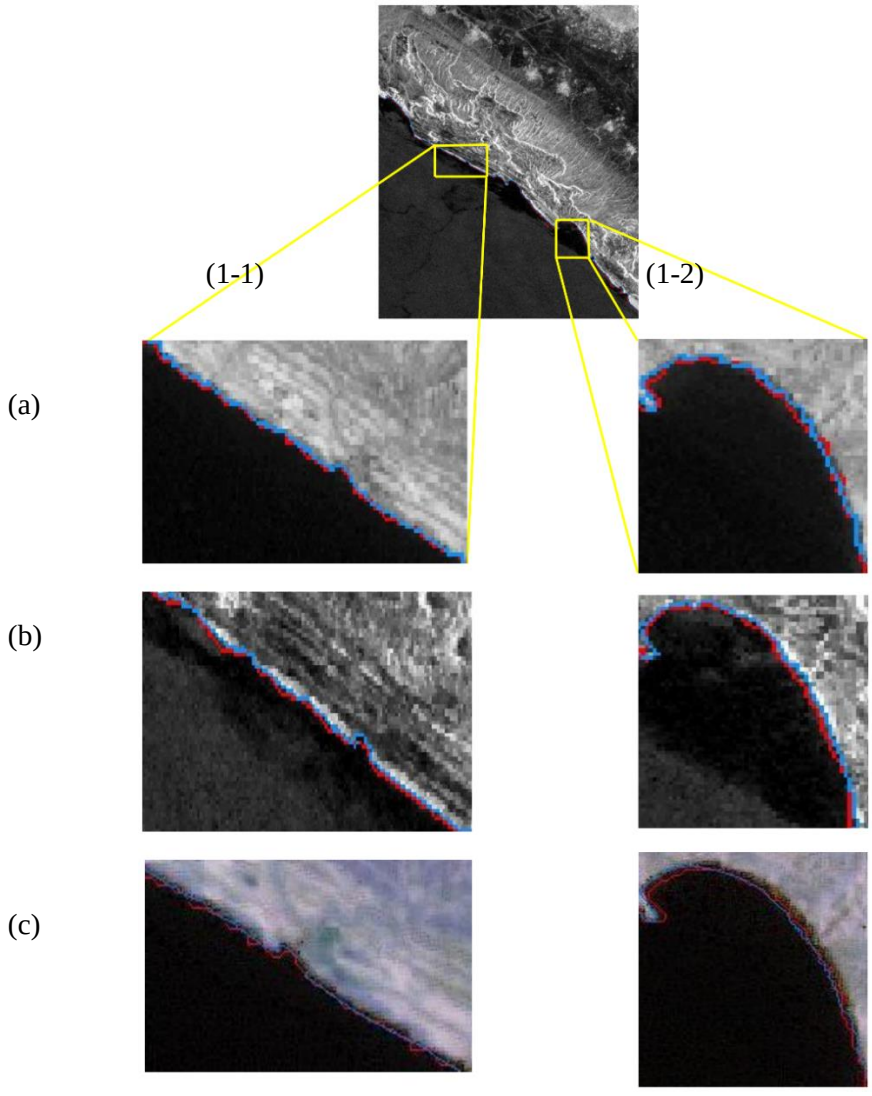

Figure 8: Two sub-section of extracted coastline in Asaluyeh 2007 by a: Landsat-7 b: ALOS c: Fused images (red line) compare to hand drawn coastline (blue line)

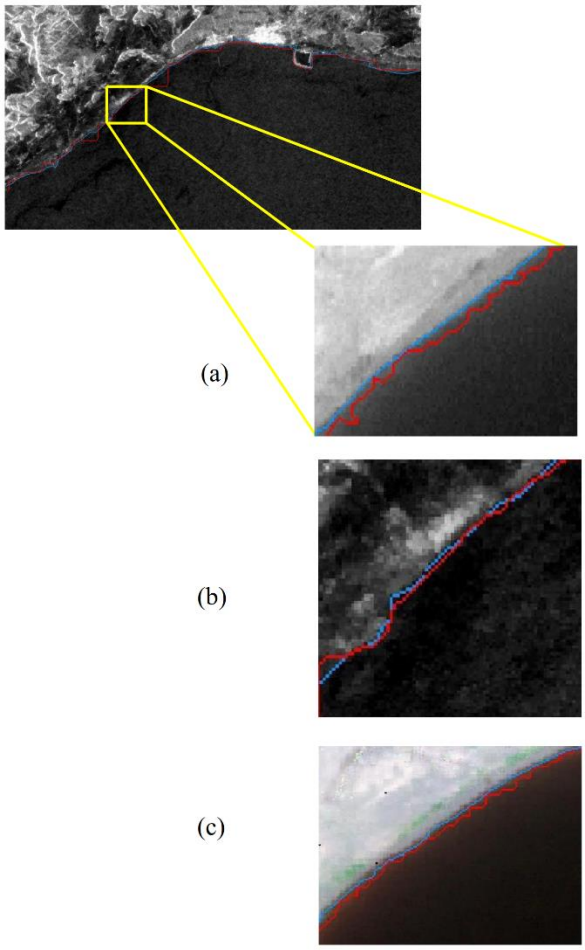

Figure 9: Sub-Section of extracted coastline in Qeshm 2009 using a: Landsat-7 b: ALOS c: Fused (red line) images compare to hand drawn line (blue line)

fusion. Also, in sub-section (1-2), the precision of extraction in Radar, Landsat and Fused images are respectively 2.96, 2.66 and 2.58. In this part of image, extraction accuracy in fused image is slightly same as Landsat and ALOS images.

In Figure 9, the obtained accuracy for sub-section (2) in Qeshm area (2009) by Landsat image is 4.86 pixels, for radar image is 1.66 pixels and fused image is 3.54 pixels. These accuracies yield a contradicting result with the precision obtained from the whole image. Here the radar image accuracy is better than the optical image One of the error factors in coastline extraction by optical images is light reflection of the sea bed in coastal area where there is shallow water. This caused a lower accuracy in extraction of coastline using Landsat 8 (Figure 6 (a)) image in 2016 compare to Landsat 7 2007 (Figure 7 (a)) image. This problem is completely removed in fused image (c parts of same figures) and the obtained coastline by images fusion has a better agreement compare to any radar or optical images stand alone. As showed in Figure 7 (yellow squares) the sea bed reflections was detected as coastline using Landsat image.

4.1 Conclusion

Generally, with one exception (Qeshm-2016) the results approved that the coastline detection using optical images (Landsat- Pancreatic Band) is more accurate than Radar images. The results of visual assessment show that, the detected coastline by optical images is more in line with the original image. However, in radar images for some reasons, the 2009 ALOS image in Qeshm there were some abnormalities caused by use of morphology analysis. If we ignore these types of errors in radar images, in other parts of radar image we could see good alignment of extracted coastline compare to original image. This is also clearly visible in radar images of Asaluyeh area. Considering that good agreement was find using optical images in 2007 and 2009 also using radar images in 2016, it can be concluded that applied method in this study for image fusion will improve coastline extraction precision. In fact, using fusion method, if not even increasing precision, will increase the accuracy of output information.

4.2 Coastline Changes Monitoring

In order to obtain coastline movements during the study period, we used the Near tool in ArcGIS (Figure 10). Thus, the displacement i.e. the average distance between the coastlines in 2007 and 2009 in

Figure 10: Coastline displacement over Qeshm (a) and Asaluyeh (b) area between 2007 (blue line) and 2016 (red line) by automated coastline extraction

the Qeshm area is 32 meters, and average distance between the coastlines in 2007 and 2016 is 37 meters in this region. In Asaluyeh area, this displacement between 2007 and 2016 is 33 meters. Coastline changes in the Qeshm area did not follow a general trend while coastline displacement in Asaluyeh region is depending on the type of beach. The coastline changes in the south of this area, which has a sandy beach, is generally up to the coast, and in the north, which has a rocky coast, it does not show any significant changes. Considering the accuracy of co-registration in this study is around 17 on average, it cannot be said that the mentioned numbers show precise coastline displacement, as they are also including co-registration errors.

4.3 Proposal

The following is recommended for future studies:

1- Use of polarimetric analysis in radar images with full polarimetric data (HH, HV, VH and VV). This method increases the ability of distinction between water and land due to the nature of the transmitted and received waves as well as the type of beach.

2- Use of ground control points to improve the accuracy of image co-registering in the pre-processing stage for fusion and monitoring the changes in different years.

3- Using meteorological and waves data to determine the effect of sea waves on the accuracy of coastline extraction.

4- Choosing a better way for continuity instead of using morphology

5- Coastline detection using different bands (C, L, and P) to determine the best frequency for extracting coastline from radar images on beaches with different classifications and types.

5. References

1- Acar, U., Bayram, B., Balik Sanli, F., Abdikan, S., Sunar, F. and Cetin, H.I., (2012), *An Algorithm for Coastline Detection Using SAR Images*, International Archives of the Photogrammetry, Remote Sensing and Spatial Information Sciences, Volume XXXIX-B3, 2012 XXII ISPRS Congress, 25 August – 01 September 2012, Melbourne, Australia.

2- Adegoke, J.O., Fageja, M., James, G., Agbaje, G. and Ologunorisa, T.E., (2010), *An Assessment of Recent Changes in the Niger Delta Coastline Using Satellite Imagery*. Journal of Sustainable Development, Vol.3(4), p.277-296.

3- Aiazzi, B., Alparone, L., Baronti, S., Garzelli, A. and Selva, M., (2006), *MTF-tailored multiscale fusion of high-resolution MS and Pan Imagery*, Photogrammetric Engineering & Remote Sensing, Vol.72(5), p.591–596.

4- Buono, A. and Mascolo, (2014), L., *A multi-polarization analysis of coastline extraction using X-band COSMO-SkyMed SAR data*, Journal of Latex Class Files, VOL.1(1).

5- Chen, K.S., Wang, H.W., Wang, C.T. and Chang, W.Y., (2011), *A Study of Decadal Coastal Changes on Western Taiwan Using a Time Series of ERS Satellite SAR Images*, IEEE Journal of Selected Topics in Applied Earth Observations and Remote Sensing, Vol.4(4), p.826-835.

6- Hong, G., Zhang, Y. and Mercer, B., (2009) *A Wavelet and IHS Integration Method to Fuse High Resolution SAR with Moderate Resolution Multispectral Images* Photogrammetric Engineering & Remote Sensing, Number 10, p. 1213-1223(11). DOI: https://doi.org/10.14358/PERS.75.10.1213.

7- Inglada, J and Garello, R., (1999), *Depth estimation and 3-D topography reconstruction from SAR images showing underwater bottom topography signatures*, in Proc. IGARSS'99, vol.2, Hamburg, Germany, p. 956–958

8- Lee, J. S and Jurkevich, I., (1990), *Coastline detection and tracing in SAR images*, IEEE Transfer, Geosci. Remote Sensing, vol.28, p. 662–668.

9- Lee, J. S., Grunes, M.R. and De Grandi, G., (1999), *Polarimetric SAR Speckle Filtering and its Implication for Classification*, IEEE Transfer, Geosci. Remote Sensing, Vol.37(5), p.2363-2373.

10- Liu, H. and JEZEK, K.C., (2004), *Automated extraction of coastline from satellite imagery by integrating Canny edge detection and locally adaptive thresholding methods*. International Journal of Remote Sensing, Vol.25(5), p.937–958

11- Mallat, S. G., (1989), *A theory for multiresolution signal decomposition: The wavelet representation*, IEEE

Transactions on Pattern Analysis and Machine Intelligence, Vol.11(7), p.674–693.

12- Mallat, S. G. and Hwang, W.L., (1992), *Singularity detection and processing with wavelets*, IEEE Transfer, Inform. Theory, vol.38, p. 617–643.

13- Mallat, S. G. and Zhong, S., (1992), *Characterization of signals from multiscale edges*, IEEE Transfer, Pattern Anal. Machine Intell., vol.14, p.710–732.

14- Mason, D. C and Davenport, I. J., (1996), *Accurate and efficient determination of the shoreline in ERS-1 SAR images*, IEEE Transfer, Geosci. Remote Sensing, vol.34, p.1243–1253.

15- Nazmfar, H., Fathi, M. H., Sarmasti, N. and Khaliji, M. A., (2013), *Monitoring changes in multi-spectral and multi-temporal satellite data processing Sefidrud Delta*, Conference: International conference on Sensors and Models in Photogrammetry and Sensing (SMPR2013), At Iran, Volume: 2nd.

16- Niedermeier, A., Romaneessen, E. and Lehner, S., (2000), *Detection of coastlines in SAR images using wavelet methods*, IEEE Transactions on Geoscience and Remote Sensing, Vol.38, p.2270–2281.

17- Ouyang, Y., Chong, J. and Wu, Y., (2010), *Two coastline detection methods in Synthetic Aperture Radar imagery based on Level Set Algorithm*, International Journal of Remote Sensing, Vol.31(17-18), p.4957-4968.

18- Qiu, Z.C., (1990), *The study on the remote sensing data fusion*, Acta Geodaetica et Cartographica Sinica, Vol.19(4), p.290–296.

19- Sahu, V. and Sahu, D., (2014), *Image Fusion using Wavelet Transform: A Review*, Global Journal of Computer Science and Technology, Global Journals Inc. (USA), ISSN: 0975-4172 & Print ISSN: 0975-4350, Vol. 14 Issue 5 Version 1.0.

20- Svab, A., and Ostir, K., (2006), *High-resolution image fusion: Methods to preserve spectral and spatial resolution*, Photogrammetric Engineering & Remote Sensing, Vol.72(5), p.565–572.

21- Wang, Y. and Allen, R. T., (2008), *Estuarine shoreline change detection using Japanese ALOS PALSAR HH and JERS-1 L-HH SAR data in the Albemarle-Pamlico Sounds, North Carolina, USA*, International Journal of Remote Sensing, Vol.29(15), p.4429-4442.

22- Yocky, D.A., (1996), *Multiresolution wavelet decomposition image merger of Landsat Thematic Mapper and SPOT panchromatic data*, Photogrammetric Engineering & Remote Sensing, Vol.62(3), p.295–303.

23- Zhang, D., L. Van Gool, and Ooosterlinck, A., (1994), *Coastline detection from SAR images*, in Proc. IEEE IGARSS'94.

INTERNATIONAL JOURNAL OF
COASTAL & OFFSHORE ENGINEERING
IJCOE Vol.3/No. 2/Summer 2018 (21-30)

Available online at: http://ijcoe.org/browse.php?a_code=A-10-198-1&sid=1&slc_lang=en

Investigation of Caspian Sea Level Fluctuations Based on ECMWF Satellite Imaging Models and Rivers Discharge

Soheil Ataei H.[1], Amir Jabari Kh.[2*], Amir Mohammad Khakpour [3], Mehdi Adjami[4] and Seyed Ahmad Neshaei [5]

[1] *Ph.D. candidate, Faculty of Civil Engineering, Shahrood University of Technology, Shahrood, Iran; ataei.h.s@gmail.com*
[2*] *Ph.D. candidate, Faculty of Civil Engineering, Shahrood University of Technology, Shahrood, Iran; amir.jabarikh@gmail.com*
[3] *Master of Sciences, Faculty of Civil Engineering, Shahrood University of Technology, Shahrood, Iran; amirmohammad.khakpour@gmail.com*
[4] *Assistant Professor, Faculty of Civil Engineering, Shahrood University of Technology, Shahrood, Iran; adjami@shahroodut.ac.ir*
[5] *Associate Professor, Department of Civil Engineering, Faculty of Engineering, University of Guilan, Rasht, Iran; maln@guilan.ac.ir*

ARTICLE INFO

Article History:
Received: 6 Feb. 2018
Accepted: 8 Sep. 2018

Keywords:
Sea Level Change
Precipitation and Evaporation
Caspian Sea
Volga River
ERA-Interim

ABSTRACT

Due to the great importance of sea level changes especially for coastal regions, identifying and studying the factors affecting these variations makes it easier to predict changes of sea level and will help to determine the riparian zone and changes in coastal lines. In this research, precipitation-evaporation is studied based on ERA-Interim model of ECMWF in order to estimate changes in Caspian Sea (**CS**) level and the validity of the results is evaluated in a period between 1980 to the end of 2015. Recorded data about the rivers entering the **CS** were also studied for better prediction of changes in water level. According to satellite and software analyses, in average evaporation has increased with a rate of 0.89 $Km^3/year$, while precipitation and rivers discharge have decreased by the rates of 1.09 $Km^3/year$ and 1.41 $Km^3/year$, respectively during the 36 years. The standard deviation of the sea level change caused by Volga discharge (normally entering 249.13 $Km^3/year$ into the sea alone) is closer to the recorded standard deviation obtained from change of **CS** level than the other two factors. Also, the lowest and the highest correlation coefficients relative to the recorded sea level changes were calculated considering simultaneous effect of precipitation-evaporation, and simultaneous effect of all parameters, respectively. As a conclusion, it can be said that the main reason for decreasing the **CS** level during recent years could be attributed to the rise of evaporation in comparison to precipitation and inlet rivers discharges.

1. Introduction

When the mean sea level is measured at different locations of the coast during a long period of time, it is understood that the sea level changes by time. This change is due to the general uplift in the mean sea level, also there is a possibility of tectonic uplift or subsidence of the coast [1].

It is believed that increment of harmful gases in the atmosphere including carbon dioxide has increased the effect of greenhouse gases, the most important of which is the melting of polar ice caps. Global warming and melting of polar ice caps have also affected the average temperature of the free waters and lakes; as a result of which the distance between molecules comprising seawater has increased, which has led to increment water volume and sea level, consequently [2]. There are predictions regarding faster uplift of the general sea level over the next century, which will have significant impact on the coastline, if occur [3, 4].

In this regard, Clark *et al.* [5] reported the world has faced an increase in greenhouse gas emissions in twentieth and twenty-first centuries. Studies also show that today's global warming are related to previous periods. Therefore, greenhouse gas emission and its influence on the weather conditions in the present

century will have detrimental effects in the future as well.

Gornitz *et al.* [6] have also stated that a significant range of sea level change is linked with the impact of human factors on the hydrological system of the Earth. Creating more runoffs by deforestation, use of groundwater resources and other factors that increase the sea level by 0.6 to 1 *mm* per year. By storing water behind the dams, some water is absorbed by the ground and some is evaporated. These factors lower the sea level by 1.5 to 1.8 *mm* per year. The net rate of sea level changes caused by humans is reduction of about 0.8+0.4 *mm* per year. However, it could be observed that the actual sea level increases by 1 to 2 *mm* per year which suggests the existence of other factors.

Changes of lakes water levels (both small and large), depend on other factors in addition to global warming. The level of the Caspian Sea has changed enormously in different time periods. Changes of the Caspian Sea level may be due to several different factors such as global warming, changes in river flows, regional precipitations, evaporation, wind stress, changes in seabed morphology, changes in the pattern of atmospheric transport and human activities such as construction of dams on main rivers.

2. The Caspian Sea

The Caspian Sea is situated in a semi-arid area between Russia, Kazakhstan, Turkmenistan, Iran and Azerbaijan (36–47N, 47–54E). Its sea level has lied between 25 to 29 *m* below the mean level of oceans over past 150 years [7].

The Caspian Sea has the area of about 436000 km^2 [8]. The catchment area of the rivers flowing into the Sea is about 3 million km^2 (close to 2% of the global land) and about 80% of the river Discharge into the Sea is from the Volga river, supplying 237 km^3 in average per year [9]. The Caspian Sea geographical position is shown in Figure 1.

Fig. 1. The Caspian Sea geographical position

The main difference between the Caspian Sea and open seas is in the way their levels change. As data show, open seas are continually experiencing rises in their levels, while in the Caspian Sea, there are both periods of rise and fall in water level. From 1977 to 1995, the Caspian Sea experienced a rise of 2.4 *m*, while from 1995 to 2015, it had a 0.8 *m* fall in its level [10]. Variations of the Caspian Sea level from 1980 to 2015 are shown in Figure 2.

3. Atmospheric Forecasting Models and Sea Water level fluctuations

For many years, changes of sea levels caused lots of damages to coastal ecosystems, residential, commercial and administrative, shipping and fishing units in different areas. Thus, studying the factors affecting the sea level changes and prediction of these variations have gained profound importance.

Ignatove *et al.* [11] studied the evolution of the Caspian Sea coasts under condition of sea level rise as a result

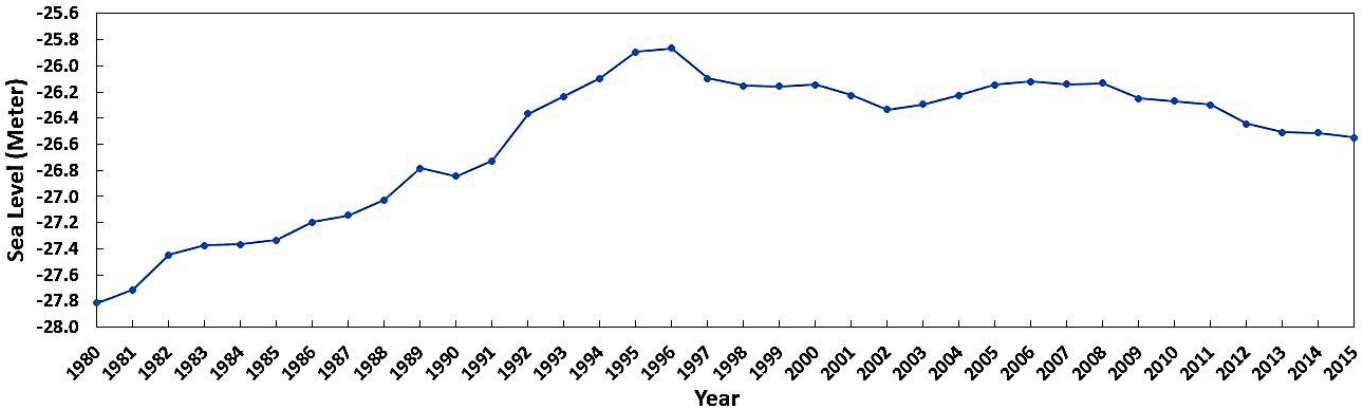

Fig. 2. Caspian Sea levels with respect to the high sea level [10].

of greenhouse gases. They investigated a large number of coasts of Caspian Sea and divided these coasts (with regard to profiles slope ($tg\alpha$)) into 6 major groups including: $tg\alpha \sim 0.0001$, $tg\alpha \sim 0.0005-0.001$, $tg\alpha \sim 0.005-0.01$, $tg\alpha \sim> 0.01$, $tg\alpha \sim 0.01$ and $tg\alpha \sim>> 0.01$. At first slope ($tg\alpha \sim 0.0001$), no dynamical or morphological changes were observed in the coastal zone and in such shores, the waves' energy be dissipated before the water's edge. Under higher inclinations ($tg\alpha \sim 0.0005-0.001$) where the slope is relatively sharp, the zone of wave break will be at some distance from the shoreline. In this case a longshore bar (and eventually a barrier) is formed in the surf zone, creating a lagoon. At third slopes ($tg\alpha \sim 0.005-0.01$), erosion process of the second slope is continued and with more erosion in the offshore slope a bigger barrier beach is developed and shifted toward land backing by a smaller lagoon. In greater inclinations ($tg\alpha \sim 0.01$), there would be no lagoon because the barrier beach is shifting toward the shore line not in the water. The mechanism is changed and one part of beach ridge is on the land and other part moves back to the sea slope, consequently. At the fifth slope ($tg\alpha \sim> 0.01$), due to the increased inclinations, the erosion is started near the shoreline, and the offshore slope is filled up to the equilibrium state by way of accumulation of the material produced by erosion of the coast. Thus, the developing profile consists of an upper erosional part and of a lower accumulation part, *i.e.* it fully agrees with Bruun's scheme. Finally, the last profile ($tg\alpha \sim>> 0.01$) illustrates the evolution of a former erosional coast that became inactive in the regressive period due to formation of the depositional terrace.

Naderi Beni *et al.* [12] studied the changes of Caspian Sea level during the last millennium (900 to 1850) by considering historical and geological documents of southern parts of that. During their investigations, they reconstructed Caspian Sea level with solar irradiance and with the fluctuation of lakes in Middle Asia and Europe, which shows a relatively good agreement between the different curves. Also, based on the anti-phase relationship between the Caspian Sea level changes and the solar irradiance during the last millennium, the main historical Caspian Sea level fluctuations have been caused by solar activities. Their studies showed some disagreements between the curves in some periods, which was due to the absence of data from the Caspian Sea level for that period of time, as well as regional irregularities, such as earthquakes and river avulsions.

The flow of rivers and P-E[1] are the most important factors in changes of the sea levels. Evaporation is so significant that almost all oceans would be dried if rainfall, runoff and groundwater areas' discharge didn't exist. Most of the water evaporating from the oceans returns to the oceans through raining and snowing [13]. Rodionov [14] and Golitsyn [15] stated that evaporation over the Sea is a very important factor of the basin water budget. Elguindi and Giorgi [16] reported over 40% of the total water exchange that affects the Caspian Sea Level is related to evaporation. Different evaporation modeling may have significant effects on predicted changes of the Caspian Sea level.

Renssen *et al.* [17] studied Caspian Sea level changes for the period 8ka to 2100 CE using a mixed model setup representing climate, hydrology and sea level. Their model predicts a drop of 5 *m* between 8 and 5.5ka, which means a decrease from −21.5 meter Baltic Sea level to about −26.5 meter Baltic Sea level. Considering presented documents, the amplitude of this model on the basis of reduction in sea level shows acceptable results, while considering former studies indicates that Caspian Sea level has reached as low as −30 meter Baltic Sea level, which is not reproduced by Renssen's model. They stated that according to the A1b scenario (IPCC Scenario), emission of pollutants caused a 4.5 *m* decrease in Caspian Sea level in the 21st Century mainly due to strong evaporation. The amplitude of this change is of the same order which was simulated for the last 8000 years. On the basis of relatively warm climate of the 21st Century, evaporation becomes the dominant factor of sea level changes in future, whilst during the period 8–5.5ka input from rivers and over-sea precipitation were more considerable in comparison with precipitation.

Cazenave *et al.* [18] performed the required studies with Topex-Posidon satellite altimetry. Results showed an increasing trend in the Caspian Sea level from January 1993 to July 1995 by $18.9\pm 0.5 cm/yr$. However, by moving from the south of the Caspian Sea to the Volga Delta, the trend increases by $3 cm/yr$, demonstrating the dependence of Caspian Sea level on the geographic area. After July 1995, the trend was completely altered, experiencing a downward trend of $-24.8\pm 1.4 cm/yr$. Future Continual measurements can help to determine the transitional or long-term regime of the Caspian Sea level changes; Also, the probable relationship between water level fluctuations and temperature, precipitation, evaporation and rivers discharge may be defined.

Arpe *et al.* [9] studied existence of any relationship between the El-Niño phenomenon and the Caspian Sea level, as well as the prominence of the phenomenon observed in the numerical model. The main feature of the studies conducted by ECHAM4 numerical method software is studying the atmospheric circulation conditions while considering the water surface temperature as the boundary condition.

Arpe *et al.* [7] concluded that summer precipitation in the Volga Basin plays a major role in the sea level

[1] **P**recipitation and **E**vaporation

changes which could explain two major events in the 1930s and 1977s about the minimum and maximum level of the Caspian Sea levels. Also, the El-Niño phenomenon is the only stimulus playing the most important role in changes of sea level during the winter in the Northern Hemisphere. Based on the model, they concluded that: 1- Changes in the level of the Caspian Sea are affected by the Volga basin 2- The observed and modeled cases in the Volga basin are similar 3- Measurements of P-E along the Caspian Sea basin and the evaporation of the Caspian Sea are less than the Volga basin.

Arpe *et al.* [19] have studied the hydrology of the Volga basin and the Caspian Sea considering the effective water balance parameters. The research emphasis on 2010 data when a severe drought developed over European part of Russia. Studies were done on the basis of ECMWF[۲]-ERA interim in the Volga basin and the Caspian Sea which indicates that the difference between precipitation and evaporation over Volga basin during July to September 2010 would decrease the Caspian Sea level by 22 *cm*, of which only 2 *cm* had been observed until the end of September. In fact, the remaining reduction of 20 cm *can* take months to follow if no other anomalies happen.

Arpe *et al.* [20] reviewed variations in the Caspian Sea level and factors affecting it, such as P-E and rivers, using data from ECMWF during a year (2012). Having considered the acceptability of the results according to the analyses, they concluded it is possible to utilize data obtained from ECMWF. Therefore, forecasts could be done for more than 6 months and it would be possible to consider the effect of Volga River runoff as one of the main rivers feeding the Caspian Sea, on the Caspian Sea level changes. In addition to precipitation - evaporation pattern, they have also proposed to consider the effect of watershed and changes in sea level and its relationship with sea surface temperature in forecasting the changes of the sea level.

Chen *et al.* [21] investigated Long-term Caspian Sea level change employed model predictions from the National Centers for Environmental Prediction Climate Forecast System. They studied the impacts of precipitation, evaporation and input from rivers on changes in the Caspian Sea level from 1979 to 2015. According to analysis of data, the model predictions agree very well with observed Caspian Sea level changes. They observed rapid increase in Caspian Sea level (about 12.74 *cm/yr*) and significant drop (~ -6.72 *cm/yr*) during the periods 1979–1995 and 1996–2015, respectively. They showed that increased evaporation rates over the Caspian Sea have played a dominant role in changes in Caspian Sea level.

In order to analyze the P-E, ERA-Interim's data from a subset of Categories of ECMWF [22] information are used. The information is processed based on satellite and 3D analysis software. At each step, the data were monitored and adjusted by methods of error control with high reliability.

4. Rivers Discharge

In addition to the P-E, the rivers inflow and surroundings basins are very important as well. The basins around the Caspian Sea are divided into six categories including Volga Basin with an average flow of 237 Km^3 (about 80%), Kura Araks Basin with an average flow of 17 Km^3 (6.3%), Ural Basin with an average flow of 8.1 Km^3 (About 3%), Terek Basin with an average flow of 7.4 Km^3 (about 2.5%), and basins in Iran and Turkmenistan with an average 8% flow share of the total area per year [9, 23]. Figure 3 indicates the basins of rivers leading to the Caspian Sea based on the ILEC [23] studies.

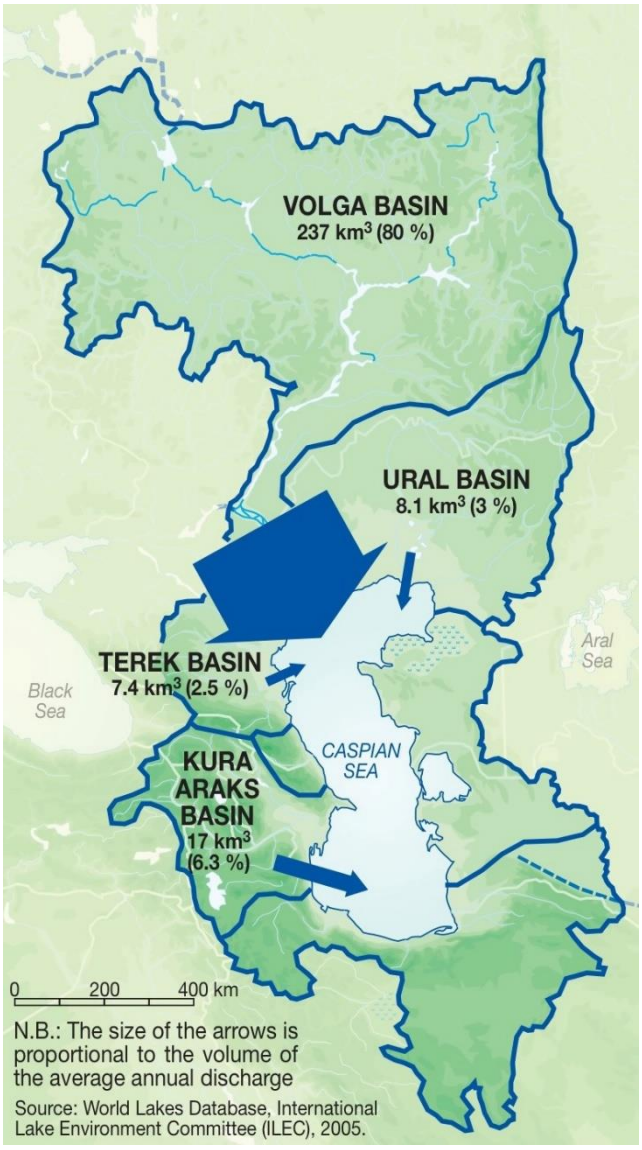

Fig. 3. The basins of rivers leading to the Caspian Sea based on the ILEC [23] studies

[2] European Centre for Medium-Range Weather Forecasts

Table 1. The monthly and annual flows of Volga River with cubic kilometers unit between 1980 and 2015 [24]

Years	Months												Annual Discharge
	January	February	March	April	May	June	July	August	September	October	November	December	
1980	20.6	18.5	21.7	15.9	36.7	31.1	15.5	17.2	17.8	17.3	19.7	20.7	252.69
1981	18.4	19.2	23.1	20.6	56.8	48.0	19.6	17.5	15.1	14.9	17.3	17.9	288.24
1982	16.8	14.1	16.9	15.8	40.2	22.7	15.6	14.7	13.6	16.3	15.4	17.4	219.25
1983	13.8	12.0	16.2	22.6	43.4	18.6	18.3	16.2	15.2	16.7	15.4	17.8	226.28
1984	19.3	19.0	24.4	14.3	35.1	20.0	13.7	14.6	13.8	14.6	15.4	20.4	224.64
1985	21.6	17.3	22.0	18.0	47.1	45.9	26.0	18.6	15.7	16.7	16.4	17.7	282.90
1986	17.6	18.0	21.5	25.5	61.3	33.4	19.2	19.4	17.4	20.4	16.9	18.5	289.24
1987	17.4	15.2	20.0	18.9	43.4	49.5	20.1	16.5	16.1	18.1	18.4	20.0	273.45
1988	13.2	14.8	13.8	16.8	49.6	26.2	17.2	15.2	13.2	14.0	15.8	16.0	225.71
1989	13.4	11.1	13.3	17.7	46.3	27.0	16.3	15.9	14.0	13.8	14.4	19.1	222.19
1990	12.8	11.1	14.6	36.0	53.3	44.8	26.2	16.1	15.8	24.0	29.0	25.0	308.82
1991	18.1	16.2	21.7	38.1	69.1	40.4	19.8	16.2	14.4	14.6	16.6	17.8	302.98
1992	14.7	13.8	19.9	24.4	49.6	31.4	16.2	14.9	14.0	13.6	13.0	14.1	239.70
1993	14.4	14.9	19.4	21.2	52.0	31.9	22.0	20.8	18.5	23.3	22.7	15.3	276.15
1994	16.0	16.5	18.8	29.5	61.9	45.4	35.9	30.3	22.7	19.1	18.6	19.2	333.92
1995	17.8	16.4	20.4	32.9	68.0	33.4	17.8	16.8	15.6	12.9	10.2	11.7	274.07
1996	12.7	13.5	11.2	13.2	31.3	16.6	12.9	13.7	13.3	13.6	12.0	12.1	176.20
1997	12.5	11.7	12.5	13.2	48.5	43.0	20.1	17.4	14.3	13.3	15.6	14.5	236.66
1998	14.2	14.4	17.9	19.6	46.1	51.6	20.4	18.3	19.5	17.8	18.1	19.3	277.11
1999	18.2	19.0	25.3	30.6	57.3	36.5	18.0	18.4	16.5	14.5	12.7	16.4	283.51
2000	11.9	11.4	13.4	18.6	55.4	33.2	20.7	16.5	16.1	15.9	14.4	14.4	242.02
2001	14.5	15.6	21.2	22.1	57.6	44.3	19.9	15.9	15.8	14.5	14.2	17.0	272.68
2002	15.8	15.8	16.4	22.8	52.8	39.7	20.1	15.5	14.1	13.4	12.9	15.2	254.40
2003	17.5	15.6	16.8	20.6	46.3	31.1	18.3	16.7	15.0	15.5	15.0	16.1	244.38
2004	17.0	17.2	16.5	23.4	47.7	27.2	22.4	19.7	15.8	15.8	15.4	17.6	255.60
2005	18.9	17.0	22.2	26.2	61.9	43.3	19.2	17.2	15.4	14.1	12.0	12.9	280.23
2006	12.8	12.9	13.5	11.9	37.2	26.4	15.5	14.1	13.1	13.3	13.2	18.2	202.19
2007	19.0	19.7	28.1	33.4	45.3	36.3	19.5	17.5	15.9	14.9	13.1	13.0	275.67
2008	12.7	12.6	15.7	24.6	49.3	22.3	15.6	15.3	14.3	13.9	13.7	20.0	229.95
2009	19.5	17.3	18.0	16.5	45.8	24.0	15.2	15.3	14.4	13.8	13.3	15.7	228.92
2010	12.2	12.4	14.9	14.0	45.0	26.4	13.1	13.0	11.7	11.6	10.8	11.8	196.97
2011	12.0	11.3	13.4	13.2	43.1	16.5	13.6	13.2	12.6	13.3	12.2	15.3	189.60
2012	13.6	12.9	14.5	13.6	49.6	31.1	16.2	13.6	12.6	12.8	14.7	25.0	230.19
2013	18.9	16.3	18.5	28.0	52.8	36.0	16.2	13.3	12.6	13.2	14.4	17.2	257.46
2014	16.4	15.9	21.5	18.7	42.9	18.0	13.7	12.7	14.0	13.3	12.0	13.3	212.54
2015	12.6	10.9	13.1	11.9	29.7	18.9	13.9	14.2	14.8	13.8	13.1	15.2	181.65

As shown in Figure 3, the Volga River has the highest inflow to the Caspian Sea compared to other basins. According to the data extracted from the CSNRC[3] report [24], the average inflow of Volga River to the Caspian Sea from 1980 to 2015 was 249.13 $Km^3/year$. Regarding the average inflow of 237 $Km^3/year$ (from 1840 to 1980) provided by Arpe *et al.* [9] and the ILEC [23], it is clear that the average inflow of Volga River to the Caspian Sea from 1980 to 2015 has increased compared to previous years. In the studied years, the highest annual flow of Volga River was in 1994, with 333.92 $Km^3/year$, while its lowest annual flow was in 1996, with 176.20 $Km^3/year$. The monthly and annual flows of Volga River within the period of 1980 to 2015 are presented in table 1.

According to the data recorded by CSNRC report [24], Iran basin includes Sefidrood, Polrood, Haraz, Chaloos and Babolrood rivers, and the average inflow of these rivers to the Caspian Sea is 5.33 $Km^3/year$. Accordingly, between 1980 and 2015, the highest annual flow rate of Iran's rivers returns to 1994, with 11.22 $Km^3/year$ and the lowest annual flow rate dates back to 2001, with 1.98 $Km^3/year$. The annual flow rates of Iran's rivers in the period of 1980 to 2015 are listed in table 2.

[3] Caspian Sea National Research Center

Table 2. The annual flow rate of Iran's rivers with cubic kilometers unit in the period of 1980 to 2015 [24]

Years	Sefidrood	Polrood	Haraz	Chaloos	Babolrood	Annual Discharge
1980	4.36	0.39	0.83	0.35	0.42	6.35
1981	5.42	0.52	0.78	0.43	0.35	7.50
1982	3.93	0.51	0.69	0.36	0.41	5.90
1983	4.82	0.44	0.86	0.34	0.55	7.00
1984	3.51	0.60	0.70	0.38	0.68	5.87
1985	5.23	0.44	0.93	0.40	0.60	7.61
1986	2.94	0.35	0.92	0.38	0.49	5.08
1987	4.32	0.54	1.15	0.56	0.59	7.17
1988	8.18	0.61	1.04	0.61	0.76	11.19
1989	2.44	0.38	0.66	0.42	0.41	4.31
1990	2.91	0.48	0.59	0.39	0.49	4.85
1991	2.59	0.34	0.76	0.34	0.47	4.50
1992	6.22	0.61	1.28	0.86	1.05	10.02
1993	5.88	0.57	0.90	0.51	0.73	8.59
1994	8.17	0.72	0.81	0.62	0.91	11.22
1995	4.36	0.45	0.91	0.47	0.39	6.58
1996	5.03	0.47	0.79	0.57	0.63	7.50
1997	2.46	0.36	0.67	0.37	0.63	4.48
1998	3.48	0.52	0.93	0.64	0.53	6.10
1999	0.72	0.19	0.48	0.28	0.42	2.09
2000	1.13	0.25	0.55	0.31	0.53	2.78
2001	0.66	0.29	0.44	0.22	0.37	1.98
2002	1.09	0.36	0.81	0.43	0.58	3.27
2003	3.65	0.64	1.25	0.56	0.66	6.77
2004	2.09	0.56	1.28	0.55	0.55	5.02
2005	2.16	0.57	1.56	0.52	0.53	5.35
2006	1.11	0.39	1.00	0.38	0.42	3.30
2007	2.46	0.58	1.19	0.52	0.59	5.34
2008	1.20	0.28	0.75	0.25	0.34	2.83
2009	0.54	0.48	0.93	0.30	0.52	2.76
2010	1.16	0.37	0.82	0.26	0.22	2.83
2011	1.23	0.56	0.85	0.40	0.25	3.30
2012	1.93	0.48	1.17	0.48	0.26	4.32
2013	1.09	0.30	0.71	0.27	0.48	2.85
2014	0.94	0.38	0.59	0.26	0.30	2.46
2015	1.00	0.43	0.72	0.33	0.33	2.80

5. Analysis of P-E Processes in the Caspian Sea Surface

In this study, information of evaporation and total precipitation containing raining and snowing statistics are analyzed from 1980 to the end of 2015. In order to achieve a higher accuracy in the analysis, the level of the Caspian Sea has been divided into 4 sections. Furthermore, each section is divided into 0.75 * 0.75 degrees, based on the accuracy of surface analysis of the software. In total, the Caspian Sea is divided into 184 levels; and in each year, 134320 data were collected from the sea surface. Table 3 shows the P-E data of the Caspian Sea surface.

Table 3. P-E Data of the Caspian Sea surface area [22]

Years	Volume of Evaporation (Km^3)	Volume of Precipitation (Km^3)	Average column of Evaporation (Cm)	Average column of Precipitation (Cm)
1980	-294.30	161.65	-67.50	37.08
1981	-267.92	170.37	-61.45	39.08
1982	-277.62	157.94	-63.68	36.23
1983	-247.54	136.25	-56.78	31.25
1984	-284.38	144.43	-65.23	33.13
1985	-287.98	140.07	-66.05	32.13
1986	-270.54	112.05	-62.05	25.70
1987	-283.07	142.57	-64.93	32.70
1988	-289.40	158.81	-66.38	36.43
1989	-282.42	120.88	-64.78	27.73
1990	-280.24	133.42	-64.28	30.60
1991	-286.23	132.76	-65.65	30.45
1992	-284.82	148.57	-65.33	34.08
1993	-315.88	141.92	-72.45	32.55
1994	-299.86	137.99	-68.78	31.65
1995	-296.37	112.71	-67.98	25.85
1996	-289.18	124.15	-66.33	28.48

Table 3. P-E Data of the Caspian Sea surface area [22] – Continue

Years	Volume of Evaporation (Km^3)	Volume of Precipitation (Km^3)	Average column of Evaporation (Cm)	Average column of Precipitation (Cm)
1997	-296.81	136.80	-68.08	31.38
1998	-305.09	119.03	-69.98	27.30
1999	-292.12	126.66	-67.00	29.05
2000	-316.97	125.68	-72.70	28.83
2001	-296.81	120.12	-68.08	27.55
2002	-305.31	137.56	-70.03	31.55
2003	-282.64	144.32	-64.83	33.10
2004	-301.71	130.36	-69.20	29.90
2005	-304.33	113.69	-69.80	26.08
2006	-301.17	132.33	-69.08	30.35
2007	-310.32	113.69	-71.18	26.08
2008	-299.97	115.54	-68.80	26.50
2009	-288.74	122.63	-66.23	28.13
2010	-312.18	106.93	-71.60	24.53
2011	-308.69	132.54	-70.80	30.40
2012	-303.13	112.82	-69.53	25.88
2013	-291.47	116.09	-66.85	26.63
2014	-305.09	90.47	-69.98	20.75
2015	-305.09	127.20	-69.98	29.18

According to table 3, in the 36-year period (from 1980 to the end of 2015), based on the ECMWF software and the satellite analysis of the ERA-Interim data series, the highest evaporation rate is observed in 2000, with the rate of 316.97 $Km^3/year$ (72.70 Cm water column), while the least evaporation rate occurred in 1983, with 247.54 $Km^3/year$ (56.78 Cm water column). Also, the highest and lowest precipitations were observed in 1981 and 2014, with 170.37 $Km^3/year$ (39.08 Cm water column) and 90.47 (20.75 Cm water column), respectively. Based on available data, the average evaporation and precipitation rates are 293.15 $Km^3/year$ (67.24 Cm water column) and 130.68 $Km^3/year$ (29.97 Cm water column), respectively. Thus, it could be stated that evaporation rate is more than twice than that of precipitation at the Caspian Sea level, indicating the more significant effect of evaporation than precipitation on the changes of Caspian Sea level.

6. Data Analysis and Discussion

In order to examine the P-E, rivers discharge and scientific measurements between these factors, the histogram in Figure 4 has been drawn.

According to Figure 4, during the 36-years period under study, precipitation is much less than those of evaporation and rivers discharge. During 1980-1994, evaporation occasionally exceeded rivers discharge and vice versa. However; since 1995, evaporation was always more than rivers discharge. In general, evaporation rose with the rate of 0.89 $Km^3/year$, while the equivalent figures for precipitation and river discharge declined at the rate of 1.09 and 1.41 $Km^3/year$, respectively, which aroused concerns. Figure 5 shows independent effect of each parameter (Volga discharge, P-E) on the Caspian Sea level.

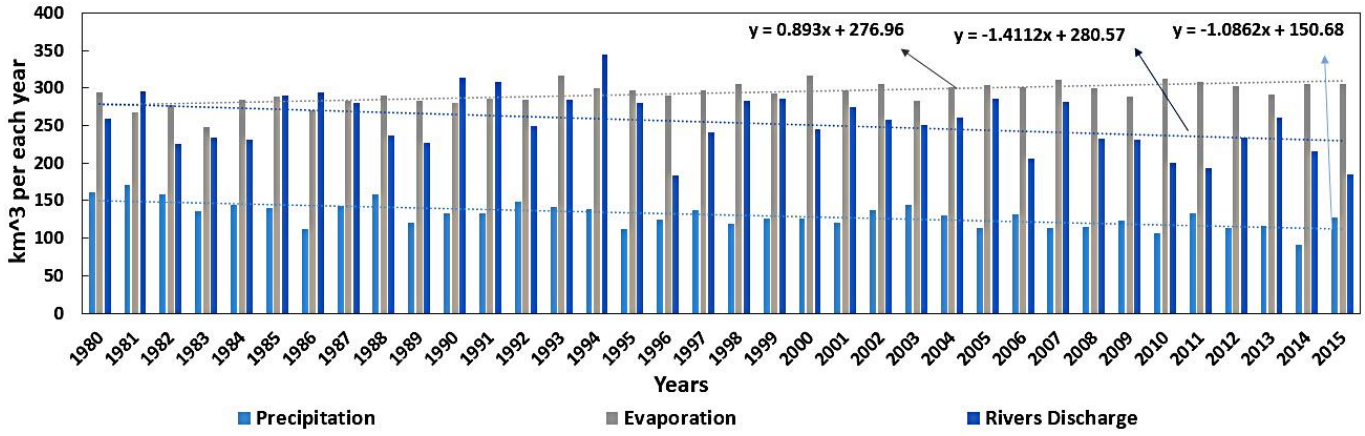

Fig. 4. Annual volumes of rivers discharge and P-E in the Caspian Sea

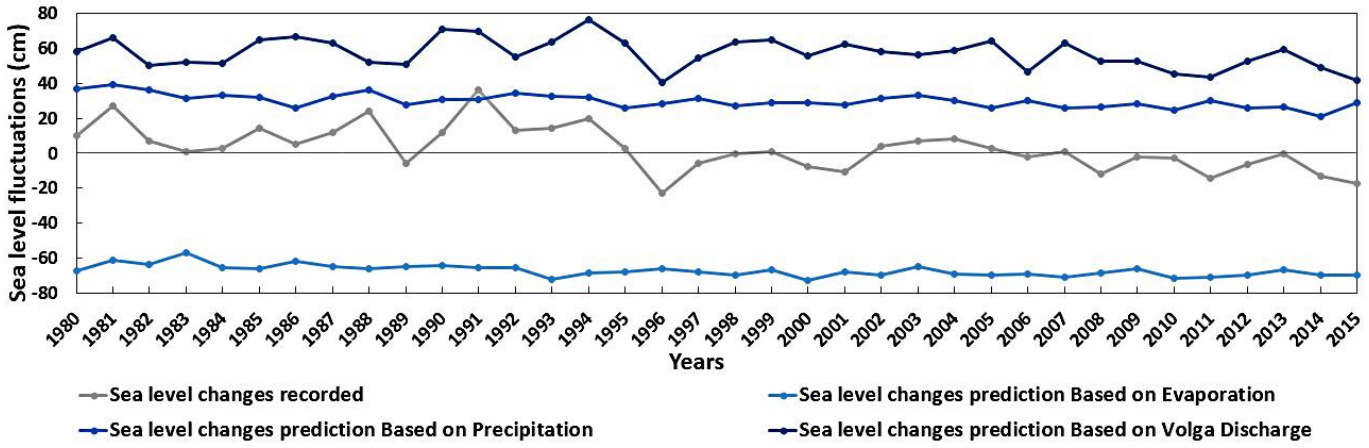

Fig. 5. Independent effect of each parameter (Volga discharge and P-E) on the Caspian Sea level

As Figure 5 suggests, evaporation decreases sea level, while precipitation and Volga discharge increase it. Meanwhile, effect of evaporation and Volga discharge on the Caspian Sea level is much higher than that of precipitation.

One common method for data analysis and proximity of their variations is the standard deviation method, which is as follows:

$$S_N = \sqrt{\frac{1}{N}\sum_{i=1}^{N}(x_i - \bar{x})^2} \quad (1)$$

In Eq. (1), S_N is the standard deviation, N is the number of data and $\bar{x}$ is the mean. Using Eq. (1), the standard deviations for each set of outputs provided in Figure 5 are presented in table 4.

As shown in table 4, the standard deviation of the sea level from Volga discharge is closer to the standard deviation of the recorded Caspian Sea level than other two factors. Based on this study, it could be concluded that Volga discharge is more effective on Caspian Sea level than other factors. Furthermore, changes in Volga discharge can make significant changes in the Caspian Sea level. Therefore, proper ordering and monitoring the Volga discharge process is very important. In order to have a better analysis of the Caspian Sea level, other factors were also evaluated. Approximately 5 cubic kilometers of water seep into the ground each year. Also, 18 cubic kilometers of water are annually entered into the Kara Bogaz Gol Gulf (except for 1982 to 1992, due to closure of the dam) [8].

Simultaneous effect of all mentioned environmental factors were also for more accurate analysis. The change of Caspian Sea level caused by rivers discharge, precipitation, evaporation, water penetration into the land and water outflow through Kara Bogaz Gol Gulf are shown in Figure 6.

Table 4. The standard deviations of each set of outputs shown in Fig. 5

	Sea level changes recorded	Sea level changes prediction Based on Volga Discharge	Sea level changes prediction Based on Precipitation	Sea level changes prediction Based on Evaporation
Standard deviation	12.48	8.43	3.83	3.29

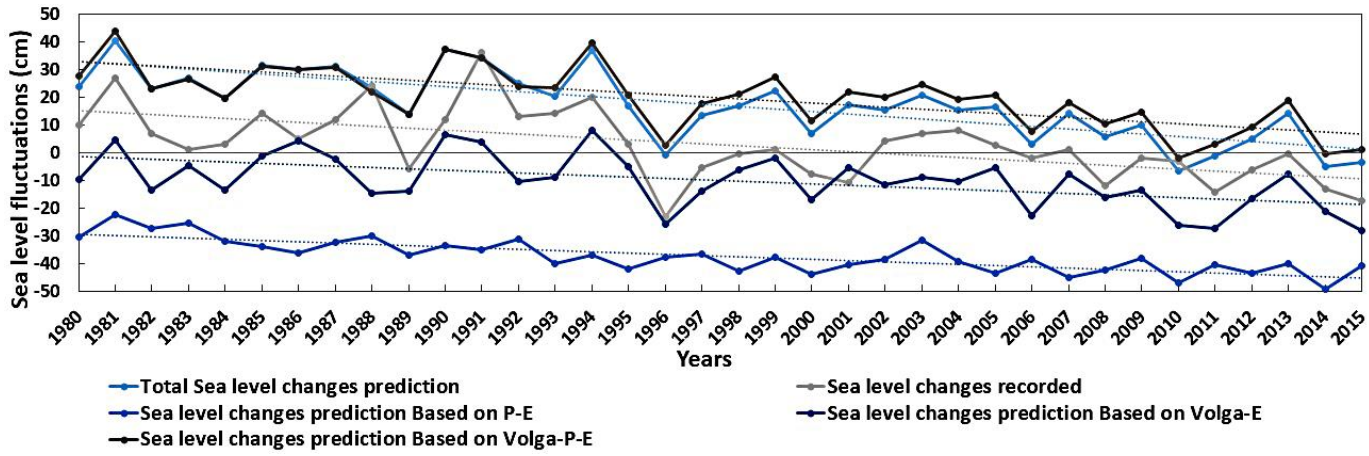

Fig. 6. The Caspian Sea level change due to the rivers discharge, precipitation, evaporation, water penetration into the land and water outflow through Kara Bogaz Gol Gulf

Table 5. The correlation coefficient of each set of outputs shown in Fig. 6, and recorded changes of Sea level

	Sea level changes prediction Based on P-E	Sea level changes prediction Based on Volga-E	Sea level changes prediction Based on Volga-P-E	Total Sea level changes prediction
Correlation Coefficient	56.94%	70.56%	80.30%	82.67%

According to Figure 6, it can be seen that considering simultaneous effect of all parameters, increase of evaporation rate and reduction in precipitation and rivers discharge generally reduced the Caspian Sea level (linear trend line); which is confirmed by the sea level changes recorded in the tide gauge of Anzali port (Sea Level changes recorded parameter in Figure 6). To evaluate the results obtained by effect of environmental factors on sea level with actual recorded changes in sea level, correlation coefficient could be calculated as follows:

$$CC = \frac{\sum_{i=1}^{N}(x_i - \bar{x}) \times (y_i - \bar{y})}{\sqrt{\sum_{i=1}^{N}(x_i - \bar{x})^2 \times \sum_{i=1}^{N}(y_i - \bar{y})^2}} \quad (2)$$

In Eq. (2) CC is the correlation coefficient, N is the number of data of each set, $\bar{x}$ and $\bar{y}$ are data average. Base on Eq. (2) the correlation coefficient of each set of outputs shown in Figure 6, as well as recorded changes of Sea level are presented in table 5.

Based on the results shown in table 5, the lowest correlation coefficient with respect to recorded changes of sea level is obtained for the simultaneous effect of P-E. Also, the highest correlation coefficient is observed for the simultaneous effect of all parameters, with 82.67%.

7. Conclusions

In this research, the P-E of the Caspian Sea have been analyzed based on the ECMWF satellite weather forecast model of. Also, the rivers discharge, water infiltration and exfiltration through Kara Bogaz Gol gulf bed, between 1980 and 2015, have been investigated. Due to the great importance of sea level changes especially for coastal regions, identifying and studying the factors affecting these variations makes it easier to predict changes of sea level and will help to determine the riparian zone and changes in coastal lines.

The basins around the Caspian Sea was divided into six categories including: Volga Basin, Kura Araks Basin, Ural Basin, Terek Basin, and Basins in Iran and Turkmenistan. The highest value was observed for Volga Basin with an average flow of 249.13 $Km^3/year$. According to the satellite and software analysis, in the 36-year period, the average evaporation rate was 293.15 $Km^3/year$ and the average precipitation was 130.68 $Km^3/year$. Therefore, it could be stated that evaporation rate has been more than twice the precipitation rate at the Caspian Sea level, indicating more significant effect of evaporation than precipitation on the Caspian Sea level. In the course of the whole period, in average evaporation increased with a rate of 0.89 $Km^3/year$ and precipitation and rivers discharge decreased by the rates of 1.08 and 1.41 $Km^3/year$, respectively.

Standard deviation method was used to assess the effect of each factor on the sea level changes and its validation with regards to the actual sea levels recorded. The standard deviation of the change in sea level caused by Volga discharge was closer to standard deviation of actual recorded amounts than other two factors. Therefore, Volga discharge had more dramatic effect on the process of Caspian Sea level change than other factors. Furthermore, correlation coefficient was utilized to examine the results obtained by effect of environmental factors on sea level with actual recorded changes in Sea level. Based on the results, the lowest correlation coefficient with respect to actual recorded changes of sea level was obtained for the simultaneous effect of P-E. Also, the highest correlation coefficient was observed for the simultaneous effect of all parameters, with 82.67%.

Based on the available analyses it can be concluded that the ERA-Interim series of ECMWF set does not have sufficient accuracy for scientific studies and accurate forecasts of Caspian Sea level changes. However, it could be devised for long-term review and forecasting the Caspian Sea level changes. In particular, the current study shows that the main reason for decreasing the Caspian Sea level during recent years could be attributed to the rise of evaporation in comparison to precipitation and inlet rivers discharges.

Acknowledgments

The authors would like to acknowledge support given by the European Centre for Medium-Range Weather Forecasts and the researchers of ECMWF that have provided Meteorological data of the Caspian Sea basin. Thanks to Iran's Port and Maritime Organization and Iran's Caspian Sea National Research Center that have provided the Long-term sea level changes data and Runoff data of the Caspian Sea basin. Their support is gratefully acknowledged.

8. References

1- Dean, R.G., (1983), *Shoreline erosion due to extreme storms and sea level rise*, Coastal and Oceanographic Engineering Department, University of Florida. http://aquaticcommons.org/id/eprint/1473.

2- Union of Concerned Scientists, (2013), *Storm Surge and High Tides Magnify the Risks of Local Sea Level Rise*. http://www.ucsusa.org/global_warming/science_and_impacts/impacts/causes-of-sea-level-rise.html#.V5yacGh97IU

3- Nicholls, R.J., Cazenave, A., (2010), *Sea-level rise and its impact on coastal zones*, science, 328(5985), 1517-1520. doi: 10.1126/science.1185782

4- Warrick, R.A., Oerlemans, J., (1990), *Sea level rise*, Cambridge University. Climate Change - The IPCC Scientific Assessment, pp. 257 – 281.

5- Clark, P.U., Shakun, J.D., Marcott, S.A., Mix, A.C., Eby, M., Kulp, S., Schrag, D.P., (2016), *Consequences of twenty-first-century policy for multi-millennial climate and sea-level change*, Nature Climate Change. doi: 10.1038/nclimate2923

6- Gornitz, V., Rosenzweig, C., Hillel, D., (1997), *Effects of anthropogenic intervention in the land hydrologic cycle on global sea level rise*, Global and Planetary Change, 14(3), 147-161. doi: 10.1016/S0921-8181(96)00008-2

7- Arpe, K., Leroy, S.A., (2007), *The Caspian Sea Level forced by the atmospheric circulation, as observed and modeled*, Quaternary International,173, 144-152. doi: 10.1016/j.quaint.2007.03.008

8- Ieva, R., Otto, S., (2011), *Vital Caspian Graphics 2 Opportunities, Aspirations and Challenges*, Zoi Environment Network and GRID-Arendal.

9- Arpe, K., Bengtsson, L., Golitsyn, G.S., Mokhov, I.I., Semenov, V.A., Sporyshev, P.V., (2000), *Connection between Caspian Sea level variability and ENSO*, Geophysical research letters, 27(17), 2693-2696.

10- Ports and Maritime Organization report, (2016), *Caspian Sea Level Changes*, Ministry of Roads & Urban development of I.R. Iran. http://www.pmo.ir/en/home

11- Ignatov, Y.I., Kaplin, P.A., Lukyanova, S.A., Solovieva, G.D., (1993), *Evolution of the Caspian Sea Coasts under Conditions of Sea-Level Rise: Model for Coastal Change under Increasing" Greenhouse Effect"*, Journal of coastal Research, 104-111.

12- Naderi Beni, A., Lahijani, H., Mousavi Harami, R., Arpe, K., Leroy, S.A.G., Marriner, N., Reimer, P.J., (2013), *Caspian Sea-level changes during the last millennium: historical and geological evidence from the south Caspian Sea*.

13- Eghtesadi, S.H., Zahedi, R., (2012), *Study of factors affecting the South Caspian Sea level fluctuations*, Journal of Marine Science and Technology, 10 (3), 4-13 (In Persian).

14- Rodionov, S., (1994), *Global and regional climate interaction: The Caspian Sea experience (Vol. 11)*, Springer Science & Business Media.

15- Golitsyn, G.S., (1995), *The Caspian Sea level as a problem of diagnosis and prognosis of the regional climate change*, Izvestiya, Atmospheric and Oceanic Physics, 31(3), 366-372.

16- Elguindi, N., Giorgi, F., (2006), *Projected changes in the Caspian Sea level for the 21st century based on the latest AOGCM simulations*, Geophysical research letters, 33(8). doi: 10.1029/2006GL025943

17- Renssen, H., Lougheed, B.C., Aerts, J.C.J.H., De Moel, H., Ward, P.J., Kwadijk, J.C.J., (2007), *Simulating long-term Caspian Sea level changes: the impact of Holocene and future climate conditions*, Earth and Planetary Science Letters, 261(3), 685-693.

18- Cazenave, A., Bonnefond, P., Dominh, K., Schaeffer, P., (1997), *Caspian Sea level from Topex-Poseidon altimetry: Level now falling*, Geophysical Research Letters, 24(8), 881-884.

19- Arpe, K., Leroy, S.A.G., Lahijani, H., Khan, V., (2012), *Impact of the European Russia drought in 2010 on the Caspian Sea level*, Hydrology and earth system science, 16, 19-27.

20- Arpe, K., Leroy, S.A.G., Wetterhall, F., Khan, V., Hagemann, S., Lahijani, H., (2013), *Prediction of the Caspian Sea level using ECMWF seasonal forecasts and reanalysis*, Theoretical and applied climatology, 117(1-2), 41-60. doi: 10.1007/s00704-013-0937-6

21- Chen, J.L., Pekker, T., Wilson, C.R., Tapley, B.D., Kostianoy, A.G., Cretaux, J.F., Safarov, E.S., (2017), *Long-term Caspian Sea level change*, Geophysical Research Letters, 44(13), 6993-7001.

22- European Centre for Medium-Range Weather Forecasts, (2016), *Precipitation and Evaporation data in the Caspian Sea*, http://www.ecmwf.int

23- International Lake Environment Committee, (2005), *Annual discharge into the Caspian Sea*, World Lakes Database. http://www.ilec.or.jp/en/

24- Caspian Sea National Research Center report, (2016), *Caspian Sea Profiles*, Water Research Institute, Ministry of Energy of I.R. Iran. http://wri.ac.ir/csnrc

INTERNATIONAL JOURNAL OF
COASTAL & OFFSHORE ENGINEERING
IJCOE Vol.3/No. 2/Summer 2018 (31-44)

Available online at: http://ijcoe.org/browse.php?a_code=A-10-121-3&sid=1&slc_lang=en

System Readiness Level Estimation of Oil and Gas Production Systems

Sirous F. Yasseri[1*], Hamid Bahai[2]

[1]* *Corresponding Author; Brunel University London; Sirous.Yasseri@Brunel.ac.uk;*
[2] *Brunel University London; Hamid Bahai@Brunel.ac.uk*

ARTICLE INFO

Article History:
Received: 1 Jul. 2018
Accepted: 8 Sep. 2018

Keywords:
Oil and Gas Production system
Technology readiness level
Integration readiness level
System readiness level
System Architecture

ABSTRACT

This paper explores further and describes the System Readiness Level estimation for means of production in the oil and gas industry, through a case study. The concept as Technology Readiness Level (TRL) originally promoted by NASA and was then adopted by government agencies and industries across the USA and Europe. TRL was adopted by API (API 17N) and tailored for the assessing the readiness of subsea components for inclusion in subsea production systems. The API's TRL has been recently extended by introducing two more metrics namely, the Integration Readiness Level (IRL) and the System Readiness Level (SRL). SRL is a mathematical combination TRL and IRL and is a metric for assessing progress in developing major subsea systems.
Standard assessment metrics, such as Technology Readiness Levels (TRL), do not sufficiently evaluate the modern complex systems. Building on the previous publications [43] the SRL calculation method is expanded and expounded by adding a system engineering framework for the process of SRL estimation. Explained in some detail, in this paper, which produces more consistent results. Using an error averaging method, SRL is calculated by combining the TRL of each component with IRL, which expresses the readiness of each of these components to be integrated with other components of the system. To facilitate the calculation the Design Structure Matrix (DSM) is used both to visualise components and perform the necessary arithmetic.

1. Introduction

A better understanding of the technology readiness is critical in making good decisions about the inclusion, development and integration of new technologies in complex engineering projects [34]. The most widely used tool for readiness assessment is the Technology Readiness Level (TRL) scale [6] The TRL scale was first developed at NASA in the 1970s [25] to be a consistent measure and a common understating of the state of development. The scale was originally devised to assist the transition from technology development to space mission development [39].
Following initial implementation within NASA in the '70s, the technology readiness concept was published again in 1989, as a 7-point scale [34]. In 1995, NASA published a refined 9-point scale, along with the first detailed descriptions of each level [4]. Today the TRL approach is being used in multiple industries and serves a similar purpose but in a broader context. Commercial implementations of the TRLs are similar to NASA's 9-point embodiment. Figure 1 shows a generic 9 scale TRL definition. The NASA scale begins with a technology in its very basic scientific form and progresses to a technology proven in the required operating environment (Figure 1). Thus for a generic technology, the levels describe the demonstration requirements, including the environment and technology assembly status, gradually conforming to the final operating system as the design evolves.
Various definitions of "technology" exist at many different scales, namely components, modules of the system level. The predominant conceptualization within the TRL-community, at NASA, and used in this paper, is that of a component-technology. The TRL scale is used to assess the maturity of a component (or a principle that will eventually be embodied in a component) that features new materials, scale, or working principles.
The most widely used tool for the readiness assessment is the Technology Readiness Level (TRL) Scale. The TRL Scale was developed to support decision making in relation to the introduction of new technologies during the development of complex systems [24]. Although this scale has been used for decades, it does not reflect well the integration of new technological elements into the system architecture. Its application has other challenges related to system complexity, project planning, and subjectivity and imprecision of

the increasingly realistic testing. Once the technology is sufficiently proven, it can be incorporated into a system/subsystem.

The United States Department of Defence has adopted TRLs for all of its new procurement programs in 2001 [41]. A variety of industries have now generated customized standard guidelines for using TRLs for complex systems development, which includes USA Homeland Security [17], USA Department of Defence (Katz [19]), oil and gas, and infrastructure, e.g. DNV [12] and API [2], ABS[1] and UK Ministry of Defence [13, 19, 28 and 29], Nolte [32] and so on.

System architecture-related extensions to the TRL include Integration Readiness Level (IRL) and system readiness level (SRL), introduced by Sauser and his colleagues [15, 15 and 34 to 38]. Austin [3] provided an example of its application. Yasseri [42] has extended API adaptation of NSA's TRL to include IRL and SRL. These reflect the reality that technologies do not exist in isolation, but rather they are connected through interfaces in the system architecture [45].

This paper differentiates between the system "readiness" and the system "maturity". Following Smith [39] a distinction is made between readiness and maturity by noting that a system considered mature in one context, may not possess sufficient readiness for operation in a different environment. Bilbro [7], used "maturity" as part of the definition of "readiness" and thereby implied a relationship between the two terms. Other authors also used the terms interchangeably; e.g. See Azizian et al. [5].

Table 1 shows API's definition of TRLs. A NASA-type TRL is also included alongside for the comparison purposes. Figure 2 shows a comparison of NASA and API scales.

Generally speaking, when a new technology is first invented or conceptualized, it is not suitable for the immediate application. Instead, new technologies are usually subjected to experimentation, refinement, and increasingly realistic testing. Once the technology is sufficiently proven, it can be incorporated into a system/subsystem. While technology and system development theoretically follow similar maturation paths, ultimately a technology is inserted into a system based on its maturity, functionality, and environmental readiness as well as its ability to integrate with the intended system.

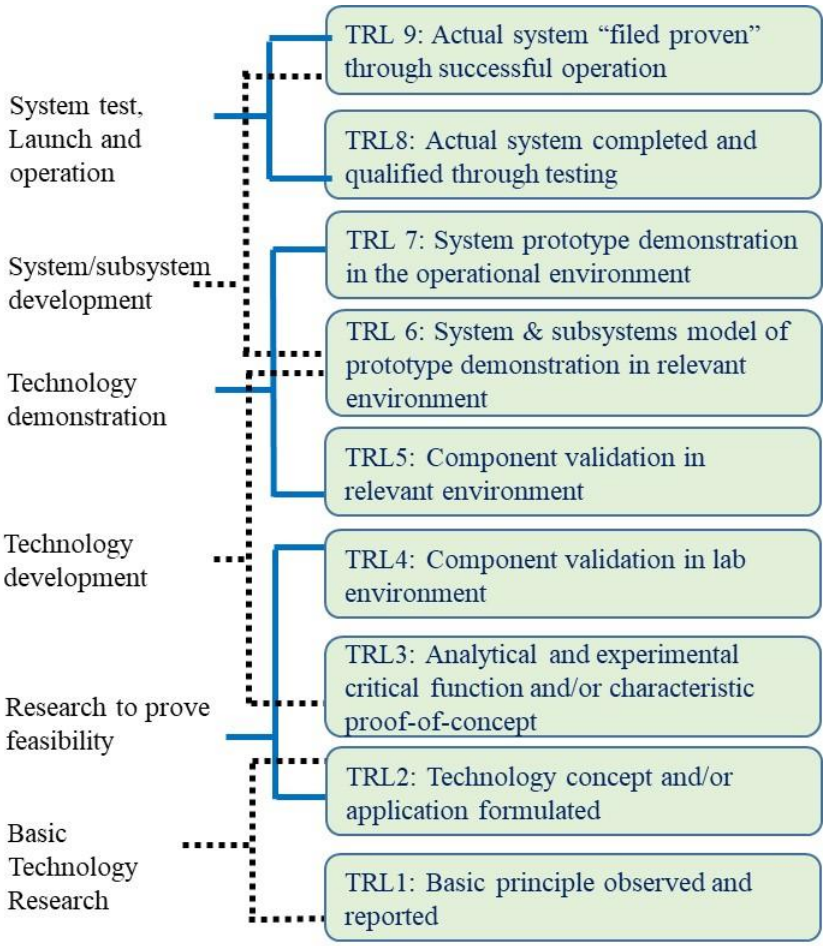

Figure 1: A generic NASA-type [32] TRL scale

Table 1: API definition of TRLs and its equivalence with the NASA type [33] definition

	API 17N's TRL	API 17N's TRL	Development Stage Completed	Definition of the development stage	NASA Like TRL
Concept	initiation	0	Unproven Concept (Basic R&D, paper concept)	Basic scientific/engineering principles observed and reported; paper concept; no analysis or testing completed no design history.	1
{roof-of-concept	Concept	1	Proven Concept (As a paper study or R&D experiments)	a) Technology concept and/or application formulated b) Concept and functionality proven by analysis or reference to features common with/to existing technology c) No design history; essentially a paper study not involving physical models but may include R&D experimentation	2
	Proof-of-concept	2	Validated Concept (experimental proof of concept using physical model tests)	Concept design or novel features of the design is validated by a physical model, a system mock-up or dummy and functionally tested in a laboratory environment; no design history; no environmental tests; materials testing and reliability testing is performed on key parts or components in a testing laboratory prior to prototype construction	3
Prototype	Integration	3	Prototype Tested (System function, performance and reliability tested	a) Item prototype is built and put through (generic) functional and performance tests; reliability tests are performed including reliability growth tests, accelerated life tests and robust design development test program in relevant laboratory testing environments; tests are carried out without integration into a broader system b) The extent to which application requirements are met are assessed and the potential benefits and risks are demonstrated	4
	Demonstration	4	Environment Tested (Pre-production system environment tested)	Meets all Requirements of TRL 3; designed and built as production unit (or full scale prototype) and put through its qualification program in simulated environment (e.g. hyperbaric chamber to simulate pressure) or actual intended environment (e.g. subsea environment) but not installed or operating; reliability testing limited to demonstrating that prototype function and performance criteria can be met in the intended operating condition and external environment	5
	commissioning	5	System Tested (Production system interface tested	Meets all the requirements of TRL 4; designed and built as production unit (or full-scale prototype) and integrated into the intended operating system with a full interface and functional test but outside the intended field environment	6
Field qualified	Production	6	System Installed (Production system installed and tested)	Meets all the requirements of TRL 5; production unit (or full-scale prototype) built and integrated into the intended operating system; full interface and function test program performed in the intended (or closely simulated) environment and operated for less than three years; at TRL 6 new technology equipment might require additional support for the first 12 to 18 months	7
	Field proven	7	Field Proven (Production system has been field proven)	Production unit integrated into the intended operating system, installed and operating for more than three years with acceptable reliability, demonstrating a low risk of early life failures in the field	8 & 9

Achievement of API's TRL 4 [2] is one of several pieces of evidence that is used in the decision-making process in committing to the major capital investment [43]. Thus, the TRL 4 is critical for making the decision on whether to go forward with the investment. TRL 5 arguably is the most important stage (technically) during the subsea development process. At API's TRL 5 [2] stage readiness of all necessary components must be demonstrated; it also involves a demonstration that the components work together as a system. Thus, achieving a TRL of 5 is a prerequisite for the integration and installation of assemblies. Validation at this level must go beyond discrete component level, it must consider testing of the assembly of components (or subsystems); testing at the quayside, and possibly in shallow water (i.e. a relevant environment) and/or the operational environment.

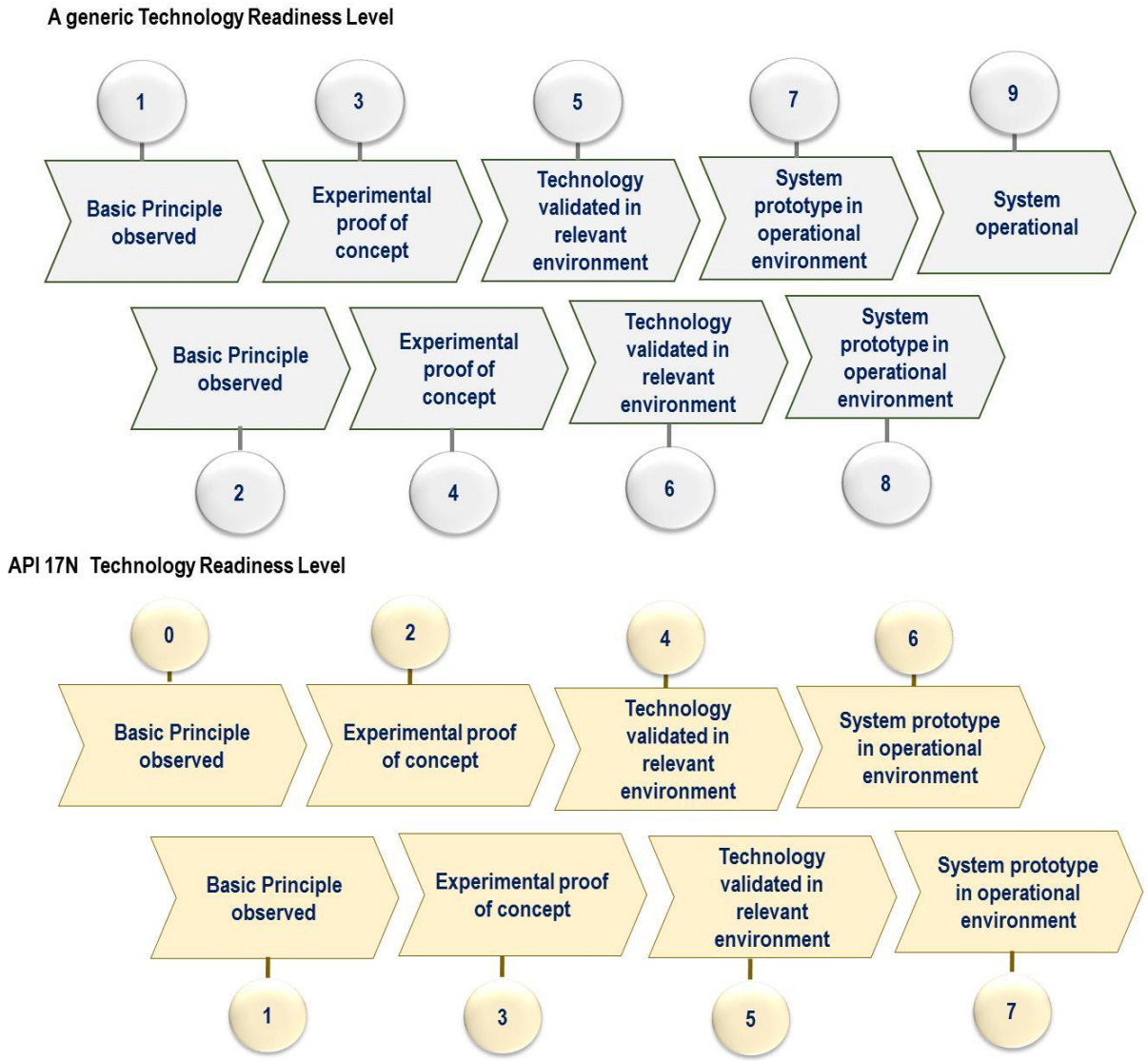

Figure 2: Comparison of NSA-type TRL scale with API's TRL scale

TRLs provide a common understanding of the status of a technology in its development pathway, a means of assessing and managing risk, and decision making concerning funding and implementation of technology. As with any management tool, there are certain limitations to its use. The TRL approach has been used in different industries and has proved to be useful as a tool for:

- general understanding of technology status;
- risk indicator and management;
- decision making with respect to technology funding;
- Decision making with respect to technology insertion.

Assigning a TRL rank is not a quick task. These are some questions that need to be answered and backed by evidence. In the subsea context:

- Is technology (equipment) widely used by other operators?
- Is technology demonstrated in the final form (in a system somewhere in the world)?
- Is technology demonstrated in the relevant environment (field conditions)?
- What is the target performance/efficiency level (technically and economically)?
- What is currently achieved performance/efficiency?
- What are the materials involved and what is their availability?
- Is infrastructure available for deployment for this technology?
- What are the main barriers impeding the higher performance? … etc.

2. Systems Engineering V-Model

TRL level is judged using the notion of Fit-For-Purpose (FFP), i.e. ready to use, supported by evidence gathered through analysis, simulation, experiment, standard testing and in-service experience. It is important to state both purpose and application; since mature irrelevant technology is as useless as immature relevant technology. Readiness only has a meaning in relation to the purpose of the product or service.

The systems engineering framework can help to document and track all requirements which are the system purposes. Systems Engineering is an integrative process of top-down synthesis, development, and operation of a real-world system that satisfies, in a near optimal manner, the full range of requirements for a system. [48 and 49]

The system engineering V-model describes the activities and results that must be produced during development (Figure 3). The left side of the V represents the system specification stream, where the system requirements and the system and subsystem or component designs are specified. The designed components are then fabricated and installed at the bottom of V. Component fabrication is followed by the testing stream on the right tail of the V, where the gradually evolving and growing system is verified against specifications defined on the right-hand side of the V.

The system is specified top-down and then the subsystems are integrated bottom up. Additionally, the definition of distinct steps for the design, at different hierarchy levels, appears first in the V-model and enables breaking down of the system into independent subsystems. The system is decomposed (broken down) into functional subsystems, which are easier to handle. Subsystems can then be designed and fabricated in parallel, according to the system specifications defined in the previous phase.

Technology readiness only has a meaning in relation to the purpose of the system that will be using it. If something does the job for which it is designed then it is ready for insertion.

Describing the purpose of a system, one needs to look beyond the system itself, and into the activities that it will support. For example, the purpose of a banking system is not to be found in the technology used to build it, but in its day-to-day business activities in fulfilling the needs of its customers. Thus, requirements are a set of activities concerned with identifying and communicating the purpose of a system and the contexts in which it will be used. Requirements act as a bridge between the real-world needs of the Client, and the capabilities and opportunities afforded by technologies. Then the technology is assessed if it would support the requirements.

Requirements analysis provides a process for understanding the purpose of a system and the contexts in which it will be used. It bridges the gap between, an initial vague recognition that there is a need, and the task of building a system to address such a need. Ideally, each requirement from the highest to the lowest level of the project must link to a parent requirement. Requirements without parents will either represent a nice to have or a missing requirement at the higher level. If it is the former, the existence of the requirement must be carefully considered again. In the event of the latter, the requirement needs to be rolled back up to ensure completeness of the requirements at the higher level. A simple trace matrix can be used to simplify and provide a clearer arrangement of the traceability and is needed to ensure that all higher-level requirements are linked to the lower level requirements, and will be maintained throughout the system development. This is one of several parameters which influences the TRL decision.

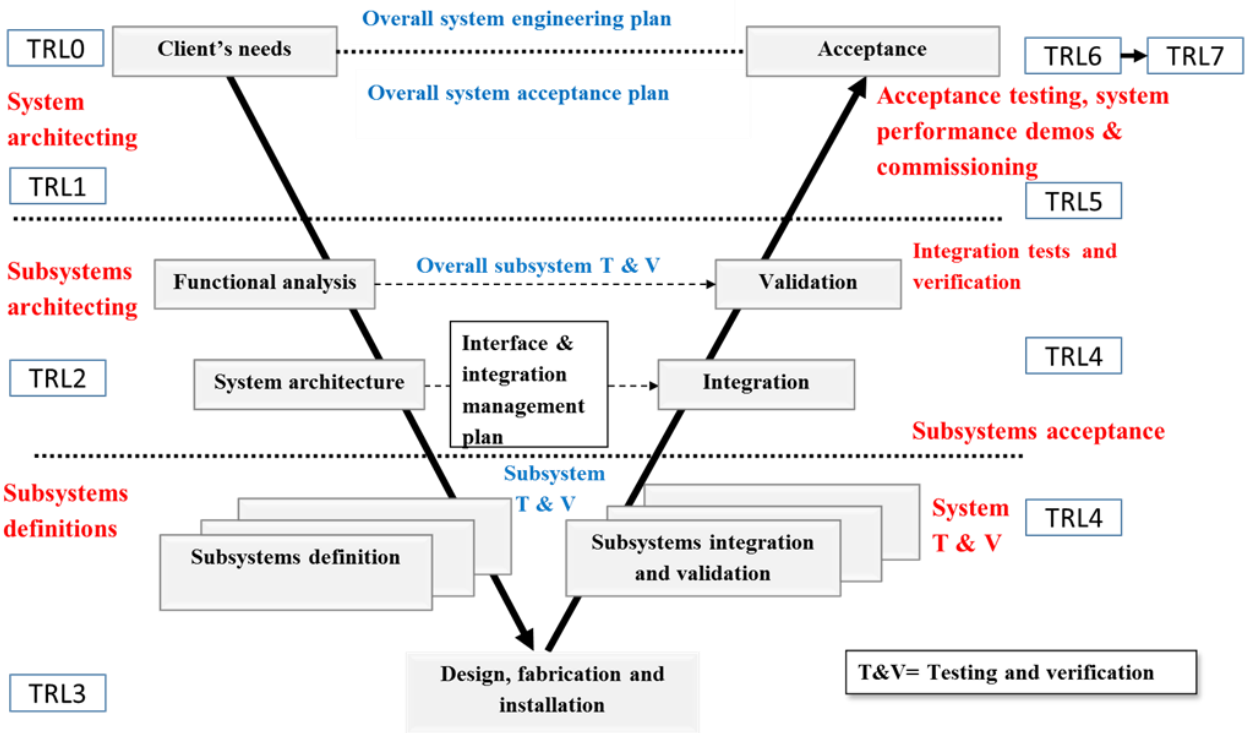

Figure 3: Systems engineering V-model for product development.

The traceability requirement ensures that all a system's needs can be traced to one or more piece of equipment, as well as all equipment can be traced to a requirement. Thus the traceability references the link between user requirements, specifications and test cases. This makes it possible to trace cross-references between specified elements.

3. Integration Readiness Level (IRL)

The TRL scale is component oriented. Namely, the focus of TRL is on individual technologies (components) in isolation, as the primary use of the TRL scale is to align different technological developments and move them along the same timeline. However, the higher TRLs (e.g. API's TRL 6: installation completed and the system being qualified i.e. validated), are about integrating different individual technologies, possibly with different maturities, into a complex system. Acceptable technology maturity has often been the principal driver, particularly in systems where availability is fundamental to the customer requirements. While TRL provides a metric for describing components' maturity status, one should still be interested in a metric that provides a description of integration, i.e. how components relate to each other. It is vital that all stakeholders have the same understanding when evaluating the integration maturity, which also can be used together with TRL to potentially determine the system readiness.

Many authors extended the TRL classifications to account for the effects of having to integrate multiple technologies to create a single system; see e.g. Sauser et al [34] and Yasseri [43]. They introduced another metric called Integrated Readiness Level (IRL) to compliment the TRL metric for the integration of applications. They also developed a protocol to measure the overall technological readiness of a system, System Readiness Level (SRL), by combing the TRL and IRL metrics of all technologies included in the system to produce an index to measure the complete system readiness. Yasseri [43 and 47] created an Integration Readiness Level (IRL) for subsea systems to measure integration maturity on a scale similar to API's TRL [2] with the objective that it could be combined with TRL to provide a system-level readiness. Assessment of the readiness of the individual technologies will contribute to risk reduction in budgets and planning. Other readiness assessment metrics have been developed to compliment TRL, see for example London et al [22] and McConkie [27]

Further clarification of the eight levels of IRL (including zero) is presented in Figure4. From Table 2 can be understood as having three stages of integration definition: semantic, syntactic, and pragmatic. Semantics is about relating meaning with respects to clarity and differentiation. Thus IRL 0-2

Table 2: Definitions of TRL, IRL and SRL

Phase	TRL	Development stage	IRL	Development stage	SRL	Development stage
System validation	7	Proven in the filed - Production system field-proven.	7	Integration is field-proven through successful operations.	7	Field Proven Operational System.
	6	System installed - Production system Installed and tested.	6	Integration is completed and qualified through sufficient and rigorous testing in the marine environment.	6	The System is installed tested. Commissioning in progress.
Technology validation	5	System tested - Production system interface tested.	5	The integration has been verified and validated with sufficient detail for the system to be deployable.	5	Manufacturing and installation in progress.
	4	Environment tested - Preproduction system environment tested.	4	There are sufficient details to assure interoperability between technologies necessary to establish, manage and assure the integration.	4	Detail design and final procurement.
	3	Prototype tested - System function, performance, and reliability tested.	3	There is sufficient detail in the control and assurance of the integration between technologies to deliver the required functionality.	3	Front-end engineering, sourcing of long lead items.
Concept validation	2	Validated concept - Experimental proof of concept using physical model tests.	2	There is sufficient evidence of compatibility between technologies within the system. Namely, they will work together and can be integrated with ease.	2	Concept Selection. An optimal concept has emerged.
	1	Demonstrated concept - Proof of concept as desk study or R&D experimentation.	1	There is some level of specificity to the system functionality to allow identification of linkage between technologies.		Concept Refinement. Two or more competing concept being considered.
	0	Unproven concept - Basic research and development (R&D) in papers.	0	The interface, i.e. the linkage, between technologies can be identified/characterised with sufficient clarity.	0	Concept Definition. Various ideas are being considered or discounted

are considered fundamental to describing what we define as the three principles of integration: i.e. interface, interaction, and compatibility. It can be contended that these three principles are fundamental to an integration effort. The next stage is Syntactic, which is defined as a conformance to rules, where IRLs 3-5 are about the assurance that an integration effort is in compliance with specifications. The final stage is Pragmatic, which relates to practical considerations. Thus, IRLs 6-7 are about the assertion of the application of an integration effort.

4. Systems readiness level

The application of an IRL in the assessment process provides a check as to where the technology maturity is on an integration readiness scale. Just as a TRL has been used to assess the risk associated with developing technologies, an IRL is designed to assess the risks associated with integrating these technologies. Table 2 defines an SRL scale that incorporates the maturity level of components and the interoperability of the entire subsea system, including integration with its environment.

Sauser et al [34] combined the TRLs and IRLs for a system under development, using a matrix multiplication. Yasseri [43] proposed a methodology to aggregate TRL and IRL into a single metric, termed SRL_{est}. This methodology requires all components to be assessed using TRL (Table 2), as well as their readiness for integration with each other and the environment to be assessed using IRL (Table 2). For more detail see [43]. The proposed method combines TRLs and IRLs into a single composite metric, yielding a numerical value between 0 and 7. The estimated SRL_{est} is used in Table 2 to judge system readiness, compared with what it should be at the time of assessment. Building a spreadsheet (see the case example) will enable the user to regularly review the state of system readiness and track the project's progress.

5. Domain Mapping

A system is described as an aggregation of equipment and enabling products to achieve a given purpose. In the context of an oil and gas production system, these are the subsystems and facilities that together achieve the mission. A system can be mapped in different ways depending on the overall goal. It may show a system as a single facility or several facilities linked together. It is this diagram that provides a visual tool for applying TRL. Thus, it is necessary to construct a system map to determine the overall purpose and identify all equipment in a facility that is required to create a complete production system. A system map shows every piece of equipment that is required, and how they are linked together. There are several ways to map a system. For example, a schematic diagram of a chemical process uses symbols to represent the vessels, piping, valves, pumps, and other equipment of the system, emphasizing their interconnection paths while omitting all physical details. In an electronic circuit diagram, the layout of the symbols may not resemble the layout in the circuit. The schematic (see below) shows the intent and how the parts are supposed to interact with each other. Thus, a schematic, or schematic diagram, is a representation of the elements of a system using abstract graphic symbols rather than realistic pictures. A schematic usually omits all details that are not relevant to the information. In contrast, a construction drawing shows things as they are actually laid out, and shows them to scale. A construction drawing can be used to build the system.

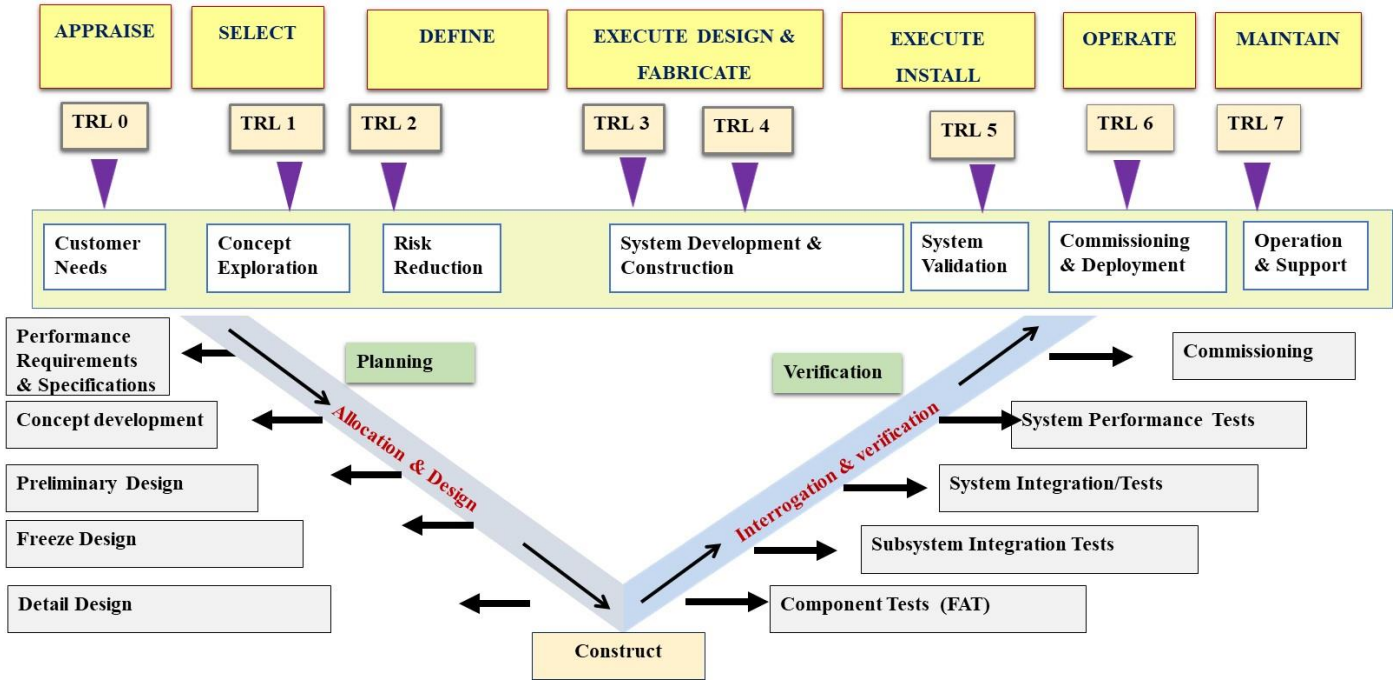

Figure 4: Timeline for stage-gating in a subsea development

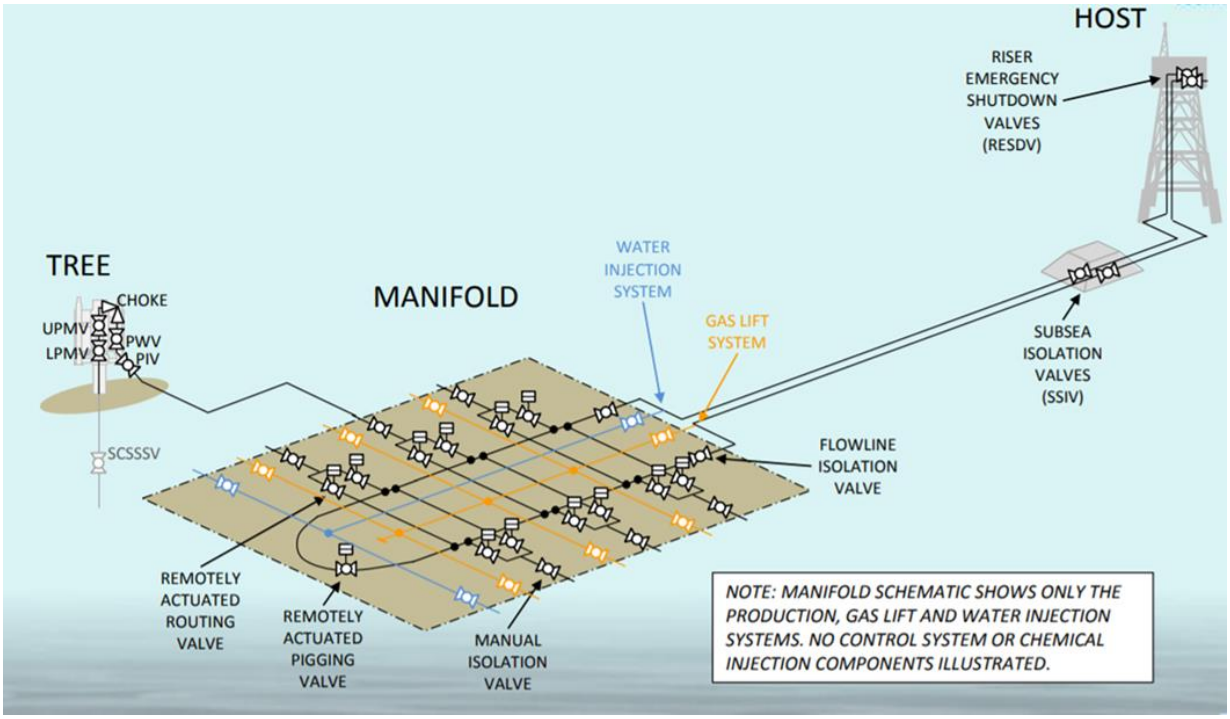

Figure 5: A schematic of a subsea production system

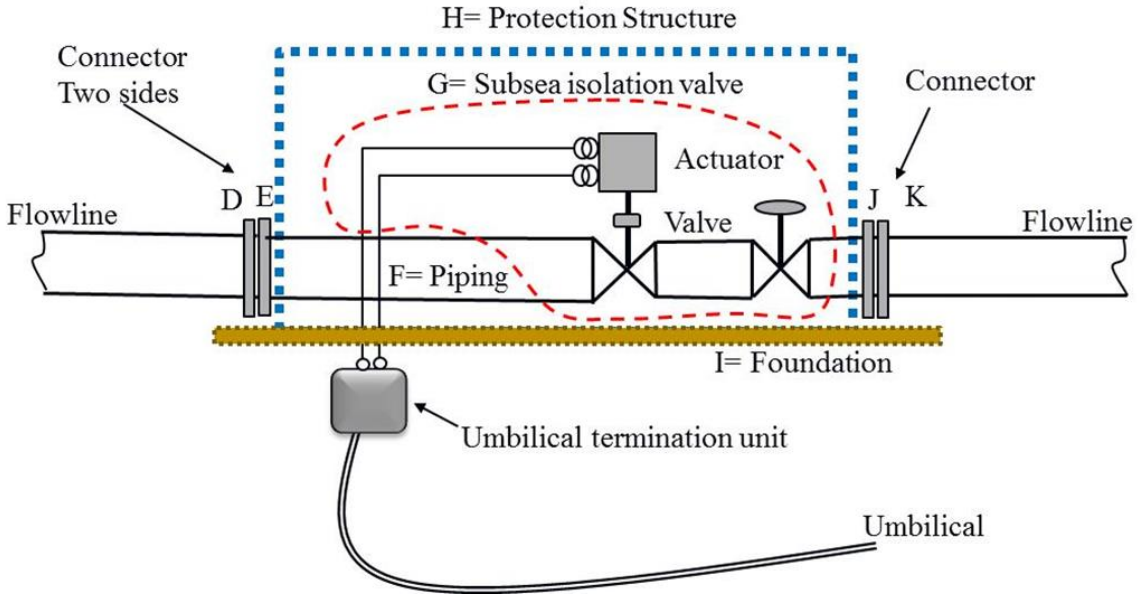

Figure 6: A detailed schematic of the SSIV used in the SPS system shown in Figure 5above.

Figure 5 shows a schematic of a simple subsea production system. A schematic of the subsea isolation valve (SSIV) shown in Figure 5 is shown in more detail in Figure 6. SSIV components have been labelled for later use in this paper.

Two popular methods of representation of a system functional architecture (or alternatively its structural elements) are the Block Diagram (BD) and the Design Structure Matrix (DSM) as further described below.

Block Diagram: A method to avoid unnecessary clutter is the Block Diagram. A Block Diagram is a representation of a system in which the principal or functions (or parts, or equipment) are represented by blocks connected by lines that show the relationships between the blocks. They are used in various engineering disciplines e.g. in reliability analysis, and process flow diagrams. A Block Diagram will not show every detail. Block Diagrams are typically used for higher level, less detailed descriptions that are intended to demonstrate overall concepts without concern for the details of implementation. As such, they provide a quick, high-level view of a system to rapidly identify points of interest or trouble spots. The Block Diagram is especially focused on the input and output of a system. It cares less about the internal workings. This principle is referred to as the Black Box in engineering, whereby the parts that get from input to output are unknown, or they can be left for a later in-depth study.

Figure7 shows the Block Diagram of a simple system consisting of 7 components grouped into 2 modules at an advanced stage of the development. There are interfaces between the components of each module, as well as between components of the two modules. Interfaces between the two components are shown by double-headed arrows, which implies, that the readiness of two components to be integrated is interdependent. The arrow is not intended to indicate the direction of the flow, but to show dependency or relationship. This is a simple representation of a system architecture, which captures the relationship between different components.

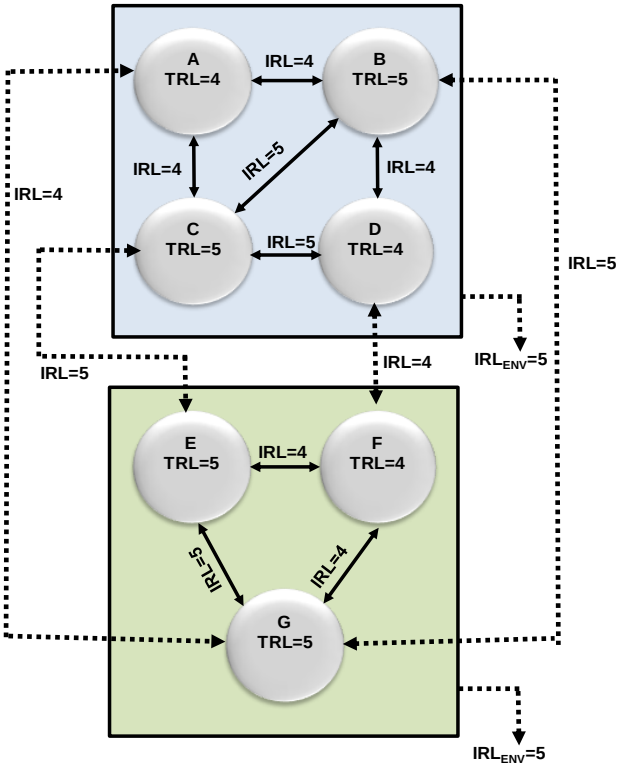

Figure 7: A system consisting of two modules

Design Structure Matrix: DSM is a visual tool [11] that represents the relationships and dependencies between components of a system. The component-based DSM (Eppinger and Browning, [14]), which is used in this paper, comprises of a list of components in some desirable order whereby upstream components are listed in the upper row. DSM is a square matrix for a visual representation of a system ([42], [9] and [10]), which shows both components of the system and linkages between them. It is the equivalent of an adjacency matrix in graph theory and is used in systems engineering and project management to model the structure of complex systems, in order to perform system analysis, project planning and organizational design. The system elements are often labelled and are shown in a row of the matrix and in a column on the left of the matrix. These elements represent subsystem, components (in a component-based DSM), or project activities (in an activity-based DSM).

Figure 8 shows a directed graph network and its representation using DSM is shown in Table 3. Figure 8 depicts the functional block diagram which gives a view of the functional elements, and how they must interface to achieve the overall goal (relationships). The components are shown as rows and columns in the matrix (Table 3) where they are listed in the same order along both axes. An off-diagonal mark located within the matrix denotes a coupling between two components (relationship). Table 3 shows that components C and H do not require input from the other components, but A, B, D, E, F, and G do receive inputs. The component interactions are represented by "***X***" marks in the off-diagonal cells. The marked cells indicate dependencies between components. Reading down a column indicates that a component provides input to others in its associated row. On the other hand, a component in the row receives input from the component in the corresponding column when reading across a row in the matrix. A number can be used instead of "***X***" to represent some sort of quantity, for example, risk or/and the volatility of the interface (see [44]).

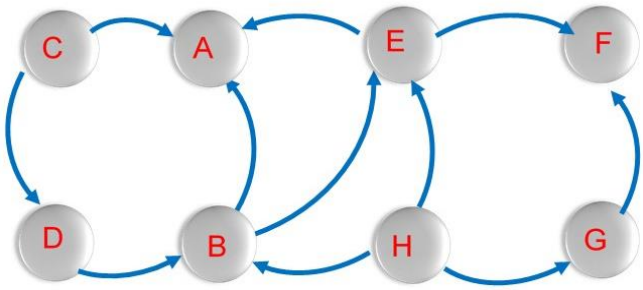

Figure 8: A directed graph network showing component of a system and their connectivity

Table 3: DSM of the directed graph network shown in Figure 7. Reading along a row reveals the input/dependency which is marked by an X placed at the intersection of that row with the column that bears the name of the component providing input.

	A	B	C	D	E	F	G	H
A	**A**	**X**	**X**		**X**			
B		**B**		**X**				**X**
C			**C**					
D			**X**	**D**				
E		**X**			**E**			**X**
F					**X**	**F**	**X**	
G							**G**	**X**
H								**H**

Since the network shown in Figure 7 is a directed graph, its DSM shown in Table 3 is an asymmetrical matrix. This paper, for simplicity, assumes at the highest level of system hierarchy all dependencies are a two-way relationship; thus, leading to a symmetrical matrix. The relationship maps show that element D is dependent on C through some characteristic of D. In doing this, the analyst should understand better the

complexity of a system and, in turn, has more information to manage dependencies and use this information to improve system performance and manage interfaces between the elements [14].
As another example, the Block Diagram of Figure 6 is mapped into the Design Structure Matrix (DSM) as shown in Table 4. Here it is assumed that dependency is bilateral, thus the DSM is a symmetric matrix. The DSM maps the elements of a system to each other (like a two-way table), enabling concise representation and integration analysis. Reading across a row of the matrix shows where the element in that row sends its outputs and reading down a column shows where the element in that column receives its inputs [9].

Table 4: DSM representation of the subsea isolation valve shown in Figure 5. Note the symmetric matrix due to the assumption of two-way mutual dependency.

Components		D	E	F	G	H	I	J	K
Connectors (female)	D	D	*X*						
Connectors (male)	E	*X*	E	*X*					
Piping	F		*X*	F	X	*X*		*X*	
SSIV	G			*X*	G				
SSIV Structure	H			X		H	*X*		
SSIV Foundation	I					X	I		
Connectors (female)	J			*X*				J	*X*
Connectors (male)	K							*X*	K

The X marks in Table 4 indicate the existence and direction of information flow or a dependency of one component with another. Reading along a row reveals the input/dependency flows by an X mark placed at the intersection of that row with the column that bears the name of the input task. Reading down a column reveals the output information flows from that component to another component by placing an X in a similar manner as described above. For example in the DSM (Table 4), the marking in row E and column D indicates a dependency between E and D (E must integrate with D). The cells on the diagonal are typically used to represent the system elements and their interface requirements. Marks below the diagonal represent forward flow of information, and marks above the diagonal represent feedback from a later downstream task to an earlier or upstream one. This means that the earlier task has to be repeated in light of the late arrival of new information, thus making the processes iterative. Design iterations create rework and require extra communications and negotiation.
Matrix-based tools provide some insight into the internal relationship of a complex system (i.e. a dependency map and their complexity); however, they do not expose the logic behind these dependencies. That is, if component A is shown to relate to component E, it is not clear why and how this relationship exists and where it originates from. Such information can be represented on Block Diagrams.

Table 5: DSM for the system shown in Figure 7. Components A to J are mapped along the diagonal and off-diagonal numbers are the IRL values.

	TRL		A	B	C	D	E	F	G	ENV
M1	4	A	A	4	4				4	
	5	B	4	B	5	4			5	
	5	C	4	5	C	5	5			
	4	D		4	5	D		4		4
M2	5	E			5		E	4	5	
	4	F				4	4	F	4	
	5	G	4	5			5	4	G	4
ENV										

As another example, the Block Diagram of Figure 7 is mapped into a DSM matrix (Table 5). The TRL of each component is shown in the column to the left of the components. Numbers in off-diagonal terms are the IRL of this system which consists of only two modules. The decision regarding the level of detail required for a system map will be dependent on the technologies being developed. In many cases a tiered approach will be required, starting with a super-system diagram and then a system diagram for individual plants or facilities; possibly linked together. In some cases, (e.g. for complex, highly integrated equipment), sub-system diagrams may be required to highlight aspects of a piece of equipment within an assembly of the system that requires development. Generally presenting every component of a system in a single matrix obscures its visual usefulness. A subsea system can be organised into a hierarchical structure, e.g. subsystem, sub-subsystems and assemblies or components ([44]). Such hierarchical representation avoids problems related to presenting extremely large matrices by shifting the focus to various levels in the hierarchy at a time, which enables the analysis of a system at different levels of details as necessary. In general, the DSM analysis only looks at relationships across components (at the same level) and not within components (which is the next level below).

5. Example Case

A system is a collection of equipment and enabling software linked together to achieve a given goal. Figure 9 shows an example system consisting of three subsystems (or modules) linked together. Within each subsystem, there are a number of components or items and it is to them that the TRLs are applied.
A process which is known as Technology Readiness Assessment (TRA) is used to identify Critical Technological Elements (CTEs) of a system. The TRA is a systematic, evidence-based process [46] that assesses the maturity of CTEs. A technological element is "critical" if the system depends on it to meet

operational requirements. Thus, if a system depends on specific technologies to meet operational threshold requirements in development, production, and operation, and if the technology is new, that technology is deemed to be Critical Technological Element (CTE). Not every component is subjected to a rigorous TRA assessment.

One should make a distinction between critical technology and necessary technology. In principle, every equipment in a system is necessary since if there is no need for an equipment, it can be eliminated. However, only a few pieces of equipment may be critical, since there is no substitute for them, and without them, the intended system will not perform. In subsea practice, no subsystem, assemblies (or large components) are excluded from the assessment; namely, every equipment is considered to be critical. The level of detail is decided by the assessor(s), drawing help from the subject expert. This suggests that the purpose of TRL in the subsea industry is to ensure the readiness of the components for insertion into the system.

Table 6 shows a DSM for the case example of Figure 9. Simplifications can be made to prevent DSM clutter. In practical cases, this matrix can be much larger. However, one should only include important items and avoid unnecessary complications, since including every nut and bolt would not lead to a better conclusion. Once the system's DSM (Table 6) is complete, TRLs for each item can be assigned by following the description in Table 1.

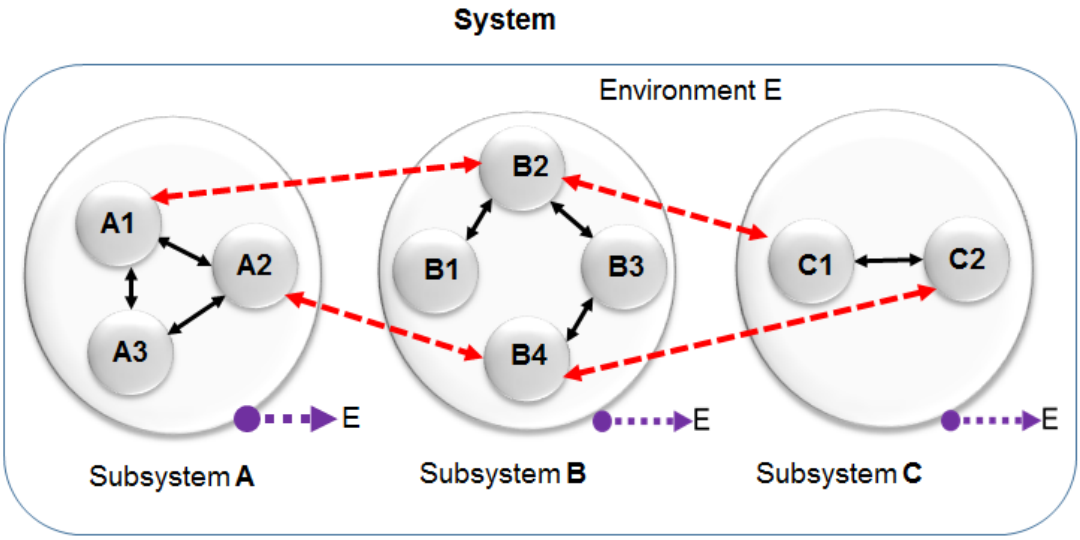

Figure 9: System architecture of the case example.

Table 6: A DSM of case example shown in Figure 9.

1	2	3	4	5	6	7	8	9	10	11	12	13	14	15	16	17
2			Components													
3			A1	A2	A3	B1	B2	B3	B4	C1	C2	ENV				
4		TRL	**IRL Matrix**										Ave. IRL	TRL*Ave_IRL	SQRT	Module IRL
5	A1	5		**4**	**5**		**5**						4.67	23.33	4.83	
6	A2	4	**4**		**4**				**4**				4.00	16.00	4.00	
7	A3	4	**5**	**4**		**4**						4	4.33	17.33	4.16	4.35
8	B1	5			**4**		**4**						4.00	20.00	4.47	
9	B2	5	**5**			**4**		**4**		**5**			4.50	22.50	4.74	4.39
10	B3	4					**5**		**4**		**4**		4.33	17.33	4.16	
11	B4	4		**4**				**4**			**5**	4	4.33	17.33	4.16	
12	C1	5					**5**				**5**		5.00	25.00	5.00	
13	C2	5						**4**	**5**	**5**		4	4.67	23.33	4.83	4.92
14															SRL=	3.44

For this example, it is assumed that two interfacing components could be at a different TRL, but their integration readiness levels are the same and equal to the least ready component, (due to mutual dependency), hence yielding a symmetric matrix. In general, if two components are combined to create an assembly, there may be different degrees of integration readiness for each component and hence the matrix may not be symmetric in some cases. Symmetry assumption is not necessary for the application of the method.

Each row of the column "*Average_IRL*" in Table 6 is the arithmetic mean of all IRLs in that Row, determined by summing up of IRLs of all interfaces

across the row and dividing it by the number of interfaces; e.g. for the first row $(4 + 5 + 5)/3 = 4.67$. The 15th column gives the results of multiplication of the component's TRL by the average of its IRLs; e.g., in Row 1:- $5 \times 4.67 = 23.33$. The 16th column gives the sure root of the 15th Column, which is SRL of each component. In statistics and its applications, the **root-mean-square** (abbreviated **RMS** or **rms**) is defined as the square root of the mean square (the arithmetic mean of the squares of a set of numbers). The RMS of the 16th column is given in Column 17, which is the SRL for each module, giving a composite *module* readiness index. For the first sub-system [43]:

$$M_{1-R} = \sqrt{\frac{23.33 + 16.00 + 17.33}{3}} = 4.35$$

Three in the denominator is the number of components of the first subsystem. Alternatively,

$$\mathrm{M_{1-R}} = \sqrt{\frac{(4.83)^2 + (4.00)^2 + (4.16)^2}{3}} = 4.35$$

An estimate of the system readiness level is given by [43]

$$\mathrm{SRL_{estimate}} = \sqrt{\frac{4 \times (4.83)^2 + 4 \times (4.00)^2 + 4 \times (4.16)^2}{7 \times 3}} = 3.44$$

Where, 7 is the highest score in API's TRL ranking [2] and it is used for normalisation purpose.

From a metric point of view both $\mathrm{SRL_{est}}$ and SRL are meant to measure the same things on the same scale. However, SRL is defined (Table 3), while $\mathrm{SRL_{est}}$ is derived by aggregation of attributes of all components. The estimate of system readiness reaches its highest level from below, as it measures the system readiness as a whole, not its elements. If all components mature simultaneously along the same path, then $\mathrm{SRL_{est}}$ reaches SRL.

Using a value of 3.44 in Table 1, the system must be at assembly and installation stage, if the project schedule dictates a different level then reasons must be sought. One should distinguish between component readiness level and the system readiness level. For instance, a component is investigated if it had achieved TRL 6. Although this investigation is in the context of the intended system in its environment, the focus is on that individual component, not the whole system.

This index informs the management when and where to intervene if the system readiness is lagging behind the schedules. The entries in each row identify which components require more management attention. A tightly controlled project ensures that TRL, IRL and SRL closely follow each other.

6. Concluding Remarks

In a previous paper by the lead author [43] two new metrics where defined to complement API's TRL scale, I.e. IRL and SRL. The Integration Readiness Level (IRL) indicates the readiness of two interfacing components to be brought together. The System Readiness Level (SRL) is a measure of the readiness of the entire system, which combines Technology Readiness Level (TRL) with IRL quantitatively into a system readiness metric. The methodology is further extended by adding a system engineering framework around the process to track the progress of a subsea system development. The process of estimating SRL is described using a case study, which is a simplified version of the development of an actual subsea subsystem.

Comparing the estimated SRL and values in the SRL table given in this paper would indicate the level of system readiness. These three indices can provide part of the required information for the sanction bodies to allow a project to move through the review gate to the next phase of development, in a stage-gate process [44]. Technology development, Integration and Systems development follow similar evolution (or maturation) paths, TRL, IRL and SRL are not generally far apart, allowing performing arithmetic on the ordinal numbers [47]. This paper distinguishes readiness from maturity. If a technology is used in another system then it is matured, but it is considered not ready for the system under development until proven so. Thus, an existing mature theology enters into a new system at TRL 5 or 6 at best.

The proposed System Readiness Assessment methodology provides decision-makers with a snapshot of a system's holistic state of readiness, and quantifies the level of component-to-component integration during the system development, helping to improve design, fabrication and installation management. Implementation of the SRA methodology aids decision makers in identifying both programmatic and technical risk areas.

8. REFERENCES

1. ABS, (2017). Guidance notes on Qualifying New Technologies, American Bureau of Shipping, PP 45
2. API Recommended Practice 17N (2009), Recommended Practice for Subsea Production System Reliability and Technical Risk Management.
3. Austin, M. F., & York, D. M. (2015). System Readiness Assessment (SRA) an Illustrative Example. Procedia Computer Science, 44, 486–496. https://doi.org/10.1016/j.procs.2015.03.031
4. Azizian, N. Sakami, sh. and Mazzuchi.T. (2009). "A Comprehensive Review and Analysis of Maturity Assessment Approaches for Improved Decision Support to Achieve Efficient Defense Acquisition, Proceedings of the World Congress on Engineering and Computer Science 2009 Vol II WCECS 2009, October

20-22, 2009, San Francisco, USA, http://www.iaeng.org/publication/WCECS2009/WCECS2009_pp1150-1157.pdf
5. Azizian, N., Mazzuchi, T., Sakami, Sh. and David F. Rico D. (2011). A Framework for Evaluating Technology Readiness, System Quality, and Program Performance of U.S. DoD Acquisitions, Systems Engineering Vol.14, no. 4: 410-26.
6. Bakke, Kjersti (2017), Technology readiness levels use and understanding, Master thesis, University College South-East Norway, last accessed 31/05/2018 https://brage.bibsys.no/xmlui/handle/11250/2452831
7. Bilbro J.W. (2007). A Suite of Tools for Technology Assessment. In Technology Maturity Conference: Multi-Dimensional Assessment of Technology Maturity. Virginia Beach, VA: AFRL. http://www.dtic.mil/cgi-bin/GetTRDoc?AD=ADA507181.
8. Bissell C. and Chapman D. (1992). Digital Signal Transmission. Cambridge University Press. UK
9. Browning, T. (2001). Applying the Design Structure Matrix to System Decomposition and Integration Problems: A Review and New Directions, IEEE Transactions on Engineering Management. 48(3):292-306, 200.
10. Browning, T. (2002). Modelling Impacts of Process Architecture on Cost and Schedule Risk in Product Development, IEEE Transactions on Engineering Management. 49(4), pp 428-442.
11. Browning, T.R. (2016). Design structure matrix extensions and innovations: a survey and new opportunities, IEEE TRANSACTIONS ON ENGINEERING MANAGEMENT, VOL. 63, NO. 1, February 2016.
12. DNV-RP-A203 (2011). Qualification of new technology. Det Norske Veritas, Høvik, Norway.
13. Dowling, T. and Pardoe T. (2005). TIMPA - Technology Insertion Metrics, Volume 1, Ministry of Defence, United Kingdom, QinetiQ.
14. Eppinger, S.D. and Browning, T.R. (2012). Design Structure Matrix Methods and Applications (Engineering Systems), MIT Press, 19-Jun-2012, 280 pages. ISBN-10: 0262017520DoD, Director, Research and Engineering (DDR&E), "Technology Readiness Assessment (TRA) Deskbook", July 2009, Appendix F.
15. Gove, R. (2007). Development of an Integration Ontology for Systems Operational Effectiveness, Department of Systems Engineering and Engineering Management, Stevens Institute of Technology, Hoboken.
16. Gove, R., B. Sauser, and J. Ramirez-Marquez. (2007). Integration Maturity Metrics: Development of an Integration Readiness Level. In Stevens Institute of Technology, School of Systems and Enterprises Hoboken, NJ: SSE_S&EM_004_2007.
17. Homeland Security Institute, (2009), "Department of Homeland Security Science and Technology Readiness Level Calculator (ver 1.1) Final Report and User's Manual," Jesus, G.T. and Chagas, M.F. (2018). Integration Readiness levels Evaluation and Systems Architecture: A Literature Review, International Journal of Advanced Engineering Research and Science (IJAERS), Vol-5, Issue-4, pp73-84.
18. Kujawski, E. (2010). The trouble with the System Readiness Level (SRL) index for managing the acquisition of defense systems National Defense Industrial Association 13th Annual Systems Engineering Conference October 25-28, 2010, San Diego.
19. Katz, D.R., Sakami, S., Mazzuchi, T., and Conrow, E.H., (2015), "The Relationship of Technology and Design Maturity to DoD Weapon System Cost Change and Schedule Change During Engineering and Manufacturing Development," Syst. Eng., vol. 18, no. 1, pp. 1–15.
20. Institute of Electrical and Electronics Engineers - IEEE, International Electrotechnical Commission - IEC, & International Organization for Standardization - ISO. (2007). ISO/IEC 26702-2007 IEEE 1220-2005 Standard for Systems Engineering - Application and Management of the Systems Engineering Process. Geneva, Switzerland: ISO/IEC/IEEE. https://doi.org/10.1109/IEEESTD.2007.386502
21. ISO 16290:2013, (2013). Preview Space systems -- Definition of the Technology Readiness Levels (TRLs) and their criteria of assessment. Pp 12.
22. London, M. A., Holzer, T. H., Eveleigh, T. J., & Sakami, S. (2014). Incidence matrix approach forcalculating readiness levels. Journal of SystemsScience and Systems Engineering, 23(4), 377–403.https://doi.org/10.1007/s11518-014-5255-8
23. Lord, F.M. (1953). on the statistical treatment of football numbers, 1953, American Psychologist, 8, 750-751,http://www.stat.wharton.upenn.edu/~hwainer/Readings/Frederick%20Lord_On%20the%20statistical%20treatment%20of%20football%20numbers.pdf
24. Mankins, J. C. (1995). Technology Readiness Levels. Washington, USA, https://doi.org/10.1080/08956308.2010.11657640
25. Mankins, J. C. (2009). Technology readiness assessments: A retrospective. Acta Astronautica, 65(9–10), 1216–1223. https://doi.org/10.1016/j.actaastro.2009.03.058
26. Mankins, J. C. 2002. Approaches to Strategic Research and Technology (R&T) Analysis and Road Mapping. Acta Astronautica 51 (1-9): pp. 3
27. McConkie, E., Mazzuchi, T., Sakami, S., Marchette, D. (2013). Mathematical properties of System Readiness Levels. Systems Engineering, v 16, n 4, p 391-400.
28. MoD. UK Ministry of Defence, (2008) "System Readiness Levels (SRLs)", AOF Technology Management Policy, Information and Guidance on the

Technology Management aspects of Defence Acquisition version 1.0.1, available at: http://www.aof.mod.uk/aofcontent/tactical/techman/content/srl_whatarethey. Last accessed 10/10/2012.
29. MoD. UK Ministry of Defence, (2011). Defence Technology Strategy for the Demands of the 21st Century, http://www.mod.uk/nr/rdonlyres/27787990-42bd-4883-95c0-b48bb72bc982/0/dts_complete.pdf. Last accessed 12/10/2012.
30. NASA, (2007), NASA Systems Engineering Handbook, Washington, D.C.
31. The NASA technology push towards future space mission systems. Acta Astronautica, 20, 73–77. https://doi.org/10.1016/0094-5765(89)90054-4
32. Nolte, W. L., Kennedy, B. M., & Dziegiel, R. J. J. (2003). Technology Readiness Level Calculator. White Paper: Air Force Research Laboratory, 2004.http://www.dtic.mil/ndia/2003systems/nolte2.pdf
33. Olechowski, A. L., Eppinger, S. D., & Joglekar, N. (2015). Technology readiness levels at 40: A study of state-of-the-art use, challenges, and opportunities. In Portland International Conference on Management of Engineering and Technology (PICMET). Portland, USA: IEEE. https://doi.org/10.1109/PICMET.2015.7273196
34. Sauser, B., J. Ramirez-Marquez, D. Henry, D. Dimarzio, and J. Rosen. 2007. Methods for Estimating System Readiness Levels. The School of Systems and Enterprises White Paper. Hoboken NJ: Stevens Institute of Technology.
35. Sauser, B., J. Ramirez-Marquez, R. Magnaye, and W. Tan. 2008. System Maturity Indices for Decision Support in the Defense Acquisition Process. In 5th Annual Acquisition Symposium. Monterey, CA.
36. Sauser, B., D. Verma, and J. Ramirez-Marquez. (2006). From TRL to SRL: The Concept of Systems Readiness Levels. In Conference on Systems Engineering Research. Los Angeles, CA.
37. Sauser, Brian, Jose Ramirez-Marquez, D. Henry, and D. Dimarzio. (2008). A System Maturity Index for the Systems Engineering Life Cycle. International Journal of Industrial and Systems Engineering 3.
38. Sadin, S. R., Povinelli, F. P., & Rosen, R. (1989).
39. Smith, J. D. (2005). An Alternative to Technology Readiness Levels for Non-Developmental Item (NDI) Software. Proceedings of the 38th Annual Hawaii International Conference on System Sciences. https://www.computer.org/csdl/proceedings/hicss/2005/2268/09/22680315a.pdf
40. Stevens, S. S., (1946). On the Theory of Scales of Measurement, Science, New Series, Vol. 103, No. 2684. (Jun. 7, 1946), pp. 677-680. Available at:http://marces.org/EDMS623/Stevens%20SS%20(1946)%20On%20the%20Theory%20of%20Scales%20of%20Measurement.pdf
41. Tomaschek, K., Olechowski, A. L., Eppinger, S. D., & Joglekar, N. R. (2016). A Survey of Technology Readiness Level Users. In INCOSE International Symposium (IS 2016) (Vol. 26, pp. 2101–2117). Edinburgh, UK. https://doi.org/10.1002/j.2334-5837.2016.00283.x
42. US Department of Defense, "Technology Readiness Assessment (TRA) Guidance," 2011. Available: http://www.acq.osd.mil/chieftechnologist/publications/docs/TRA2011.pdf.
43. Yasseri S. (2013). "Subsea system readiness level assessment" Int. Journal of Underwater Technology 31: 77–92
44. Yasseri S., (2014). "Application of system engineering to subsea development," Int. Journal of Underwater Technology,32:93–109
45. Yasseri S. (2015). Interface management of subsea field development. Underwater Technology Vol.33, No. 1, pp 41–57.
46. Yasseri S. (2015). "Evidence-based subsea engineering," Int. Journal of Underwater Technology Vol. 32, No. 4, pp. 231-244.
47. Yasseri S., (2016), "A measure of subsea readiness level development," Int. Journal of Underwater Technology Vol. 33, No. 4, pp 215-228.
48. Yasseri S. Bahai, H and Yasseri, R., (2018a). "A Systems Engineering Framework for Delivering Reliable Subsea Equipment," 2018-TPC-035, ISOPE 2018, Japan. Accepted for publication
49. Yasseri S. Bahai, H and Yasseri, R., (2018b). "Reliability Assurance of Subsea Production Systems: A Systems Engineering Framework, IJCOE Vol.1, No. 1, pp 31-46.

INTERNATIONAL JOURNAL OF
COASTAL, OFFSHORE & ENVIRONMENTAL ENGINEERING IJCOE Vol.3/No. 2/Summer 2018 (45-55)

Available online at: www. Ijcoe.org

A Knowledge Based Decommissioning Alternative Selection System for Fixed Offshore Oil and Gas Platforms in Persian Gulf

Mohammadsaeid Bagheri Nia[1], Pedram Edalat[2*]

[1] *Offshore Engineering Department, Petroleum University of Technology; msbagherinia@strategist.academy*
[2*] *Offshore Engineering Department, Petroleum University of Technology; edalat@put.ac.ir*

ARTICLE INFO

Article History:
Received 23 Jun. 2018
Accepted 12 Sep. 2018

Keywords:
Strategy Selection System
Economic Analysis
Offshore Platforms
Decommissioning
Offshore Wind Turbine

ABSTRACT

Complexity and costly nature of operations involving in the decommissioning process require huge investments to be done during the lifetime of the field for its decommissioning phase of the total project. This work offers a knowledge-based decommissioning alternative strategy selection system for fixed offshore jacket platforms in the Persian Gulf. In this method, the alternative option of installing offshore wind turbines (OWT) as the most probable economic feasible alternative to decommissioning on an abandoned platform jacket structure in the Persian Gulf is proposed. In this regard, costs and benefits study between two strategies are considered; one total decommissioning and the other installing an OWT on the jacket structure of a local platform in the region. It is found that the second strategy is beneficial and saves near 9 million US dollars for company. Also, the company earns the technology and experiences with OWT installation and operations and would be a technical leader in the region for coming years. Moreover, this strategy contributes to reducing the rate of greenhouse gas emissions, improving environmental sustainability.

1. Introduction

The decommissioning process is constantly challenged with indeterminate risks associated with deteriorated structures and the practice of late-life decommissioning planning. Complexity and costly nature of operations involving in the decommissioning process require huge investments to be done during the lifetime of the field for its decommissioning phase of the total project. The issue is further complicated by the absence of a fit-for purpose decision framework. There are some optional alternatives to decommissioning which are depended on the availability of tourism, aquaculture or environmental energy potentials.

Traditional business priorities for oil and gas operators have always been securing new hydrocarbon reserves, embarking on greenfield projects and revitalizing brownfields. It is an important consideration that at the end of their commercial lives, these projects must be decommissioned in a sustainable and socially acceptable manner [1].

In Iran, there are more than 57 active jacket platforms and more than 150 wellhead jacket structures in charge of the National Iranian Oil Company as its offshore production segment in the Persian Gulf, which most of them are built more than 25 years ago. As the design life of these platforms is in the range of 20 to 30 years, they are needed to be demolished or reused depending on their belonged reservoir conditions. In this regard by considering non-economical and insufficient reservoir conditions, "decommissioning" process would be necessitated.

Decommissioning is, by definition a complex undertaking by the operator of an offshore oil or gas facility which entails planning and implementing the method of dealing with disused facilities [2]. Decisions in decommissioning activities are bounded by governance from various international regulatory bodies and organizations, such as International Maritime Organization and United Nations Convention on the Law of the Sea. It is understood from such regulations that "abandoned or disused offshore installations are required to be removed, except where non-removal or partial removal is consistent with the guidelines" [3].

The oil and gas industry has been decommissioning structures in the U.S. Gulf of Mexico for over four decades. Since 1973, over 4500 structures have been removed in the GOM and the technologies and operational practices are well established [4]. In this regard, in 2009, U.S. Department of the Interior Bureau of Safety and Environmental Enforcement presented an overall report of decommissioning approaches and costs for removal of GOM US Outer Continental Shelf

oil & gas facilities in greater than 400 ft. water depth. The mentioned report provided a solid background in the variety and complexity of offshore decommissioning and the technology and methodology available. The cost sections allowed the reader to piece together various costs and get an understanding or a general estimate of the total cost for a particular type of structure with various specifications [5].

The removal of offshore platforms is generally perceived to be more complicated than newly built installations. Up-to-date information on the platform's in-situ structural integrity is critical for effective planning of a decommissioning campaign. In dealing with aged offshore facilities, there is an inherent uncertainty with the in situ structural condition which has been subjected to various extreme loads and accidents, which may not be documented thoroughly during its operation. Platform end-of-life dates are considered to be very dynamic in nature which adds to the complications of planning decommissioning activities and resources [6].

In 2010, the report "Decommissioning cost update for removing pacific OCS region offshore oil and gas facilities" presented a review of the decommissioning practices for oil and gas facilities and developed benchmark costs for decommissioning the facilities utilizing conventional technologies. This report included cost assessments specific to the Pacific region operations and included reviews of the availability and capability of derrick barges; support vessel services; well plugging and abandonment services; abrasive, mechanical and explosive cutting services; disposal options; and site clearance services available along the west coast of the country. The Pacific OCS decommissioning cost report was updated in 2017 [7].

ProServ Offshore has provided the work decomposition algorithms to estimate cost for well plugging and abandonment, conductor severance, and removal, pipeline abandonment, umbilical and flow line removal, and platform removal for 53 Deepwater fixed platforms and compliant towers in the Gulf of Mexico circa January 2013 [8].

In response to this evolving economic, technical, and legal/regulatory context, the California Natural Resources Agency has begun investigating the issues surrounding alternatives for decommissioned platforms in the state Tidelands and on the OCS from 2007. This project focused on collecting, organizing, and summarizing as much as possible of the available information about the implementation process and impacts (both positive and negative) of alternative decommissioning options for offshore oil and gas platforms in southern California and evaluation of economic and technical feasibility of a range of decommissioning options and prioritizing for more detailed analysis for those most feasible and most applicable to California platforms [9].

According to the considerable natural potential of offshore renewable energies such as wind, the application of offshore wind turbines on oil and gas jacket structures after the end of the predicted economic life of their belonged oil field can be as an alternative option to decommissioning. For example, in 2007, China National Offshore Oil Corporation used an offshore wind turbine on an abandoned jacket structure named as SZ36-1, located in the Liaodong Bay at a depth of 31 meters after the end of its economic life in order to generate power from offshore wind energy [10].

The objective of this paper is to evaluate the economic costs and benefits of two strategies; one considering the full decommissioning process assuming a jacket platform which its field economic lifetime is finished in the Persian Gulf by equalization of available decommissioning cost data for the most similar platform and environmental conditions in GOM provided by the U.S. Department of Interior Bureau of Safety and Environmental Enforcement for the current time due to lack of technical experiences and relevant decommissioning cost data in region; the other considering an alternative strategy to decommissioning process which is the application of an offshore wind turbine on the abandoned jacket structure of the mentioned platform in the Persian Gulf.

2. Theory and Methodology

This research proposes a model for the planning and management of fixed offshore structure decommissioning activities at the end of design lifetime, with joint consideration of various technicalities of decommissioning alternatives especially offshore wind turbines in the region. A specific case study on one of the platforms in the Persian Gulf is provided as a benchmark in this paper. The developed model presents a framework which is anticipated to guide business units and asset managers to plan ahead and optimize resources for a decommissioning campaign. This will result in faster and more effective decisions, taking into account the subjectivity of in-situ degraded structural conditions. The focus of the work is on the ranking of feasible decommissioning alternatives based on their input structural parameters and optimal project planning. The end product of this research is integrated as a conceptual decommissioning decision aid toolbox into existing platform databases.

2.1. A new paradigm in decommissioning decision making

Dealing with aging assets in mature basins requires up-to-date asset information as it is a key representation of decision making knowledge [11]. This does not only cover the existing structural conditions of the asset but also track records and relevant historical operating or modification repositories. Present models tend to place

more emphasis on cost and environmental factors which diminishes the consideration of in-situ conditions of existing structural elements during the decommissioning planning process.

The lack of foresight in structural conditions may lead to unforeseen operational glitches or setbacks during the campaign [1]. Essential information required for decommissioning, for instance, as-built drawings, construction sequence, repairs, and modifications, should be collected, maintained and revised throughout a structure's operational lifetime. This information and knowledge should be organized so that those pertinent to decommissioning are effortlessly identified and utilized. Asset information comes from various sources over the life cycle of the asset but needs niche attention to identify and manage decommissioning related risks [12].

Keeping track on the number of offshore assets and their decommissioning priorities has always been an intense task for many asset owners. A platform can generally be earmarked for decommissioning due to unfavorable economics or old age. The in-situ structural condition of an old platform is a highly multivariate problem incorporated into the decommissioning challenge which is impossible to be processed by a single human expert. This work develops a novel algorithm for embedding relevant structural parameter into the decommissioning model via an expert knowledge-based system.

The outcome is a localized, relative scale which provides asset managers a rational basis for decision making for decommissioning planning and management throughout the lifecycle of an offshore asset.

2.2. Decision making in decommissioning

Eventually, any field development will reach the end of its economic lifetime. The economic lifetime is introduced as the point at which the annual net cash flow turns permanently negative. This is the time at which income from production no longer exceeds the costs of production and marks the point when decommissioning should occur since it does not make economic sense to continue to run a loss-making venture. Technically, the production of hydrocarbons could continue beyond this point but only by accepting financial losses. Figure 1 shows the economic lifetime according to net cash flows of income and costs of a platform and belonged life-extending ways. There are two ways to defer decommissioning:

- Reduce the operating costs, or
- Increase hydrocarbon throughput.

Operating costs represent the major expenditure late in field life. These costs will be closely related to the number of staff required to run a facility and the amount of hardware they operate to keep production going. The specifications for product quality and plant up-time can also have a significant impact on running costs. On the other hand, when production from the reservoir can no longer sustain running costs but the operating life of the facility has not expired, opportunities may be available to develop nearby reserves through the existing infrastructure. This is becoming increasingly common as a method of developing much smaller fields than would otherwise be possible.

At the end of the platforms economic lifetime, which any project is avoidably faced with, there are two options of different decision-making scenarios which are both different in concept and outputs. Decommissioning or leaving the platform/jacket structure in place for alternative applications are the two main options in front.

Total decommissioning of platforms located at shallow or intermediate waters and disposing of the topside and the jacket on shore or partial removal of jacket platforms located in deeper waters as part of the conversion to an artificial reef would be the most possible options from the traditional point of view. As it is obvious from Figure 2 there are other applications recently considered as brave alternative applications which are depended on the platform environmental, logistic conditions and potentials. These options include aquaculture, instrumentation and alternative power generation. Depended on the platform conditions, instrumentation as a diving platform or a tourism landmark might be from some attractive alternative solutions instead of the abandonment and decommissioning of the platform. Offshore LNG export terminal is another kind of abandoned platform application after its economic lifetime. There are some strong and hidden aspects of energy at oceans such as wind, wave, current and solar energy which would be a strong cause to claim the platform or its jacket structure for power generation applications as the default basement for the arrangement of some feasible energy converters.

2.3. Strategy selection model

Lowering total costs as well as increasing total income and decreasing environmental impacts are from those brave aspects of interests for all managing teams including governments, owners, contractors, and operators.

In the offshore segment; oil & gas platforms are designed for the nominal economical lifetime of the belonged field reservoirs and would be subjected to the decommissioning process finally. Making the decision to start the decommissioning process for a platform would be as the commencement of a massive costly and time-consuming phase in the last part of the platform life cycle. There are some Innovative Ideas which are considered as alternatives to decommissioning process in strategy selection phase before the decision making step. Innovations are suggested depending on different available potentials for each platform.

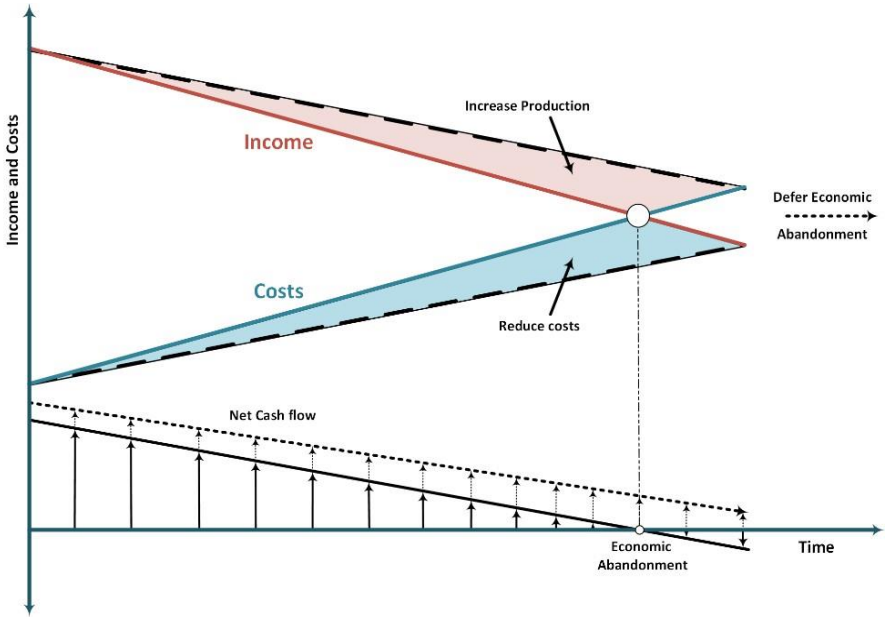

Figure 1. Representation of a Platform Economic Life Time

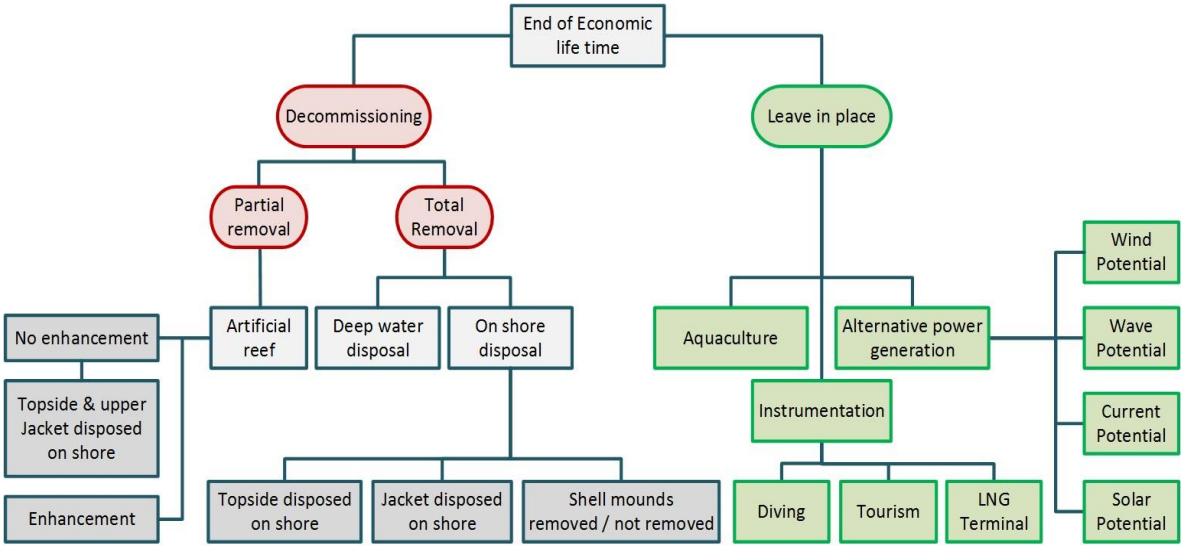

Figure 2. Summary of Decommissioning Strategies

An alternative decision related to any specific potential requires that special technological and economic feasibility study to be done.

The innovative strategy selection process starts right after the end of the platforms design life or even if any economical deficiency resulted from sudden field condition variation has been occurred. In some cases, a new potential field is discovered around or near the platforms belonged fields and its economic efficiency has been proved, so it may be worthy to rehabilitate the platform in order to extend its lifetime as much as the new economic lifetime of the discovered field would be. By the way, well plugging and abandonment are necessitated and the platform reaches to the point at which the final decision has to be made, whether to decommission or to change its application.

From the traditional point of view, the decommissioning process would unavoidably be the next decision, but from an innovative strategy selection point of view, this process can be avoided at the expense of some rehabilitation if needed and a new era of the platform economic life in an alternative application would be started. In order to reach the best result and to find the most appropriate solution, it requires an accurate study of the environmental potentials of the platform to be done. This assessment includes aspects of the economic viability of the potential alternative applications for jacket structure and for each alternative potential, required technological and economical rehabilitation feasibility if needed. Figure 3 shows a schematic overview of the mentioned strategy selection model for offshore oil and gas platforms.

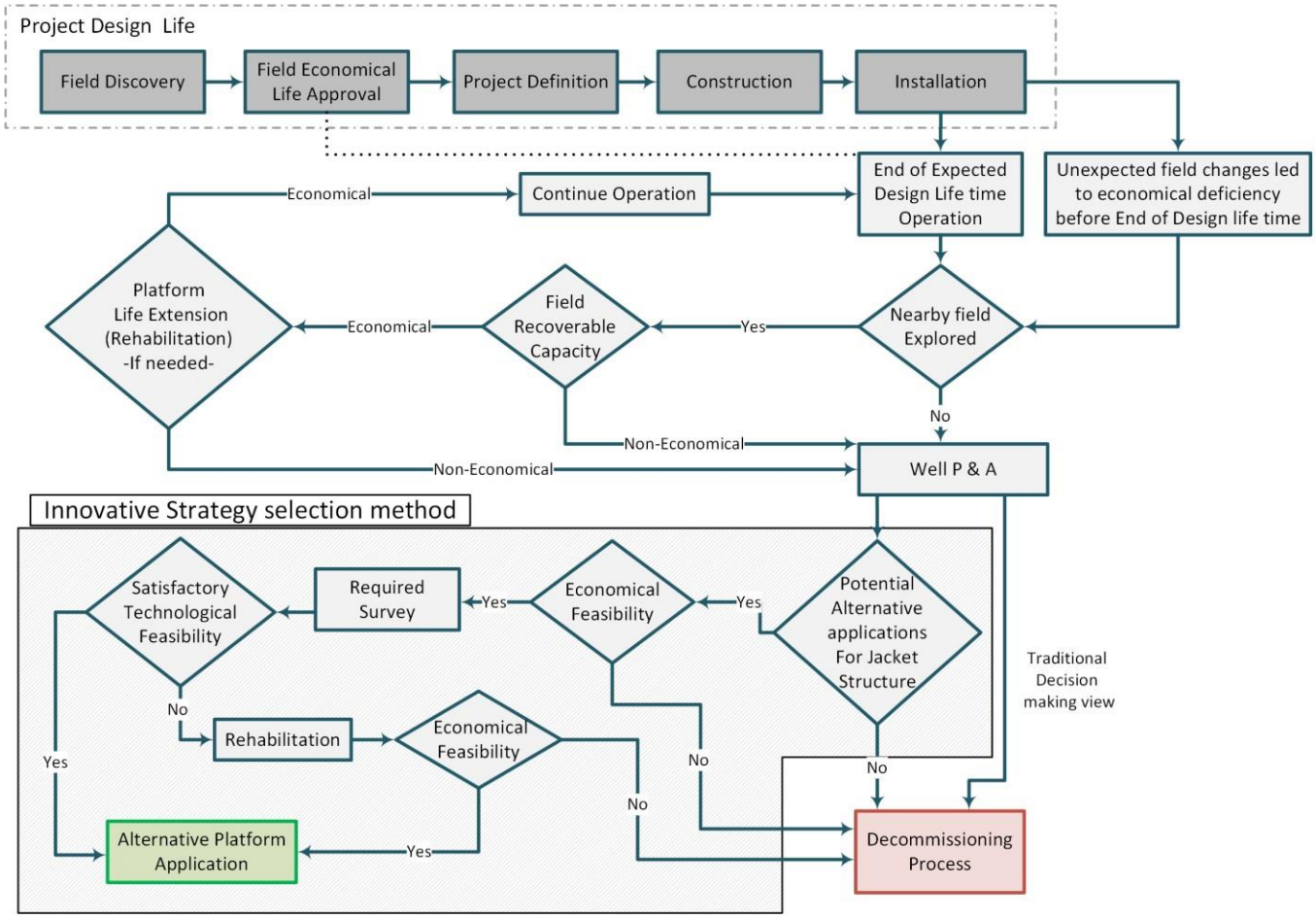

Figure 3. Strategy Selection Model at the End of Design Lifetime

2.4. OWT as an alternative to decommissioning in the Persian Gulf

Among all other alternatives mentioned above offshore wind will make a substantial contribution in Iran's energy policy requirements and similarly there is an extensive increasing worldwide trend for offshore wind turbine power generation field installations as well as an active proved tendency to develop their green energy production capacity. Potentially in addition to less turbulence and no visual or auditory annoyances, offshore wind turbines generate power more than onshore types because of the higher relative wind speed and zero roughness of the interface between the sea and the wind surface. Depending on water depth and environmental conditions offshore wind turbines are designed with different base and foundations such as mono-piles, tri-pods, and jackets for relatively shallow water fields and floating foundations for deeper potential wind fields. Installed offshore wind turbines in the world almost use mono-pile foundation and less than 20% use jacket substructure. Undoubtedly, this is due to the prevalence of shallow water locations and the maturity of this proven design, which has been almost the default choice in water depths up to 25 m with a firm seabed. But as seabed infirmity, turbine size and water depths increase, mono-pile support structures become less attractive due to rapidly growing hydrodynamic loads around large pile diameters, increasing structural flexibility at deeper water depths and complicated manufacturing with time-consuming installation processes.

Many works have investigated different solutions for the support of OWTs in general locations. For turbines over 5 MW and medium water depths of 30-60 m, jacket support structures are a coherent evolution of mono-pile that, in the last years, have evolved from prototypes to fully commercial deployments. With the development of technology in offshore oil and gas industries, jacket foundations are regarded as an alternative for the intermediate water depths (30-90m). Using jacket foundations for offshore wind turbines has the advantages of having lower ultimate loads and employing mature technologies from the offshore oil and gas industries.

The upper foundation components (column and nacelle) have the same design for each case and the only difference would be the dimensions of the turbine. As deeper the water and far from the shore; more the obtainable wind energy and consequently desirable larger turbine dimensions. Considering the situation of an oil & gas platform economical life abandonment time, the idea of using its well designed and already installed platform jacket for another application such as offshore wind turbine foundation glints. Of course,

there would be required lots of precautions before strategy selection to use the jacket as the base for the turbine or not, such as sub-sea inspections, geotechnical analysis of soil-pile interactions and structural resistance analysis considering special wind turbine loadings on an old jacket. In case of satisfactory analysis results, there is no need for some extra costs for the jacket and cable removal from the seabed. Nowadays offshore wind turbines have reached to an obtainable power capacity of more than 8 MW per tower, of course, depending on the wind speed. General dimensions of an offshore wind turbine with mentioned capacity are about 220m height and 160m blade diameter [13]. From the available environmental potentials at the Persian Gulf and feasible technological industries in Iran, using the platform jacket as the foundation for wind energy converters would be the most probable economic feasible alternative to the complex and costly process of decommissioning either total or partial removal.

Due to the absence of installed or operating offshore wind projects in Iran, the offshore reference project data are estimated from proposed U.S. projects and market data from the existing international offshore wind industry. As domestic and global wind markets mature, information about component-level costs is increasingly available. To manage and organize this component-level cost data, U.S. National Renewable Energy Laboratory has developed a system cost breakdown structure to break an entire wind project into smaller, more specific components [14]. It provides a standardized approach to characterizing total lifetime expenditures for wind projects at the component level, including both physical (e.g., materials, labor, and equipment) and financial costs (e.g., insurance, construction financing, profit, and carrying charges). Mentioned developed breakdowns for Capital Expenditures are shown in detail in Figure 4.

By application of an abandoned platform jacket as the substructure for OWT as an innovative strategy, three costly stages of Electrical Infrastructure, Site Access and Foundation, and sequentially their share in other fractions of CAPEX for a reference wind plant project such as Construction Finance, Contingency, Development, Engineering and Management should not be considered.

On the other hand, although there are some different steps for the innovative strategy especially in parts related to the jacket, power cable, and OWT, there are other common steps with the whole decommissioning strategy that should be considered in total CAPEX. Figure 5 shows two mentioned strategies in steps of common and different elements. For strategy number one, the total decommissioning process is implemented as it was discussed before. Strategy number two includes Project Management, Engineering & Planning, Inspection & Permits, Well P & A, Topside preparation, Pipeline abandonment, Conductor removal, Mobilization & Demobilization of Derrick Barges for topside, Topside removal and disposal, OWT assembly and installation, Power generation for at least 20 years, Mobilization & Demobilization of Derrick Barges for OWT, Removal & disposal of OWT, Mobilization & Demobilization of Derrick Barges for jacket, Removal & disposal of jacket and finally site clearance.

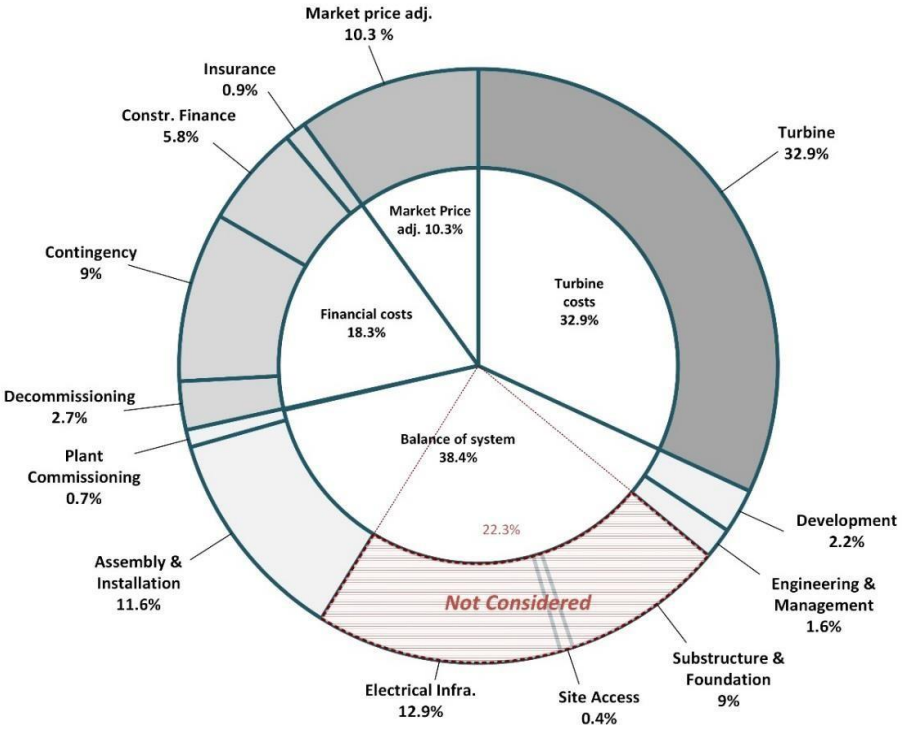

Figure 4. Capital Expenditures for the Offshore Reference Wind Plant Project [14]

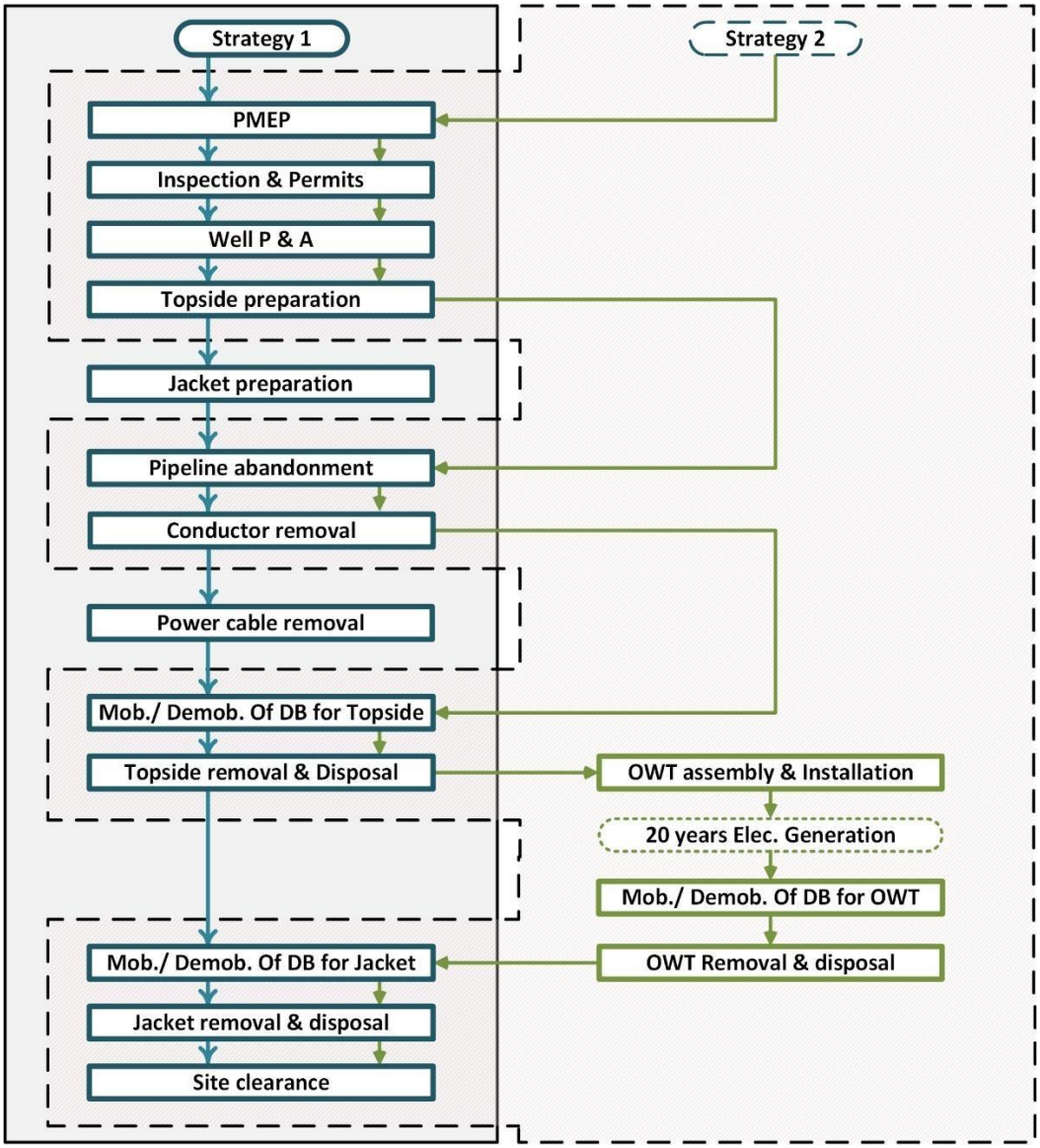

Figure 5. Common and Different Sequences of Both Strategies

3. Results and Discussion

The scope of this paper is to evaluate the economic costs and benefits of two strategies; one considering the full decommissioning process for a jacket platform in the Persian Gulf named "Ilam" which its field economic lifetime is assumed to be finished. Due to lack of technical experiences and relevant decommissioning cost data in region, this process is done by equalization of available decommissioning cost data for "Houchin" the most similar platform and environmental conditions in GOM; provided for the current time by the U.S. Department of Interior Bureau of Safety and Environmental Enforcement; the other considering an alternative strategy to decommissioning process which is the application of an offshore wind turbine on the assumed jacket structure of the Ilam platform in the Persian Gulf. Houchin is a production platform located in 50m water depth on "Carpinteria" field which has been developed late in the 60s, 1.15 kilometers far from its host platform. This field has 35 production or injection wells and conductors. Houchin exports its products to its host via four 1.15km length pipelines of different diameters and is connected to the same length power cable to the host platform [15]. Ilam is a production platform located in 50m water depth on Esfand field in the Persian Gulf which has been developed late in the 60s, 18 kilometers far from Sirri island in the southeast. The field has 4 other offshore platforms including 3 well platforms and one flare. This field has 29 production or injection wells and conductors. Ilam exports its product to Sirri island via an 18km length, 16-inches diameter pipeline and is connected to the same length power cable to the island. One of the most important applications of its production is to supply the required feeds for power plants in "Kish" and "Qeshm" islands. The arrangement of the field and mentioned islands are shown in Figure 6.

In order to compare that how much value the investment on each project adds to the company a comparative financial indicator is required for both strategies.

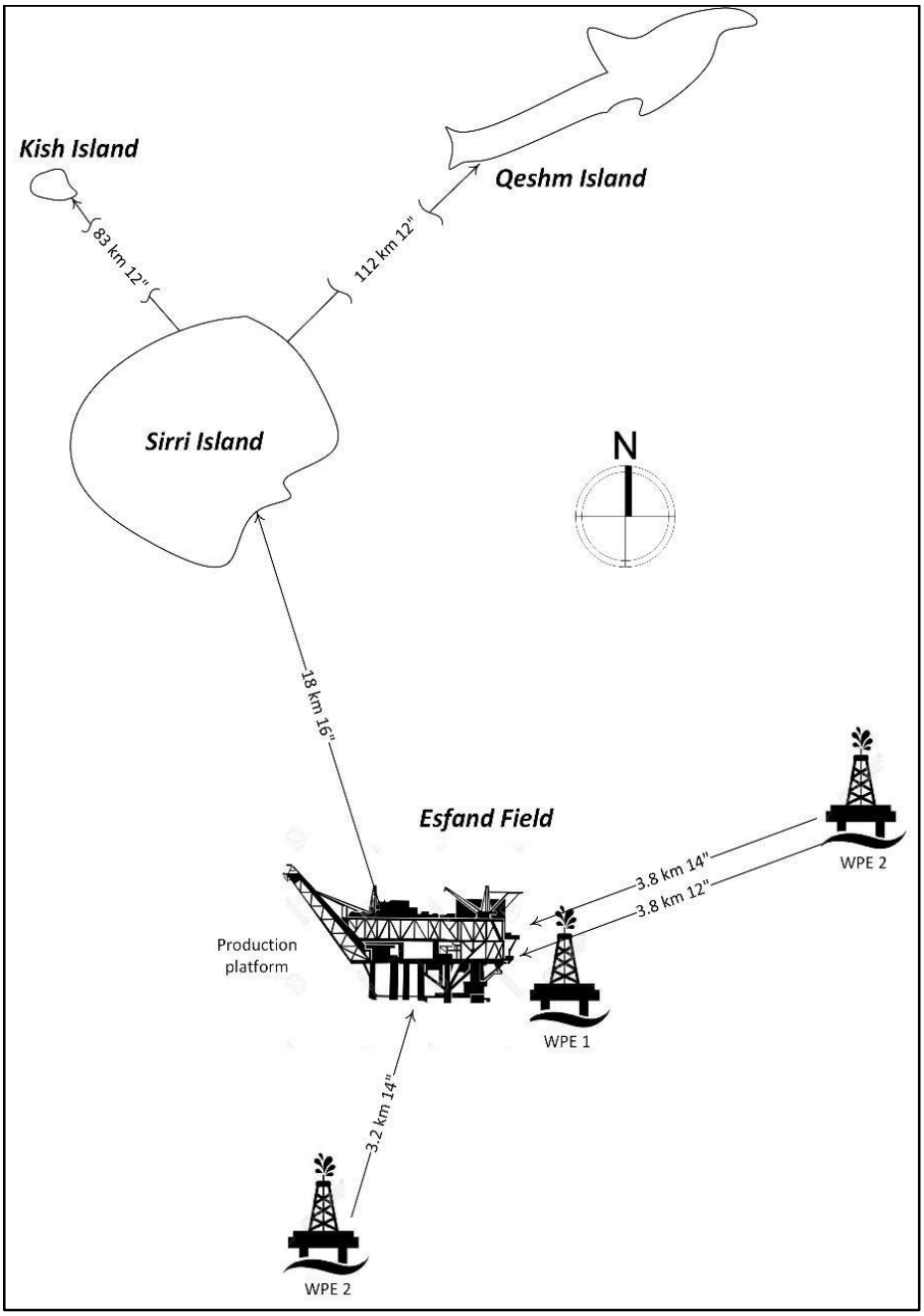

Figure 6. The Arrangement of Esfand Field in the Persian Gulf

The economic evaluations are based on the Net Present Value method. NPV is calculated considering the system lifespan, the interest factor, the total investment cost, annual income and the Weighted Average Cost of Capital. In finance, the NPV or Net Present Worth is a measurement of the profitability of an undertaking that is calculated by subtracting the present values of cash outflows from the present values of cash inflows over a specified period of time. Initial costs are included in cash outflows. Outgoing and incoming cash flows can also be described as cost and benefit cash flows respectively. Each cash inflow/outflow is discounted back to its present value then summed and the NPV is the sum of all the present values for each investment step. The rate used to discount future cash flows to the present values is the Weighted Average Cost of Capital considering risk and opportunity cost of the capital for the company. The Net Present Value of a project is calculated from the following formula as Eq. (1).

$$NPV = CF_0 + \sum_{t=1}^{n} \frac{CF_t}{(1+i)^t} \quad (1)$$

Where CF_0 is the cash flow at the year zero (Initial Cost), CF_t is the Project's Cash flows, t is individual year of lifetime (1a, 2, …, n), i is the Weighted Average Cost of Capital in percent (here = 10%) and n is operational lifetime in year.

Table 1 lists the cost categories of a total decommissioning process converted to the current time for the platforms “Houchin” and “Ilam”. Cost values

for "Ilam" are scaled from available data of its similar platform "Houchin" considering Persian Gulf location. As it is evident in table 1; if the company selects the first strategy at the end of the economic life of the field "Esfand", total decommissioning of the platform will cost around 40.5 million US dollars for the current time.

Table 1. Strategy Number 1

Total Decommissioning Costs by Category			
	Categories	Platform Name	
		Houchin	Ilam
1	Platform Removal	6,881,370$	6,634,943$
2	Platform Preparation	1,146,335$	1,146,335$
3	Well P&A	6,893,125$	5,711,447$
4	Conductor Removal	2,828,527$	2,343,637$
5	Pipeline Decommissioning	668,025$	2,614,013$
6	Power Cable Removal	358,156$	5,756,077$
7	Site Clearance	923,780$	923,780$
8	Weather Contingency	1,845,511$	1,845,511$
9	Miscellaneous Work Provision	2,768,267$	2,768,267$
10	Permitting & Regulatory Compliance	2,076,918$	2,076,918$
11	Mobilization & Demobilization of DBs	7,759,125$	4,914,112$
12	Materials Disposal	2,215,039$	2,189,392$
13	PMEP	1,575,945$	1,575,945$
	Total Decommissioning Cost (NPV)	37,940,122$	40,500,377$

$$NPV = CF_{01} + \sum_{t=1}^{20} \frac{CF_{t1}}{(1+0.1)^t} = -40{,}500{,}377\$$$

On the other side, by selecting the other strategy the company saves near 9 million US dollars in comparison to the first strategy; as listed in table 2, the costs of the yearly operations and maintenances ($OPEX$), yearly revenue earned from electricity exporting from the platform ($ElecR$) and saved fuel required for the generation of the same amount of power ($FuelR$), are included and converted to the current time considering constant prices for electricity and fuel during the whole length of the project, Eq. (2). Furthermore, the company earns the technology and experiences with OWT installation and operations and would be a technical leader in the region for coming years as well as improving the total rate of greenhouse gas emission production in the region.

Table 2. Strategy Number 2

OWT as an Alternative to Decommissioning		
	Categories	Platform Name
		Ilam
1	Platform Removal (Topside)	3,544, 487$
2	Platform Preparation (Without Marine Growth Removal)	586,890$
3	Well P&A	5,711, 447$
4	Conductor Removal	2,343,637$
5	Pipeline Decommissioning	2,614,013$
6	Power Cable Removal	0$
7	Site Clearance	0$
8	Weather Contingency	1, 489,142$
9	Misc. Work Provision	2, 233,714$
10	Permitting & Regulatory Compliance	2,076,918$
11	Mobilization & Demobilization of DBs (Topside)	2,624,137$
12	Materials Disposal (Topside)	1,162,915$
13	PMEP	1, 271,630$
14	Alternative Decommissioning Cost (NPV)	25,658,930$
15	Total Capital Expenditures (CAPEX) of a 3.39 MW OWT [1]	14,773,510.2$
16	Total Annual OPEX [2]	467,820$/*year*
17	Net Annual Produced Electricity Revenue for a 3.39 MW OWT [3]	1,510,952.832$/*year*
18	Net Annual Saved Fuel Revenue for the Same Capacity	33,026.2$/*year*
Total Cost (For 20 years) (NPV)		31, 270, 491$
[1] Without Considering the Costs of Substructure & Foundation, Site Access, and Electrical Infrastructure		
[2] Operational & Maintenance Expenditures of Jacket & 3.39MW OWT		
[3] According to Iran's Electricity Guaranteed Purchasing Base Rate [16] (With Considering Turbine Net Capacity Factor of 42.4%)		

$$NPV = CF_{02} + \sum_{t=1}^{20} \frac{CF_{t2}}{(1+0.1)^t}$$

$$CF_{02} = -25{,}658{,}930\$ - 14{,}773{,}510.2\$ = -40{,}432{,}440.2\$$$

$$CF_{t2} = OPEX_t + ElecR_t + FuelR_t \qquad (2)$$

$$OPEX_t = \frac{-138\$}{kW.year} \times \frac{1000kW}{MW} \times 3.39MW = \frac{-467{,}820\$}{year}$$

$$ElecR_t = \frac{120\$}{MWh} \times 3.39MW \times \frac{8760hr}{year} \times 0.424 = \frac{1{,}510{,}952.832\$}{year}$$

$$FuelR_t = \frac{932{,}415.5kg}{year} \times \frac{0.023\$}{m^3} \times \frac{1.54m^3}{kg} = \frac{33{,}026.2\$}{year}$$

$$NPV = -40{,}432{,}440.2\$ + \sum_{t=1}^{20} \frac{-467{,}820}{(1+0.1)^t} + \sum_{t=1}^{20} \frac{1{,}510{,}952.832\$}{(1+0.1)^t} + \sum_{t=1}^{20} \frac{33{,}026.2}{(1+0.1)^t} = -31{,}270{,}491\$$$

By using the 3.39 MW NREL offshore wind turbine as an alternative to jacket decommissioning of the mentioned platform, the total cost of the process is decreased by 22.78%, retrieving more than 9 million US dollars for the company. Figure 7 shows the cost comparison between both strategies. The cash flow percentages against different cost categories of decommissioning work breakdown and the cost of yearly operations, yearly revenue earned from electricity exporting and fuel saving are presented in details.

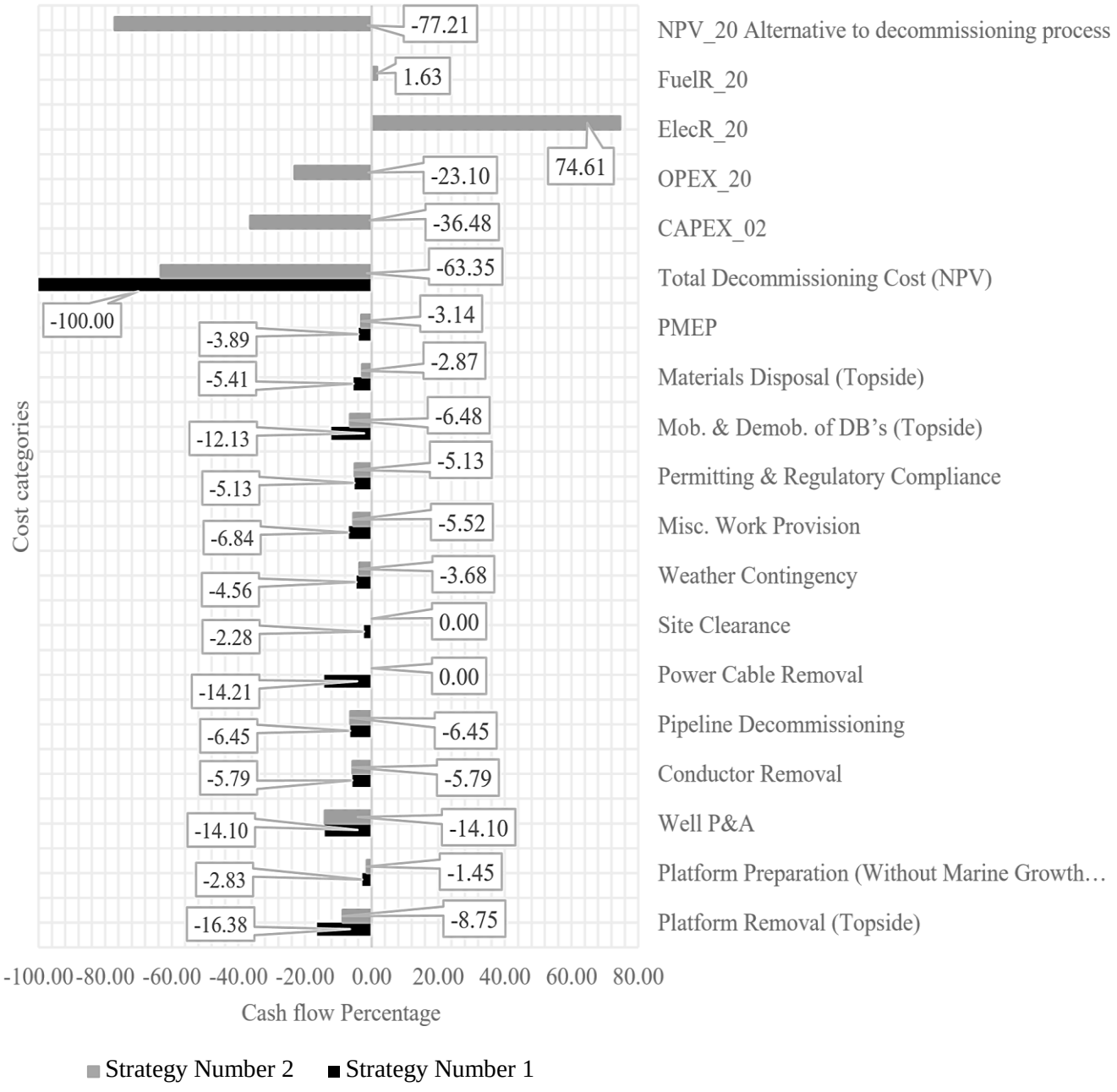

Figure 7. Strategy No.2 Costs Compared to Strategy No.1 (in percentage)

4. Conclusions

A knowledge-based decommissioning alternative strategy selection system for fixed offshore jacket platforms has been introduced in this study. The economic costs and benefits of two strategies were evaluated; the first strategy involves the full decommissioning of a jacket platform (Strategy Number 1), and the second strategy proposes the installation of an offshore wind turbine (OWT) on the existing jacket structure in the Persian Gulf (Strategy Number 2) as an alternative to decommissioning. The results show that the second strategy reduced the total decommissioning costs by 22.79%, saving the company over 9 million dollars. In addition to the economic advantages, adopting the OWT installation strategy equips the company with advanced technology and operational experience, positioning it as a technical leader in the region for the foreseeable future. Furthermore, this strategy contributes to reducing the overall greenhouse gas emissions in the region, enhancing environmental sustainability.

5. References

[1] World Bank Oil, Gas and Mining Policy and Operations Unit (COCPO), (2009), *Towards Sustainable Decommissioning of Oil Fields and Mines: A Toolkit to Assist Government Agencies.*

[2] Climate and Pollution Agency, (2010), *Decommissioning of Offshore Installations*, Department of Climate and Industry, Oslo.

[3] Lyons, Y., (2010), *Disused Offshore Installations in Southeast Asia: The Legal Story*, Retrieved from Centre for International Law: http://cil.nus.edu.sg/wp/wp-content/uploads/2010/08/YounaLyons-DisusedOffshore-Installations-DecomWorld.pdf⟩

[4] Siems, G.L., (2016), *Decommissioning Process Optimization Methodology*, Offshore Technology Conference, Houston, Texas, USA.

[5] TSB Offshore, (2009), *Decommissioning costs for removal of GOM US Outer Continental Shelf (OCS) oil & gas facilities in greater than 400 ft. water depth*, U.S. Department of the Interior Bureau of Safety and Environmental Enforcement, Virginia.

[6] KPMG Global Energy Institute, (2015), *Decommissioning Strategy: A New Imperative for E & P Firms*, KPMG LLP, United Kingdom.

[7] TSB Offshore, (2017), Decommissioning cost update for removing pacific OCS region offshore oil and gas facilities, U.S. Department of the Interior Bureau of Safety and Environmental Enforcement, Virginia.

[8] Kaiser, M.J., and Liu, M., (2014), *Decommissioning cost estimation in the deep water U.S. Gulf of Mexico – Fixed platforms and compliant towers*, Marine Structures, vol. 37, pp. 1-32.

[9] Bernstein, B. B., (2008), *Evaluating Alternatives for Decommissioning California's Offshore Oil and Gas Platforms*, California Ocean Science Trust, California.

[10] Wang, Y., Duan, M., and Shang, J., (2009), *Application of an Abandoned Jacket for an Offshore Structure Base of Wind Turbine in Bohai Heavy Ice Conditions*, International Offshore and Polar Engineering Conference, Osaka, Japan.

[11] International Atomic Energy Agency, (2008), *Long Term Preservation of Information for Decommissioning Projects*, International Atomic Energy Agency, Vienna.

[12] Thornton, W., (2014), *Decommissioning and abandonment*, J. Pet. Technol., 102.

[13] Multon, B., (2012), *Marine Renewable Energy*, Great Britain: ISTE – Wiley.

[14] National Renewable Energy Laboratory, (2017), *Cost of Wind Energy Review*, U.S. Department of Energy, Denver West Parkway, USA.

[15] TSB Offshore, (2016), *Decommissioning Methodology and Cost Evaluation*, U.S. Department of the Interior Bureau of Safety and Environmental Enforcement, Virginia.

[16] Ardakanian, R., (2017), *Proclamation of Iran's Electricity Guaranteed Purchasing Base Rate from Renewable Energies*, Ministry of Energy, Islamic Republic of Iran. (In Persian)

INTERNATIONAL JOURNAL OF
COASTAL & OFFSHORE ENGINEERING
IJCOE Vol.3/No. 2/Summer 2018 (57-65)

Available online at: http://ijcoe.org/browse.php?a_code=A-10-171-2&sid=1&slc_lang=en

Numerical Study of Winter Shamal Wind Forcing on the Surface Current and Wave Field in Bushehr's Offshore Using MIKE21

Mohammad Pakhirehzan[1], Maryam Rahbani[2*], Hossein Malakooti[3]

[1] *Ph.D. student, Faculty of Marine Science and Technology, University of Hormozgan, Bandar Abbas, IRAN; mht_pa@yahoo.com*
[2*] *Assistant Prof., Faculty of Marine Science and Technology, University of Hormozgan, Bandar Abbas, IRAN; maryamrahbani@yahoo.com*
[3] *Associate Prof., Faculty of Marine Science and Technology, University of Hormozgan, Bandar Abbas, IRAN; hos_malakooti@yahoo.com*

ARTICLE INFO

Article History:
Received: 11 Jun. 2018
Accepted: 18 Sep. 2018

Keywords:
Persian Gulf
winter Shamal wind
MIKE21

ABSTRACT

Marine areas are affected by different atmospheric phenomena such as wind and storm. In this research the effect of a large scale atmospheric phenomenon, known as Winter Shamal Wind, is investigated on the regime of currents and waves in the northwest part of the Persian Gulf. This wind normally occurs for the period of three to seven days, during December to early March. MIKE21 Coupled Model FM was applied to study the pattern of current and waves for this period. To provide the hydrodynamic data for the model and validate the simulated results, the wind data of ECMWF and mast meteorology of coastal synoptic station of Bushehr and wave data of buoy located offshore of Bushehr was used. The results indicated only a slight increase in current speed with no significant change in current direction during Winter Shamal Wind, showing a stable current pattern in northwest of the Persian Gulf. The significant wave height and wave propagation speed for the period of Winter Shamal Wind in comparison with the days prior to the wind show significant changes. The maximum wave speed in the area under investigation reaches up to 1 m/s and the significant wave height is almost 1 meter higher than that of normal situation.

1. Introduction

The Persian Gulf is one of the most important water ways in the world. It is also the center of the richest oil resources of the world (Kampf and Sadrinasab, 2006). This Gulf is semi enclosed shallow water with the average depth of about 35 m (Azizpour et al., 2014; Thoppil and Hogan, 2010a). Its total coastline is about 3000 km., of which about 1722 km is under the territory of Iran. The mean length of this Gulf is about 1000 km, its width reaches up to 336 km at its widest area, and its depth reaches up to about 90 m at the Strait of Hormuz. The Persian Gulf is connected to the Gulf of Oman and open oceans via Strait of Hormuz (Reynolds, 1993). The direction of the winds in the Persian Gulf is mainly northwesterly throughout the year. They are mostly stronger during November to February and weaker during the June to September (Thoppil and Hogan, 2010a).

This Gulf is stretched between latitudes 24º-30º N and longitudes 48º-58º E. Its climate therefore, can be divided into two seasons and two transitional periods. Summer season starts from June and continues till September. This is followed by the autumn transition from October to November. Afterwards, December to March are known as the winter season, which is completed by the spring transition from April to May (Walters and Sjoberg, 1998).

Due to its geographical location, this Gulf is dominated by the monsoon known as Shamal wind. Shamal Wind is a climatic regime which is developed over Mediterranean Sea and extended to the Persian Gulf. It causes uneven weather conditions such as dust storms, and low level winds (Rao et al., 2003).

Shamal Wind is the only persistently strong wind in the Persian Gulf region that can last for several days with the winds which can reach strong to gale force over the open sea and routinely produce wind waves of 3–4 m high (Glejin, 2013).

The prevalent direction of the Shamal Wind is north and northwesterly (Al Senafi and Anis, 2015; Perrone, 1979). For northwesterly winds of the Persian Gulf, the plume from Shatt-al-Arab first heads towards the

Iranian coast and then spreads southeastward (Pous et al., 2013). This wind is categorized as Winter and Summer Shamal Wind. Summer Shamal Wind normally occurs between May and July, sometimes elongates till September. This wind is in connection with the interaction of thermal and seasonal climatic systems of low altitude which works over northwest India, Pakistan, Iran and Saudi Arabian high pressure. It is almost moderate wind with mean velocity of about 3 m/s (Rao et al., 2001).

Winter Shamal Wind (WSW) on the other hand, is a short term phenomenon, and can be categorized into two different types according to its persistence; one with the duration of about 1 to 3 days, and the other with the duration of about 3 to 5 days (Abdi et al., 2012). WSW can occurs 3 times per year especially by the end of December and the beginning of the March (Rao et al., 2001). It occurs when a transient low pressure front conjunct with a cold and strong passing front of the Turkey's mountains. The front edge of the cold air mass carries near surface dusts, which could cause dust storm. This wind is stronger than Summer Shamal Wind. The near surface velocity of this wind, entering to the center of the Persian Gulf, is about 15 to 20 m/s. According to Thoppil and Hogan (2010b) velocity is about 5 times stronger than its initial velocity.

Since the oceans and coastal waters are bounded by the atmosphere, every near surface atmospheric phenomena can disturb their hydrodynamic and cause the onward, upward or downward movement of ocean (Stewart, 2008). The Persian Gulf, like every other coastal waters is supposed to be affected significantly by the WSW. There are numerous literatures published with this regard such as Rao et al. (2001); and Thoppil and Hogan (2010b). There are however, little review about the effect of this large scale wind system on the dynamic of the daily waves and currents in this Gulf.

Considering the northwestern part of the Persian Gulf, which is most affected by the Winter Shamal wind, the aim of this research was to study the hydrodynamic of the area due to WSW. Due to the lack of field measurements and in situ observations in many regions, nowadays numerically simulated wave data are widely used as the data bank for extracting designed wave characteristics and for further studies with this regard (Moeini et al., 2010). The employed measured wind data was those recorded at mast meteorology of coastal synoptic station of Bushehr. They are recorded at the height of 10 m and are proper to use as initial condition of the model.

The aim of this research is to simulate wave and current pattern of the area under the effect of WSW. For this reason a numerical model should be selected.

The most vital points to achieve a right decision is the applicability of that model in the area. Another point to choose a proper model is availability of input data should be feed to that model (Arı Güner et al., 2013). Since MIKE21, developed by Denmark Hydraulic Institute (DHI), has been used successfully in different investigations area, the use of it has been considered appropriate for this study. The availability of the input data to feed to this model is also guaranteed.

2. Materials and Methods

2.1. Circulation in the Persian Gulf

As mentioned, the most investigations carried out in the Persian Gulf are focused on the main circulation in the Persian Gulf, or specifically in the Strait of Hormuz. Observations and field measurement of water properties and circulation in the Persian Gulf are limited in some temporal and spatial measuring field coverage (Yao, 2008). Surface current in the Strait of Hurmoz is always inward to the Persian Gulf (Sadrinasab, 2010) and this current continues through the Gulf to the end of the Gulf at the northeast, where this current is divided into two parts to flow along shores in the opposite direction of the main current (Fig 1).

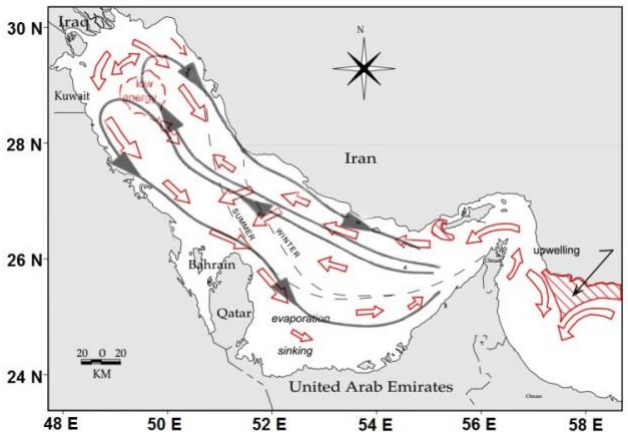

Figure 1. General circulation in the Persian Gulf (Pous et al. 2013, Reynolds 1993)

In a research by Kampf and Sadrinasab (2006), a three dimensional hydrodynamic model of the Persian Gulf was developed using Coherence software to study the full circulation through the Gulf. They claimed that the Gulf experiences two different cyclones; a cyclonic overturning circulation during spring and summer, and mesoscale eddies during autumn and winter.

Circulation in the Persian Gulf is divided into two different scales; the basin scale and mesoscale circulations. The basin scale in this Gulf is a cyclonic circulation; composed of a northwestward-flowing Iranian Coastal Current (ICC) from the Strait of Hormuz along the northern side of the basin with speeds greater than 10 cm/s and a southeastward-flowing current in the southern portion of the Gulf (Hunter, 1983; Thoppil and Hogan, 2010a). This basin scale of the Gulf is well known, due to the availability of vast literatures with this regard (Thoppil and Hogan, 2010a).

The surface current in this circulation is strong during the summer (reaches up to 20 cm/s), and is relatively weak during the winter (about 5 to 10 cm/s). The weakness of the current during winter is a result of the reduced density gradient between the Persian Gulf and the Gulf of Oman, which itself is due to the weak stratification at this time owing to the winter cooling (Thoppil and Hogan, 2010a). The strength of the cycle in the summer however, was suggested to be due the strengthening of stratification and weakening of the Shamal wind. Its magnitude reaches up to 40 cm/s. Besides, the isopycnals inclining downward toward the north is responsible for the strong long shore current.

Details of the interior circulation during summer is barely known. The basin scale can be disturbed by three or four mesoscale eddies with the diameter of about 115-130 m, which are called as Iranian Coastal Eddies (ICE). These eddies extend down to the depth and also remain stationary at their locations. These eddies diminish as soon as the winter cooling cause the collapse of the thermocline (Thoppil and Hogan, 2010a).

2.2. Shamal Wind

Shamal Wind is a strong northwesterly wind which blows over a wide area of Iraq and Persian Gulf and spread out over Saudi Arabia and Kuwait. This wind is quite strong during the day, usually slows down during the night. It happens a few times per year; mostly in summer, but sometimes in winter. The sands brought up from Syria and Jordan by this wind causes strong sand storm in Iraq (El-Baz, 1994).

Shamal wind in general, is divided into two types; the Summer Shamal Wind, and the Winter Shamal Wind (WSW). The synoptic conditions relevant to the pressure variation between the high pressure of the Northern Arabian Peninsula, Iraq and the Mediterranean Sea in one hand, and the low pressure of southern Iran and the southern Arabian Peninsula in another hand are favorable conditions for the formation of the Shamal Wind. According to Rao et al. (2001) the days in which the surface wind direction is north-westerly or northerly and the hourly mean wind speed is 17 kn (8 m/s) or more for at least three hours a day, is called Shamal day.

The Summer Shamal Wind is more famous in the area than the Winter Shamal Wind. It is also known as 120 Days Wind. It affect the region predominantly during May to July and are known to be linked with the seasonal thermal low pressure lying over north-west India, Pakistan, Iran and southern Saudi Arabia. The WSW however, is the resultant of a permanent high pressure over the Saudi Peninsula after a cold front passage. It is directly associated with mid-latitude disturbances moving from west to east and is caused by the presence of a large pressure gradient that develops after a cold front passage. Upper level subsidence in associate with rapid formation of high pressure over Saudi Arabia and Iraq reinforces the low-level northwesterly winds (Thoppil and Hogan, 2010b).

This wind normally happens several times during November till March; sometimes with the short period of 24 to 36 hours and sometimes with the longer period of 3 to 5 days. Fig 2 depicts the influence of the WSW on the air characteristics of the area under investigation during the January 2013. It can be seen that WSW is started on the 10th of the January with the speed of over 40 km/h and lasts for 5 days.

The occurrence of the WSW from 10th to 16th of January 2013 is shown in Fig 2. Prevailed north and northwesterly winds during this period is clearly observable (Fig 2d). Besides, wind speed experiences its highest value in comparison with the other days of the month (Fig 2c). The drop of the barometric pressure (Fig 2B) and the air temperature (Fig 2a) at the beginning of the WSW approve the passage of the cold front. It also can be seen that during this 5 days period the drop of the temperature is in coincidence with an increase of temperature difference between the dew point and the air, which suggests the dryness of the area during WSW (Fig 2a). These findings are also reported by other scientists, among them Rao et al. (2001); Rao et al. (2003); and Thoppil and Hogan (2010a).

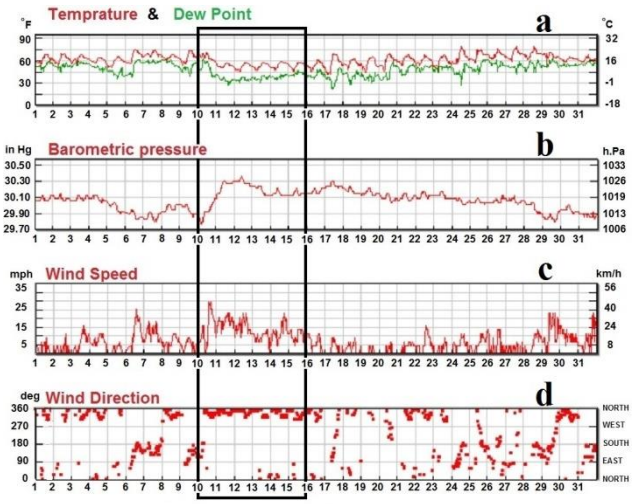

Figure 2. Temperature (a), pressure (b), wind speed (c) and wind direction (d) recorded at Bushehr station, January 2013- the black box shows the during the WSW (10th to 16th of January)- Bushehr meteorological station

2.3. Area under investigation

Bandar-e-Bushehr located in the northwest of the Persian Gulf, is a coastal city and an important port in Iran. This city can be counted as a relatively crowded port in terms of commercial and fishing activities. These activities are usually disturbed due to the WSW. Therefore, this specific area has been selected to investigate the effect of WSW on the hydrodynamic of its coastal body of water. The region has been considered for this investigation covers an area of about 9600 km^2, between longitudes 050º 00' E and 051º 07' E, and latitudes 28º 30' N and 29º 30' N. The deepest

part of the region is about 56 m, located on the southwestern part of the area (Fig 3).

Fig 4 shows the water level time series (A) and the wind rose (B) recorded at Bushehr meteorological station during January 2013. The geographical position of the buoy is: 28º 53' N, 050º 43' E. It can be seen that the wind is mostly northerly and northwesterly with the speed exceeds to 14 m/s. The figure also shows that semidiurnal tide is dominated in the area, with the tidal range of about 2 m. The horizontal line of zero water levels shows the chart datum of the Persian Gulf.

2.4. Model establishment

The two dimensional feature of the MIKE21 software has been adapted for this study. The software considers continuity, momentum, temperature, salinity and density equations for simulation. It is capable of simulating water level, flow and/or wave in the entrance of rivers, interior of gulfs, coastal areas and all other shallow and/or deep waters. The Flow module (FM) and the Spectrum Wave module (SW) of the software are adapted to use in this investigation. The ability of the software to execute coupled flow and wave module makes it suitable to perform the real situation.

Equations 1 to 3 are the conservation of mass and momentum equations which is used in this software to simulate the variation of the water level and the flow (DHI 2012).

$$\frac{\partial \zeta}{\partial t}+\frac{\partial p}{\partial x}+\frac{\partial q}{\partial y}=\frac{\partial D}{\partial t} \tag{1}$$

$$\frac{\partial p}{\partial t}+\frac{\partial}{\partial x}\left(\frac{p^2}{h}\right)+\frac{\partial}{\partial y}\left(\frac{pq}{h}\right)+gh\,\frac{\partial \zeta}{\partial x}+\frac{gp\sqrt{p^2+q^2}}{c^2.h^2}-\frac{1}{\rho_w}\left[\frac{\partial}{\partial x}(h\tau_{xx})+\frac{\partial}{\partial y}(h\tau_{xy})\right]-\Omega_q-fvv_x+\frac{h}{\rho_w}\frac{\partial}{\partial x}(\rho_a)=0 \tag{2}$$

$$\frac{\partial q}{\partial t}+\frac{\partial}{\partial y}\left(\frac{q^2}{h}\right)+\frac{\partial}{\partial x}\left(\frac{pq}{h}\right)+gh\,\frac{\partial \zeta}{\partial x}+\frac{gq\sqrt{p^2+q^2}}{c^2.h^2}-\frac{1}{\rho_w}\left[\frac{\partial}{\partial y}(h\tau_{yy})+\frac{\partial}{\partial x}(h\tau_{xy})\right]-\Omega_p-fvv_y+\frac{h}{\rho_w}\frac{\partial}{\partial xy}(\rho_a)=0 \tag{3}$$

In the above mentioned equations the relation between the water depth (h(x,y,t)), the variation of water level with time (d(x,y,t)), and the water level (ζ(x, y, t)) are related as follow:

$$h(x,y,t)=d(x,y,t)-\zeta(x,y,t) \tag{4}$$

The symbols used in the above equations are introduced in Table 1.

The spectral wave module (SW) simulates the growth, decay, and transformation of wind generated waves and swells in offshore and coastal areas. The waves in this module, are represented by the density spectrum N (σ, θ). The independent parameters are the relative angular frequency (σ = 2πf), and the direction of wave propagation (θ). The governing equation is the wave action balance equation formulated in either Cartesian or spherical co-ordinates (Komen 1996).

$$\frac{\partial N}{\partial t}+\nabla.(\vec{v}\,N)=\frac{s}{\sigma} \tag{5}$$

$$\rightarrow \frac{\partial}{\partial t}N+\frac{\partial}{\partial x}C_xN+\frac{\partial}{\partial y}C_yN+\frac{\partial}{\partial \sigma}C_\sigma N+\frac{\partial}{\partial \theta}C_\theta N=\frac{s}{\sigma}$$

where N is wave action density, σ is the relative angular frequency, θ is the wave direction, C_x, C_y, C_σ , C_θ are celerity characteristics in geographical and spectral coordinate system, and S is the energy source term, which represents the superposition of source function describing various physical phenomenon.

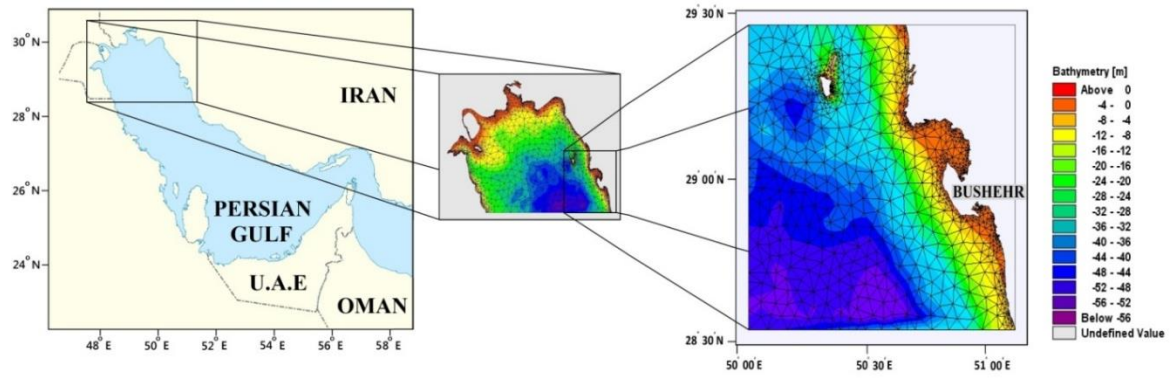

Figure 3. study area

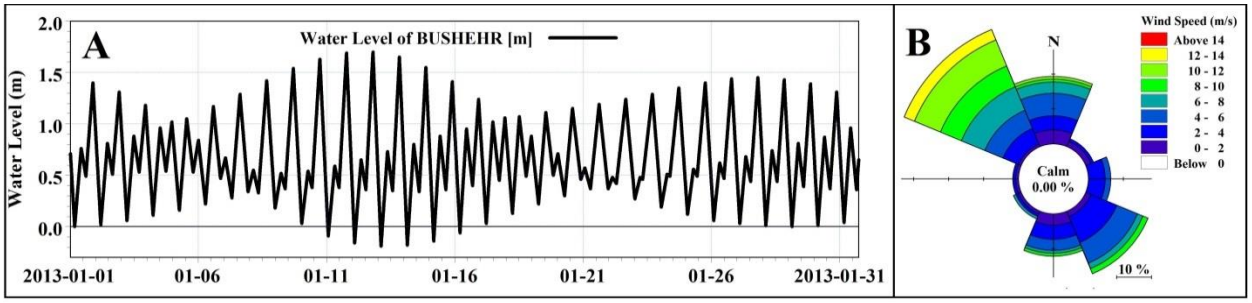

Figure 4. (A) Water level time series, and (B) Wind rose of the Busheher offshore –January, 2013

Table 1. Symbols used in equations

Phrase	Concept
$p, q\,(x, y, t)$	flux of density in the x and y direction
g	gravitational acceleration
f(v)	wind friction
V(x)	wind speed component in x direction
V(y)	wind speed component in y direction
$p_a\,(x, y, t)$	atmospheric pressure
ρ_w	water density
$\tau_{xx}, \tau_{xy}, \tau_{yy}$	shear stress components
t	time
$\Omega\,(x, y)$	Coriolis effect

$$S = S_{in} + S_{nl} + S_{ds} + S_{bot} + S_{surf} \quad (6)$$

where S_{in} represents the generated energy by the wind, S_{nl} is the wave energy transfer due to non-linear wave-wave interaction, S_{ds} is the dissipation of wave energy due to white capping, S_{bot} is the dissipation due to bottom friction and S_{surf} is the dissipation of wave energy due to depth-induced breaking (Remya 2014, Sorensen 2004).

The coupled feature of the software; SW and FM, has been adapted to simulate the surface current and also the significant wave height of the area before, during and after the WSW. The potency of simulating a phenomena considering simultaneous interaction between the flow and the wave of an area is the advantage of the usage of the coupled module. That is; the spectral wave tensions could be called directly from the SW to use in the FM module, on the other hand the variation of the water level can be reloaded from the FM module for the usage in the SW module.

For grid cells the flexible mesh has been adapted. The model has been established with the total number of the 2163 cells. The size of the grids varies from 0.5 km^2 in the area away from the coastal area, to about 0.1km^2 near the coast. The British Admiralty Nautical chart 2884 has been employed for the bathymetry of the area (Fig 3).

The wind speed and direction adapted to the model was those derived out from the ECMWF model. These data is recorded every 6 hours. The modeled area is bordered by three open boundaries at the north, east, and south, and one land boundary at the west. For the open boundary conditions the water level elevation was considered at all three open boundaries. These data are collected from mobilegeographics web page. Water level data of Khark island station, and Boushehr station were applied for the northern, and southern boundaries respectively. For the eastern boundary the interpolation method between the northern and southern water level data was employed. Considering the geographical location of the area, and taking into account the selected period for simulation, the water temperature was set to 15°, and the water salinity was set to 39 ppt.

2.5. Model calibration and validation

Validation of the model was carried out using buoy recorded data and the ECMWF reanalysis databases for the interval 27th to 31st of January 2013. This period was considered for validation, since this period was the only interval, when the buoy records was available. Three main parameters has been used for the model calibration including white capping parameter, wave breaking parameter, and bottom friction parameter. The former played the main role in this calibration. Considering reconstructing the real situation, it was found necessary to consider white capping parameter as a small value. Executing several simulations, the value of Cds=2.5 was found proper for white capping. For the wave breaking parameter the value of γ=0.8 has been choose. The bottom friction parameter was adapted to the model as Chezy coefficient. The smaller the Chezy coefficient, the bottom friction is much higher. Considering the speed of the current in the area and executing some simulations this parameter has been selected as 15.

Fig 5 shows the time series of wind speed, significant wave height and peak wave period derived out from calibrated model. The significant wave height and peak wave period of the simulation has been compared with buoy records and ECMWF data (b and c). As it can be seen the results of this model shows the good harmony with those of the buoy and ECMWF.

Since WSW ranges from January to March, according which, the wind speed and intensity increases, it affects the temperature and atmospheric pressure of the region. The best timing for the model simulation therefore, was considered to be from 10th to 16th of January (see Fig 2). The simulation was executed for longer period as a sake of comparison. Taking into account the proper Courant number, the time step for the simulation was selected as 300 seconds.

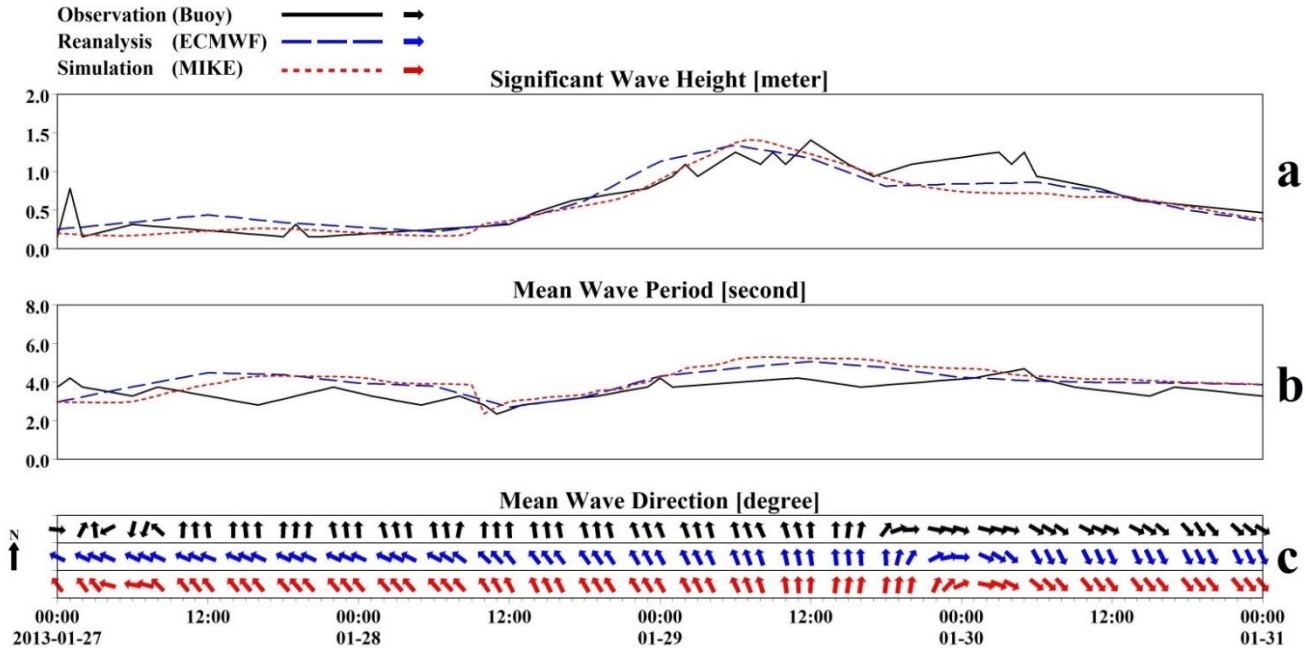

Figure 5. Time series of (a) significant wave height, (b) mean wave period, and (c) mean wave direction recorded in buoy, derived out from ECMWF reanalysed databasis, and from simulation applied in this study

In order to show statistically the goodness of results, and also to evaluate ECMWF data, four statistical parameters were considered including Bias, Correlation Coefficient (CC), Scattering Index (SI), and Root Mean Square Error (RMSE). These values are calculated for each model results and summarized in Table 2. According to these values, developed model in this research simulated wave parameters as good as the ECMWF reanalyzed databases; this is true for significant wave height, mean wave period, and mean wave direction. It should however be mentioned that simulated results represented by ECMWF shows slightly better agreement with buoy data in the case of significant wave height.

Table 2: Calculated statistical wave parameters

model	Wave parameters	Bias	CC	RMSE	SI
MIKE	Height	-0.065	0.90	0.17	0.27
	Period	0.53	0.59	0.77	0.21
	Direction	-15.9	0.88	37.3	0.17
ECMWF	Height	-0.005	0.91	0.16	0.26
	Period	0.46	0.55	0.67	0.18
	Direction	-20.04	0.86	48.3	0.23

3. Results and discussion

Figs 6 and 7 represent the time series data derived from the model. Fig 6 contains current speed and direction, and Fig 7 contains significant wave height, mean wave period and direction, for the period before, during and after WSW.

Fig 6 which show the time series of current speed and direction at monitoring point implies that WSW do not disturb the current speed and/or direction. Since the dominant current in the Persian Gulf is the result of tidal current, and current due to the density, this finding was presumed. The simultaneous variation between the wind speed and significant wave height is clear in the Fig 7. The rise of significant wave height (7b) simultaneous with the beginning of WSW (7a) is clearly shown in the figure. Fig 7c shows that the mean wave period is increased at the beginning of WSW. And Fig 7d shows the main direction of the wave propagation at the monitoring point.

Fig 8 shows the pattern of current for the whole area under investigation for a time step before, during, and after the WSW derived out from simulation using MIKE21. The date and time when the plots have been derived out, is at high tide. Plots of surface current show that the WSW has almost no effect on the pattern of surface current in this area. The dominant current in the northwest of Persian Gulf, as mentioned by literatures, is from northwest toward southeast (Pous et al., 2013; Reynolds, 1993; Kampf and Sadrinasab, 2006). The strength of the surface current is also almost the same for the three different periods.

The pattern of significant wave height for the area has been shown in Fig 9. The date and time when the plots have been derived out are: 17:00 in 9th of January (before WSW), 20:00 in 12th of January (During WSW), and 20:00 in 17th of January (after WSW). It is for a time step before, during, and after the WSW. Comparison of significant wave heights of the area for these three time steps shows significant effect of the WSW on the wave pattern of the area. It can be seen that this wind affects the height and the speed of the wave significantly. The wave height in the area is barely exceeds 1 m. before and after the wind, while during the WSW (middle plot) is mostly between 0.9 to 2.2m. This wind also causes the increase of the wave speed from about 1 m/s to about 2 m/s (almost twice).

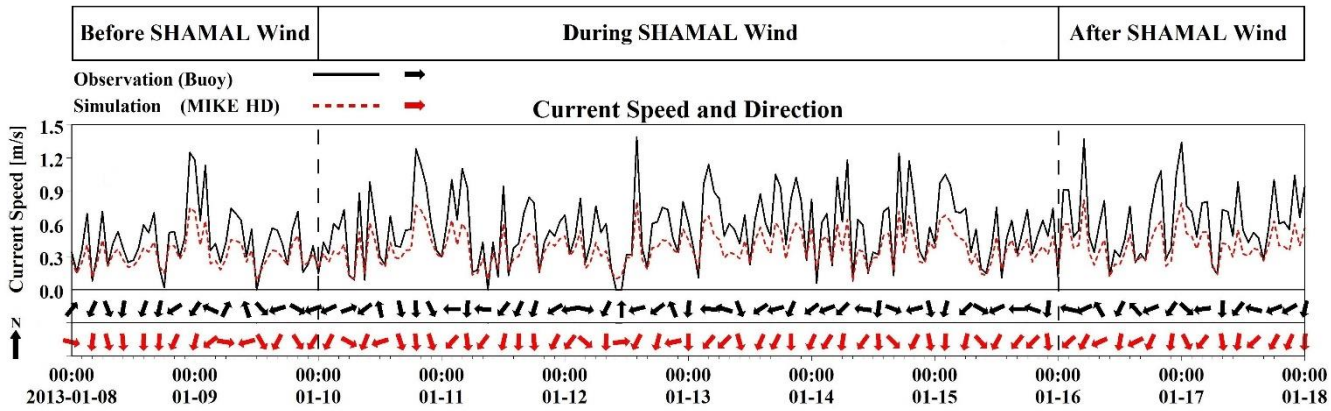

Figure 6. Time series of current speed and direction derived out from buoy data, and simulated by MIKE21 for the 08 to18 of January 2013

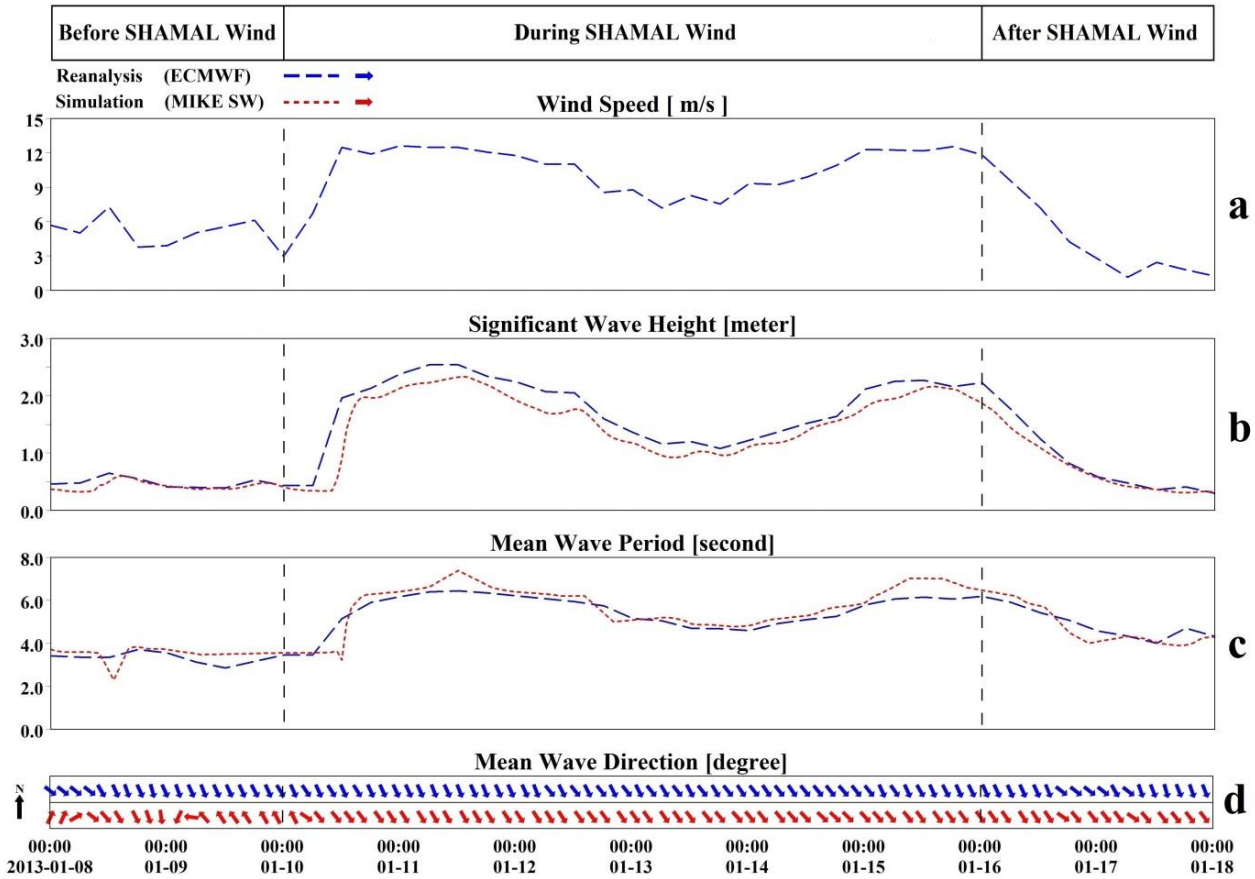

Figure 7. Time series of (a) Wind speed, (b) significant wave height, (c) mean wave period, and (d) mean wave direction of the simulation using MIKE21 in compare with ECMWF data, for the 08 to18 of January 2013

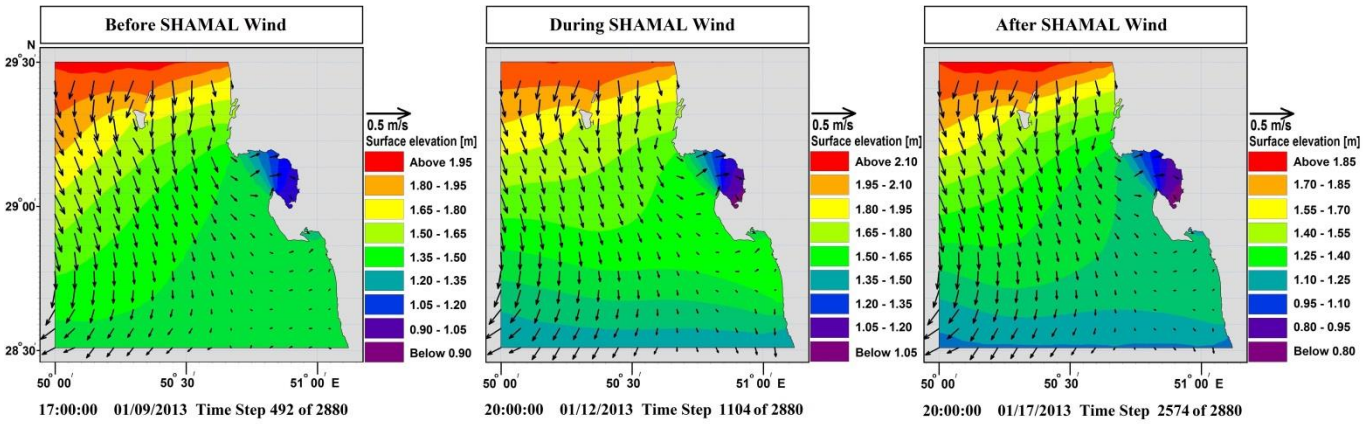

Figure 8. Patterns of current in the area under investigation for a time step before (top), during (mid), and after (down) WSW derived out from model

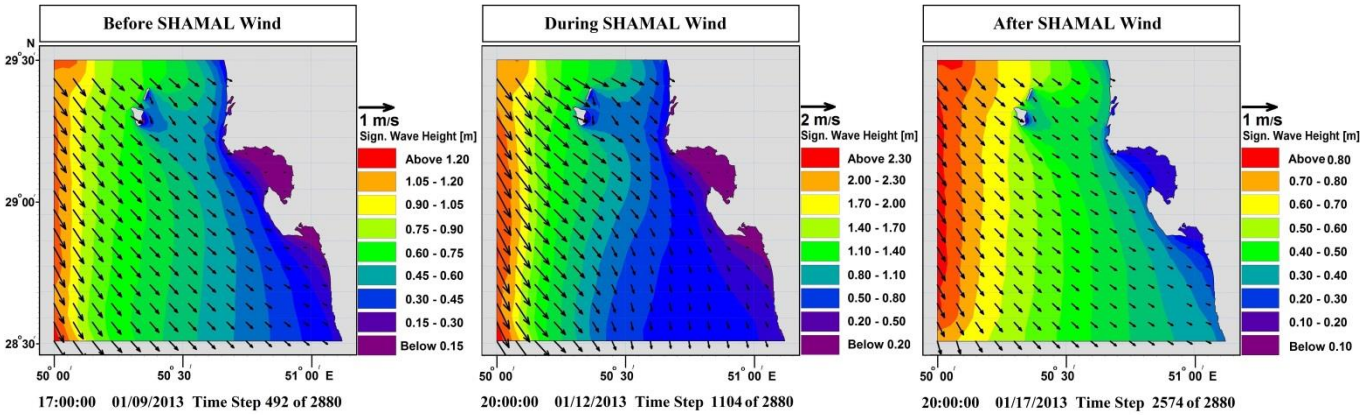

Figure 9. Patterns of significant wave height in the area under investigation for a time step before, during, and after WSW derived out from model

4. Conclusions

The effect of Winter Shamal Wind on the pattern of current and wind in the northwest of the Persian Gulf is studied using MIKE21. It was found that the direction of surface current in the study area is almost uniform and the simulated results shows no significant variety before, during and after the Winter Shamal wind. However, a small increase of about 0.1 m/s in speed of surface current was observed during Winter Shamal wind. Its direction is from the northwest to the southeast. It can be said that the pattern of current in the Persian Gulf as a semi-enclosed area always follows a general pattern of this Gulf and does not affected by Winter Shamal Wind.

In terms of significant wave height and wave speed however, results was different. Simulated results shows that During the Winter Shamal Wind, the maximum wave height is higher than that of before and after this wind. Moreover, it was found that the speed of waves exceeds to about 2 m/s during Winter Shamal Wind, which is a considerable amount for the wave speed.

The wave direction in the period of Winter Shamal Wind is mostly northerly and northwesterly. While, it is often southerly and easterly before and after the Winter Shamal Wind.

5. References

1- Abdi Vishkaee, F., Flamant, C., Cuesta, J., Oolman, L., Flamant, P., & Khalesifard, H. R (2012) Dust transport over Iraq and northwest Iran associated with winter Shamal: A case study. *Journal of Geophysical Research: Atmospheres*, *117*(D3).

2- Al Senafi F, Anis A (2015) Shamals and climate variability in the Northern Arabian/Persian Gulf from 1973 to 2012. International Journal of Climatology, 35: 4509-4528.

3- Arı Güner H A, Yüksel Y, Özkan Çevik E (2013) Estimation of wave parameters based on nearshore wind–wave correlations. Ocean Engineering, 63: 52-62.

4- Azizpour, J., Chegini, V., Khosravi, M., & Einali, A (2014) Study of the physical oceanographic properties of the persian gulf, strait of hormuz and gulf of oman based on PG-GOOS CTD measurements. *Journal of the Persian Gulf*, *5*(18): 37-48.

5- DHI. 2012. Mike21/3 Coupled Model FM, scientific documentation, D.H.I., Denmark.

6- El-Baz F (1994) The Gulf War and the environment.Taylor and Francis

7- Glejin, J., Kumar, V. S., Nair, T. B., Singh, J., & Mehra, P (2013) Observational evidence of summer Shamal swells along the west coast of India. *Journal of Atmospheric and Oceanic Technology*, *30*(2): 379-388.

8- Hunter J R (1983) Aspects of the dynamics of the residual circulation of the Arabian Gulf. Coastal Oceanography, 31-42
9- Kampf J, Sadrinasab M (2006) The circulation of the Persian Gulf: a numerical study. Ocean Science, 2: 27-41.
10- Komen G J, Cavaleri L, Donelan M, et al (1996) Dynamics and modelling of ocean waves. Cambridge University Press
11- Moeini M H, Etemad-Shahidi A, Chegini V (2010) Wave modeling and extreme value analysis of the northern coast of the Persian Gulf. Applied Ocean Research, 32: 209-218.
12- Perrone T J (1979) Winter shamal in the Persian Gulf. Naval environmental prediction research facility monterey ca, 180 p.
13- Pous S, Carton X, Lazure P (2013) A Process Study of the Wind-Induced Circulation in the Persian Gulf. Open Journal of Marine Science, 03: 1-11.
14- Rao P G, Al Sulaiti M, Al Mulla A H (2001) Winter shamals in Qatar, Arabian Gulf weather. Weather, 56: 444-451.
15- Rao P G, Hatwar H R, Al Sulaiti M H, et al (2003) Summer shamals over the Arabian Gulf. Weather, 58: 471-478.
16- Remya P G, Kumar R, Basu S (2014) An assessment of wind forcing impact on a spectral wave model for the Indian Ocean. Journal of Earth System Science, 123: 1075-1087.
17- Reynolds R M (1993) Physical oceanography of the Gulf, Strait of Hormuz, and the Gulf of Oman—Results from the Mt Mitchell expedition. Marine Pollution Bulletin, 27: 35-59.
18- Sadrinasab M (2010) Three dimensional numerical modeling of the circulation in the Persian Gulf. Oceanography, 1: 19-24.
19- Sorensen L S (2004) A third-generation spectral wave model using an unstructured finite volume technique. In 29th Intern Conf on Coastal Eng. Asce American Society Of Civil Engineers
20- Stewart R H (2008) Introduction to physical oceanography. Texas: Texas A and M University, 133-147
21- Thoppil P G, Hogan P J (2010a) A modeling study of circulation and eddies in the Persian Gulf. Journal of Physical Oceanography, 40: 2122-2134.
22- Thoppil P G, Hogan P J (2010b) Persian Gulf response to a wintertime shamal wind event. Deep Sea Research Part I: Oceanographic Research Papers, 57: 946-955.
23- Walters Sr K R, Sjoberg W F (1998) The Persian Gulf region: a climatological study. USA, USAF Environmental Technical Applications Center, Scott Air Force Base, Illinois, 62225-5438.
24- Yao F (2008) Water mass formation and circulation in the Persian Gulf and water exchange with the Indian Ocean. Coral Gables, Florida: University of Miami

.